POWER ELECTRONIC TOPOLOGIES WITH HIGH DENSITY POWER CONVERSION AND GALVANIC ISOLATION FOR UTILITY INTERFACE

A Dissertation

by

HARISH SARMA KRISHNAMOORTHY

Submitted to the Office of Graduate and Professional Studies of
Texas A&M University
in partial fulfillment of the requirements for the degree of

DOCTOR OF PHILOSOPHY

Chair of Committee,	Prasad N. Enjeti
Committee Members,	Hamid A. Toliyat
	Shankar P. Bhattacharyya
	Won-jong Kim
Head of Department,	Chanan Singh

May 2015

Major Subject: Electrical Engineering

ABSTRACT

The past decade has seen a significant increase in the number of applications where power electronic converters play a major role. Renewable energy systems such as wind turbines, solar photovoltaics, etc. employ power converters to interface with the utility grid. More and more power converters are being used in transportation sector such as in electric vehicles, locomotives, aircrafts, ships and submarines. Advancements in power converter topologies and devices have constantly pushed the limits and standards applicable in different markets towards better efficiency, lower cost and higher power density. Especially for large power systems such as wind turbine generators, adjustable speed drives, locomotives, etc., achieving smaller footprint at low cost and high efficiency has become a major challenge. These factors generate the major impetus towards the research undertaken in this dissertation.

In applications that require integration with the utility grid, the bulkiest components are usually the transformers, inductors and DC electrolytic capacitors. Instead of using a line frequency transformer to interface any power electronic system with the utility grid directly, it is possible to use a power converter to transform the line frequency AC into a higher frequency AC that can be fed to a medium or high frequency transformer. These transformers are much smaller and lighter compared to line frequency transformers. This dissertation elucidates these concepts in detail in the first section as well as at the beginning of each subsequent section, along with a summary of such techniques already proposed in the literature.

The sections in this dissertation propose and discuss several architectures (approaches) adhering to the earlier stated concepts that enable higher power density energy conversion for applications such as wind turbines, adjustable speed drives, data centers, energy storage systems, etc. Detailed operational analysis, design example, control strategy, simulation results and experimental results are shown for each concept or topology. The advantages and drawbacks are also discussed.

Finally in this dissertation, the medium or high frequency transformers that can be used in the proposed approaches are analyzed in detail using ANSYS Maxwell software in terms of material, saturation, loss and size. Further, these numbers are used to estimate the relative size advantage and efficiency that can be achieved using higher frequency transformer compared to a line frequency transformer for utility interface applications. It will be shown that for many high power applications, medium frequency transformer based circuit designs can be more efficient and simpler alternatives for high frequency transformer based approaches. The specific contributions along with future research opportunities of the proposed concepts are summarized at the end.

ACKNOWLEDGEMENTS

I do not have enough words to thank my advisor, Dr. Prasad N. Enjeti for imparting knowledge and molding me into a researcher that I am today. He has not only been a wonderful guide to me, but also a patient mentor with whom I always enjoyed having long discussions about engineering, professional career, and other aspects of life, throughout my graduate study. I feel privileged to have a PhD committee involving very eminent professors in Dr. Hamid A. Toliyat, Dr. Shankar P. Bhattacharyya and Dr. Won-jong Kim. I extend my sincere gratitude for their insight, guidance and time spent for me. I also thank the Qatar National Research Foundation for their support. I thank the Texas A&M ECE department staff, especially Tammy Carda, Jeanie Marshall, Annie Brunker, among all others who helped me immensely during my life at graduate school. I should also acknowledge and thank my professors and teachers from my earlier years in undergraduate university and high school for providing the foundation necessary to accomplish this work.

I would like to acknowledge all current and past students in the research group and in Texas A&M power electronics division, without whom my work would have been very hard. I thank (in no particular order) Somasundaram Essakiappan, Pawan Garg, Poornima Mazumdar, Joshua Hawke, Dibyendu Rana, Jorge Ramos, Jose Sandoval, Michael Daniel, Taeyong Kang, Bahaa Hafez, Ahmed Morsy, Vivek Sundaram, Yateendra Deshpande, Souhib Harb, Mohammad Shadmand and all others in the EPPE research division for making learning and life enjoyable.

I extend my gratitude to all my colleagues from GE, Ford, Schlumberger and Google, where I have worked/interned at different points of time, for providing me with a deep knowledge of their respective industry. I would also like to thank organizations such as ABB, Magna-Power, etc. for providing valuable support to my research through funds, facilities or services.

Last but not least, I thank my wife, Tulasi, my parents, brother, in-laws, relatives and friends for believing in me, supporting me and also for boosting my morale when the chips were down.

TABLE OF CONTENTS

Page

LIST OF FIGURES

Page

LIST OF TABLES

Page

1. INTRODUCTION

1.1. Introduction

The world has seen a steep rise in the usage of renewable energy resources, driven by issues such as global warming, depletion of non-renewable energy sources, etc. The United States' Department of Energy (DoE) predicts that as a proportion of total electricity supply, renewable energy sources will contribute almost 20 % in the year 2050 compared to 12 % in 2010 (see Figure 1-1 from NREL report [1]). In order to utilize these vast energy resources, energy has to be converted from one form to another and interfaced to the electric grid. This has significantly increased the prospects of power electronics in the energy sector [2].

Power converters process the power generated from renewable energy sources such as wind turbines, solar photovoltaics (PV), etc., and convert them to the voltage and frequency levels suitable for the utility grid. Not only in power generation, but power electronic converters are also used to interface different high power electro-mechanical loads to the utility grid, such as adjustable speed drives (ASDs), electric vehicle (EV) battery, uninterruptable power supply (UPS), etc. Recently, governments have also started coming up with certain energy storage mandates, targeting the use of battery and other energy storage media to offset the demand-supply gap in the electric grid or to act as buffer for the intermittent and unpredictable renewable energy sources [3]. The objective of future power conversion will be processing maximum power with the highest efficiency and reliability, at the smallest footprint and cost.

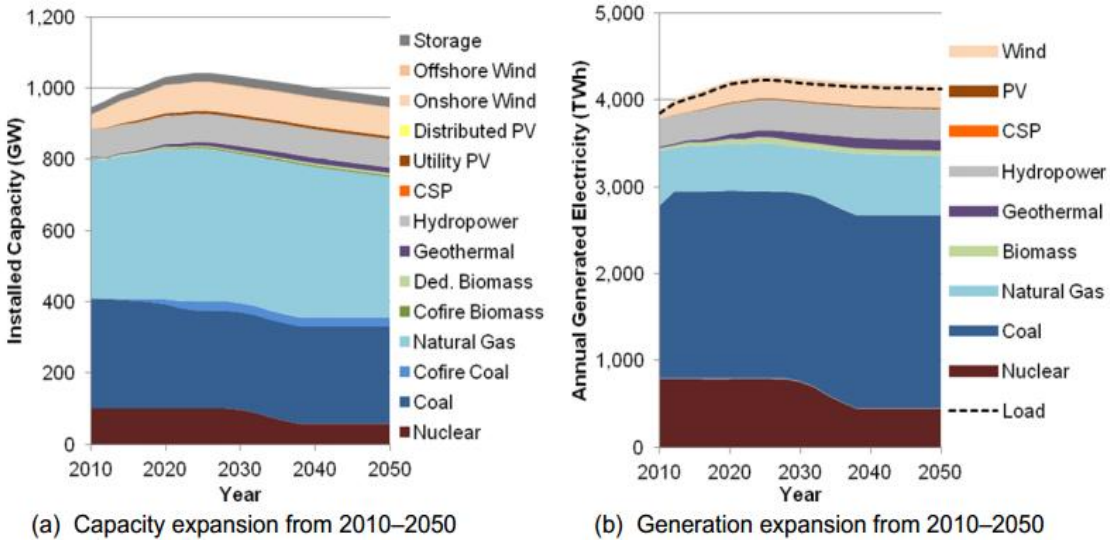

Figure 1-1: Capacity and generation expansion in low-demand as baseline (Adapted with permission from the US National Renewable Energy Laboratory [1])

1.2. Applications Involving Utility Interface

DoE forecasts the following distributed energy sources (DES) to have significant impact in the US energy market: *solar photovoltaics* (PV), *wind turbine generators* (WTG), *micro-turbines* (MT), *Fuel Cell Systems* (FCS), etc. Apart from these sources, owing to their operation flexibility and dispatchability, *battery energy storage systems* (BESS) and *electric vehicles* (EV) may also fall under the category of DES [4]. EVs in the future will also be an energy storage option for the grid when the concept of *vehicle-to-grid* (V2G) materializes on a large scale.

Figure 1-2: shows some of the DESs being employed in utility interface applications. Utility interface of high power DESs generally require transformers to provide galvanic isolation. Similar is the case with large loads like ASDs, data center power system, etc. [5]

1.3. Power Density and Power-to-Mass Ratio of Converters

Power density of a converter can be defined as (1.1):

$$Power\ Density\ \left(\frac{W}{m^3}\right) = \frac{Total\ Power\ Processed\ (W)}{Total\ Volume\ (m^3)} \tag{1.1}$$

Figure 1-2: Distributed energy sources (Adapted with permission from the US National Renewable Energy Laboratory [4])

Alternately, some literatures also define power density as *power-to-mass* or *power-to weight* ratio. Though the theme of this research involves both power-to-volume ratio and power-to-mass ratio, the usage of the term '*power density*' is as per eqn. (1.1) and any reference to the mass/weight is represented appropriately. It is widely

considered that in order to scale up large power systems such as wind turbines, electric locomotives, etc., power density has to be increased. DoE has set a target to reduce the production cost of electric tractions by 50% and increase the power density by 20% by 2020. Advantages of achieving higher power density are: reduced weight/footprint, reduced fuel consumed during transportation, reduced cost, simpler installation/maintenance, etc.

Figure 1-3 shows a high power system in electric locomotives and off-shore wind turbines. The power converter is placed at the base in an electric locomotive, whereas the converter is typically placed on top of the tower in off-shore wind turbines. In both systems, any improvement in power density achieves all the advantages mentioned above [6-10].

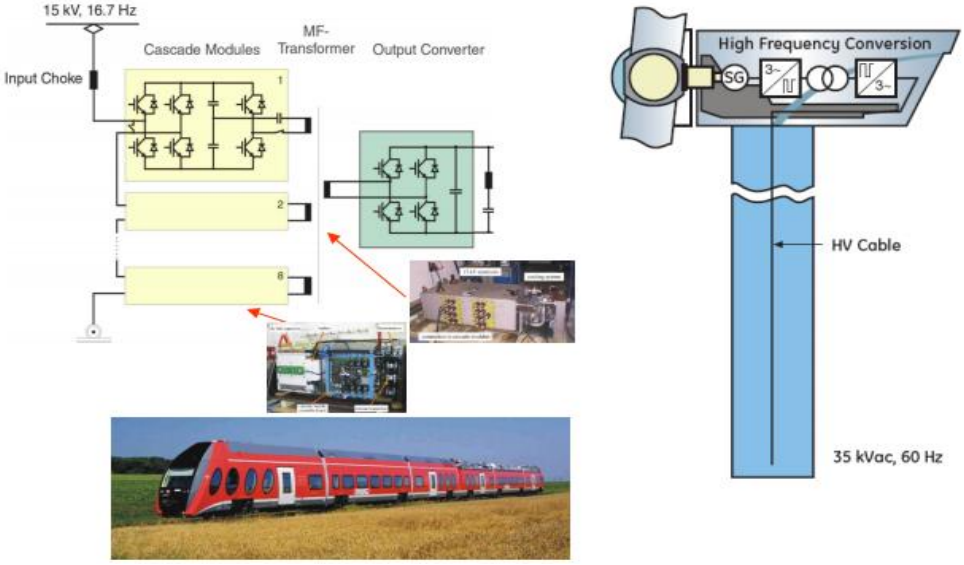

Figure 1-3: Electric locomotive and offshore wind turbines [8-10] (Adapted with permission from the National Institute of Standards and Technology, U.S. Dept. of Commerce [10])

1.3.1. Components Affecting Power Density

A typical power conversion scheme for utility integration has the following major components: power semiconductor devices (IGBTs, MOSFETs, etc.), filter passive components (inductors, capacitors, etc.), DC-link capacitor, heat sink, power transformer. Figure 1-4 shows the comparison of space occupied by different components in a non-isolated DC-AC inverter (rated 10 kW) [11]. The 2-Level Voltage Source Inverter (2LVSI) along with boost converter (BC) at 8 kHz occupies almost 4.0 L (1 L = 1 dm^3), with the inductor occupying around 2.5 L, the DC capacitor, devices and heat sink occupying 0.5 L each.

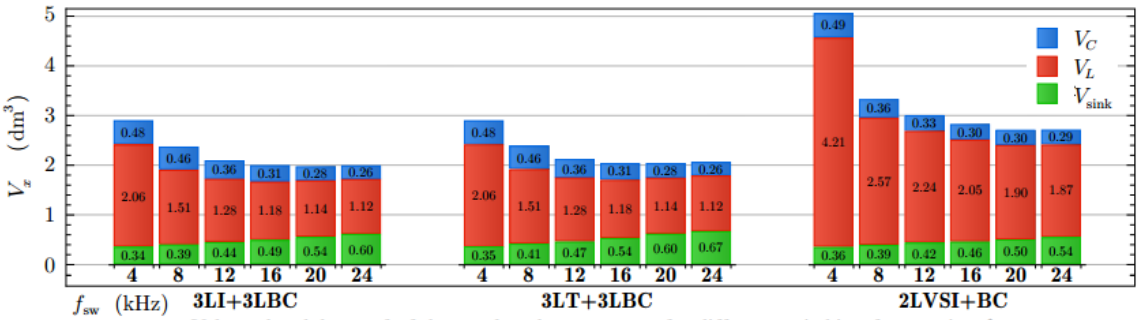

Figure 1-4: Volume of components in a 10 kW DC-AC converter (© 2013 IEEE [11] – Adapted with permission from the IEEE)

If galvanic isolation has to be added to this system, a reasonable volume estimate of a 10 kVA transformer is around 20 L, which is greater than *80%* of the entire system volume. From this, it can be stated that the magnetic components such as transformer and inductor, typically affect the power density of a power conversion scheme. Not only the volume, but the magnetic components also affect the weight of the converter almost

to the same extent. Magnetic components are followed by DC-link capacitors and heat sinks in terms of size. Any reduction in the size of these components will drastically improve the system power density, especially in systems where it is either mandated or desired to employ power transformers for isolation.

1.3.2. Methods to Improve Converter Power Density

One of best known methods to improve the power density of converters is to increase the frequency of the transformer or inductor core [12-14]. At a higher frequency, a transformer core can carry the same amount of flux lines at a smaller area (assuming same flux density). From Figure 1-5 [14], it can be noticed that the volume of a 1 MVA silicon (Si) steel core transformer can be reduced from 2000 L to 200 L if the core frequency is increased from 50 Hz to 1000 Hz. This transformation in the frequency can be implemented using power electronics. Though it is possible to increase the frequency and reduce the volume/weight, this may lead to higher losses and audible noises if the magnetic flux density is not chosen appropriately. If a better core such as amorphous silicon (Si) or nano-crystalline Si is employed instead of conventional Si steel core, this further increases the cost. Power electronics further adds to cost and power losses, also affects the system reliability. This research does not focus on the reliability aspect, though reliability can be a major factor for commercialization.

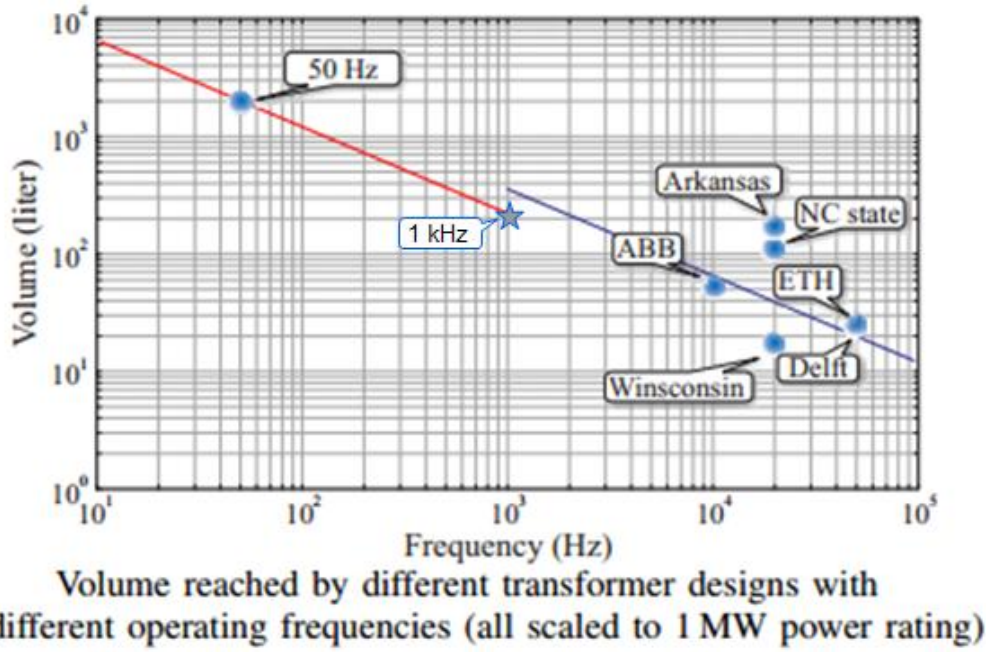

Figure 1-5: Volume comparison of different transformer designs (© 2010 IEEE [14] – Adapted with permission from the IEEE)

1.3.3. Medium or High Frequency Transformer

Once it is decided that an application is going to replace a line frequency transformer to a higher frequency transformer with power electronics, the design of the transformer, especially its core has to be primarily optimized for size, losses, cost and audible noise. Different factors influencing these parameters are the core material, core operating frequency, magnetic flux density, etc [13]. Typically considering high power applications (greater than 500 kW), Si steel cores (around $800/ton [15]) can be used for frequencies lower than 1.5 – 2.0 kHz. If taken to higher frequencies, the core loss and audible noise will be very high. Amorphous core can be used at higher frequencies up to around 5.0 – 8.0 kHz, but cost higher than Si steel (around $2500/ton). Ferrite and nano-crystalline cores can be used even at frequencies as high as 20 – 25 kHz (have much

lower core losses), but the materials are very expensive (more than $12000/ton). Moreover if desired to operate at very high frequencies, the skin effect and corona effect will be significant and it might become necessary to construct the transformer larger, losing out a little on the size advantage. Also, the power converter switching loss will be much higher even with soft-switching techniques. Overall, the transformer has to be designed according to the application. Table 1-1 shows an example design of a 60 Hz and a 1000 Hz transformer for 142 kVA power (Si steel core). It can be seen that the 1000 Hz transformer is almost 25% of the volume and much lower in cost compared to 60 Hz transformer. This may offset the power electronics cost.

Table 1-1: An example design comparison of a 60 Hz transformer and a 1000 Hz transformer

PARAMETER	1000 HZ DESIGN	60 HZ DESIGN	NORM 60 HZ DESIGN	UNIT
KVA RATING	142.2	34.6	142.2	KVA
FLUX DENSITY	3700.0	15000.0	15000.0	GAUSS
CORE LOSS/LB	2.0	1.0	1.0	W/LB
CORE LOSS	480.0	240.0	986.4	W
WIRE LOSS	632.4	491.2	2018.7	W
CORE WEIGHT	240.0	240.0	986.4	LB
WIRE WEIGHT	65.8	65.8	270.5	LB
NORMALIZED SIZE	1.00	1.00	4.11	
EFFICIENCY	0.99	0.98	0.98	
CORE COST	$316.80	$316.80	$1,301.99	
WIRE COST	$128.55	$128.55	$528.32	
CORE + WIRE COST	$445.35	$445.35	$1,830.31	

1.4. Power Converter Modelling and Implementation

This section explains certain basic concepts of deriving the switching function of a converter, and later selecting the converter to implement the switching function. Once the specifications of the input and output of a converter are given, the switching function

can be defined as the ratio of output voltage to the input voltage. Figure 1-6 shows the switching function for a power converter when the input is DC and the output desired is a high frequency square wave. The frequency spectrum (FFT) of output voltage shown in Figure 1-6 confirms the equations.

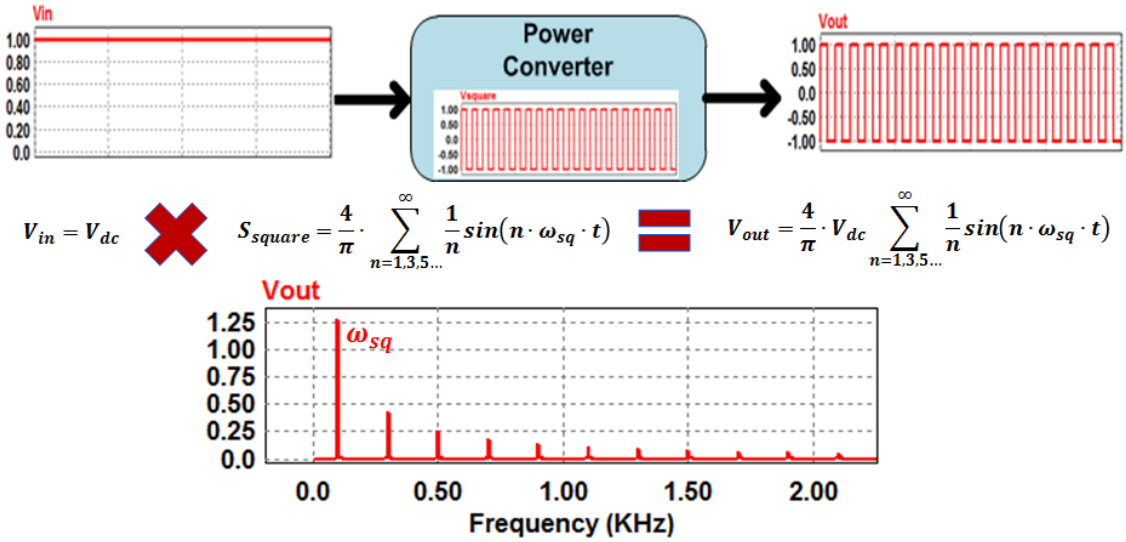

Figure 1-6: Square wave switching function for DC input

Figure 1-7 shows the switching function and output voltage of a power converter when the input is low frequency sinusoidal AC and the output desired is of high frequency AC. The frequency spectrum (FFT) of output voltage in such a case is also shown in Figure 1-7. Unlike the earlier situation, the output here is a multiplication of the input low frequency sine wave and higher frequency square wave switching function. From the equations, it can be seen that the output voltage equation can be obtained by simply multiplying the input with the switching function. Assuming ω_s is the input frequency and ω_{sq} is the square wave frequency, the output voltage has fundamental frequency as $\omega_{sq} \pm \omega_s$ as verified by the FFT in Figure 1-7.

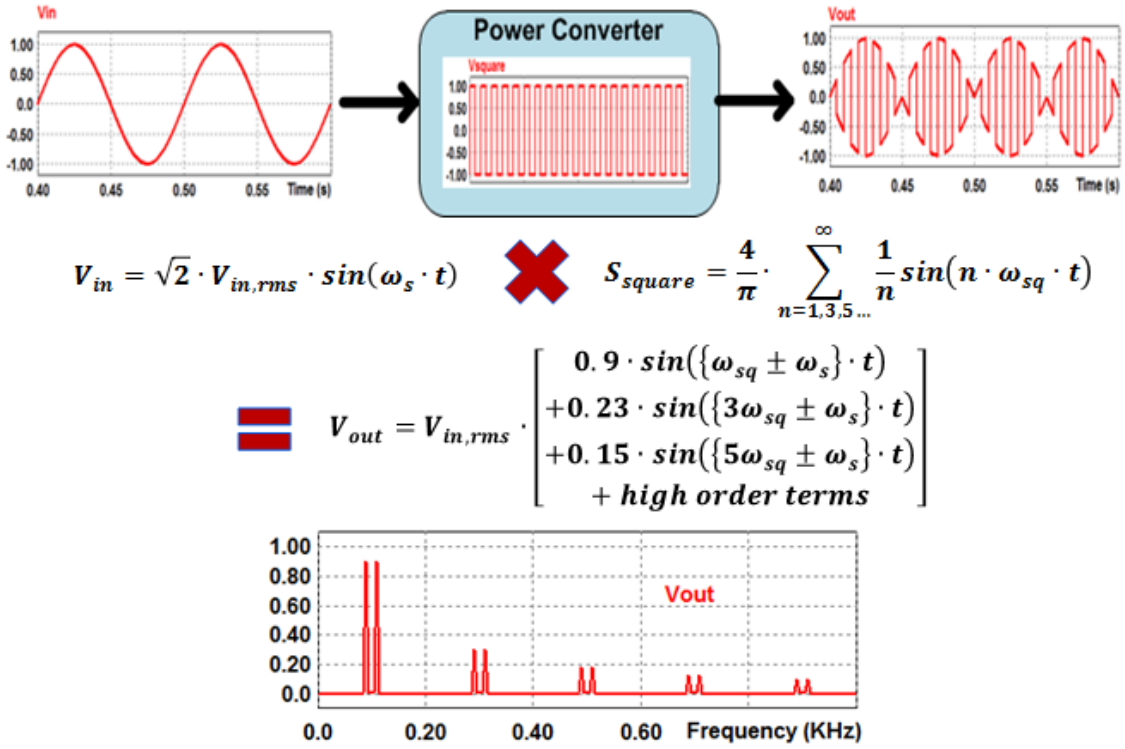

Figure 1-7: High frequency square wave switching function for low frequency sinusoidal input

From Figure 1-7, it can be seen that a square wave modulation creates many frequency tones at $3\omega_{sq} \pm \omega_s$, $5\omega_{sq} \pm \omega_s$, etc. on the output, due to the higher order terms present in the Fourier series expansion of a square wave (switching function). If only the fundamental tone(s) is (are) required, a physical filter can be placed at the output. Otherwise, the converter modulation can be selected as a higher frequency sine wave.

Instead of a medium or high frequency square wave, it is possible to modulate the converter with a sine PWM switching function, as shown in Figure 1-8. It can be seen from Figure 1-8 that when an input sinusoidal voltage of frequency ω_s is operated upon by a sine PWM of fundamental frequency ω_{mf}, the output once filtered is a voltage waveform of frequencies $\omega_{mf} \pm \omega_s$.

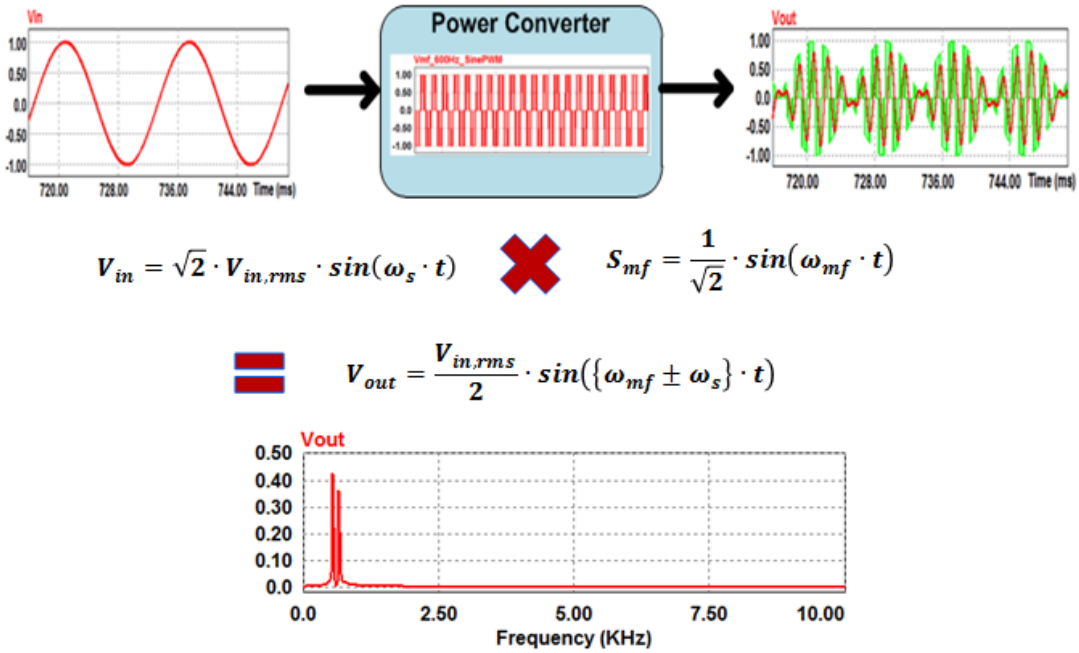

Figure 1-8: High frequency sine PWM switching function for low frequency sinusoidal input

However in power electronics, the switching states are discrete and it is difficult to do amplitude modulation. Instead, pulse-width modulation (PWM) methods can be used where a sine wave can be interfaced with a higher frequency triangle in such a way that the switching function has a desired fundamental frequency and the next frequency is close to the frequency of the interfacing triangle (PWM frequency). Such a scheme can reduce the filter size since the PWM frequency can be chosen to be much higher, only limited by the device losses. Figure 1-9 shows two of the major methods by which this can be achieved – *bipolar PWM and unipolar PWM.*

Using PWM scheme, any desired switching function can be implemented; it can even be a sum or product of many different switching functions. There are alternate switching methods too, such as programmed PWM, Space Vector (SV) PWM, etc.

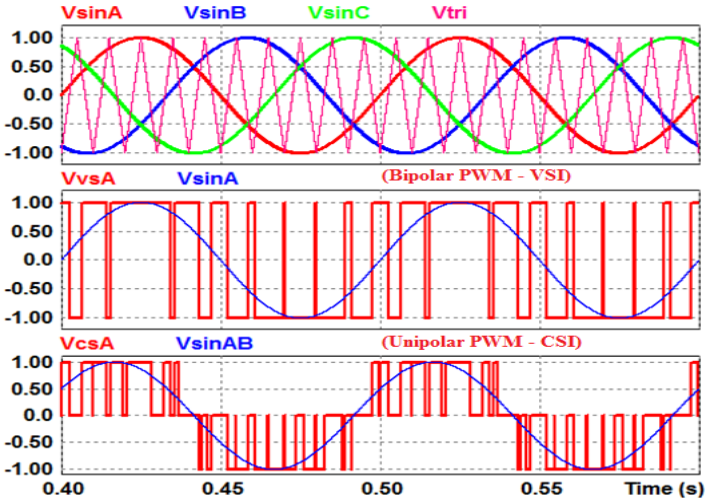

Figure 1-9: Sinusoidal PWM switching function – bipolar and unipolar versions

While an AC-DC rectifier or DC-AC inverter can transform AC to/from DC, AC-AC converter (cyclo-converter/matrix-converter) can directly convert AC from one frequency to another. Figure 1-10 shows the evolution of AC-AC converters (1-phase) from full-bridge with bidirectional switches (direct bidirectional) to back-to-back inverter bridge (indirect bidirectional) and back-to-back diode bridge and inverter bridge (indirect unidirectional) from there. The choice of topology depends on the application. When higher frequency transformers are involved, the topology can be broadly classified as solid state transformer (SSTs) or electronic transformers.

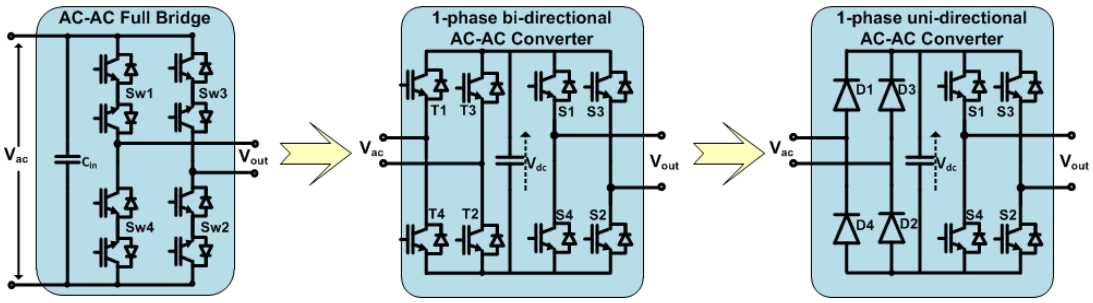

Figure 1-10: AC-AC converter evolution – bidirectional (with / without bidirectional switches) to unidirectional

1.5. Research Objective

From the earlier sub-sections, it is evident that the power electronics industry is moving towards higher efficiency at lower cost and smaller footprint. In response to this growing demand for smaller and less expensive energy conversion, this dissertation aims to propose, design, analyze and test isolated power converter topologies that improve the power density of certain utility interface applications, such as wind turbine generators (WTGs), adjustable speed drives (ASDs), etc., over the conventional topologies. All the proposed topologies employ unidirectional or bidirectional AC-AC converters and also use medium frequency (MF) or high frequency (HF) transformers to achieve higher power density. AC-AC converters avoid DC electrolytic capacitors due to pulsating (weak) DC bus instead of a stiff one. The major concepts discussed earlier in this section are used at multiple locations throughout this dissertation.

A conventional WTG system uses back-to-back inverters that convert low frequency AC to the line frequency AC, which is then interfaced to the utility grid via a bulky line frequency transformer. In case of a large ASD system, a 12-pulse or 18-pulse diode rectifier configuration is usually used, which also employ line frequency transformers in star-delta configuration. When analyzed in depth, the largest components present in these conventional topologies are mostly the line frequency transformers and the filter inductors. They are also usually the most expensive components too. The theme of this dissertation revolves around identifying and formulating alternative strategies that replace the bulky line frequency transformers with a combination of AC-AC converters and higher frequency transformers. The sole purpose of the AC-AC converters is to

modulate the line frequency voltage to higher frequency AC suitable to interface with a MF or HF transformer. In order to interface the system with a medium voltage (MV) utility grid, multi-level AC-AC converters can be used. One such multi-level approach has also been studied and experimented in this dissertation. Wherever possible, simple open loop control strategies are employed. Even where closed loop control is required, conventional PI control is used most of the time, which makes the proposed approaches attractive to the industry.

Once it is decided that a higher frequency transformer is desired for an application, there are two main choices – (a) use silicon steel, powdered iron or amorphous silicon core based MF transformer or (b) use ferrite or nano-crystalline core based HF transformer. A MF transformer made with silicon steel or amorphous core operating at or around 1 kHz can be as small as 25 % of a 60 Hz transformer, while a HF transformer using ferrite core operating at or above 10 kHz can be constructed to be much smaller. But factors such as higher corona loss, higher converter switching loss, higher material cost, etc. restrict the advantages of size reduction in HF transformers. This dissertation hence concentrates more on MF transformer based approaches, but even higher frequency transformer based approaches have been studied in brief. Moreover most of the proposed topologies can be extended to higher frequencies.

After designing and analyzing the proposed topologies, simulations have been done for each concept. Further, experimental results on scaled down laboratory prototypes validate the functionality of the proposed topologies. Since hardware demonstrations could not be carried out on megawatt scale due to restrictions in the set-

up, 2-D finite element analyses are done using ANSYS Maxwell software, using which it is possible to do comparisons on loss, size and saturation effects of transformers under different core materials for the proposed techniques. These studies conclude the research performed through this dissertation.

1.6. Outline of Dissertation

This dissertation is organized into seven sections. Section 1 introduces the main utility interface applications and the concepts of power density in power converters. The size benefits of using a MF or HF transformer over a line frequency transformer are explained in detail. Mathematical modeling of power converters at various modulation schemes is elucidated and the section concludes by describing the research objective. Since the organization of the dissertation is into different applications, literature review is covered at the beginning of each major section.

Section 2 proposes an isolated 3-phase AC-DC converter that employs a MF or HF transformer and avoids DC electrolytic capacitors on the utility side power converter. The proposed topology is then compared with a conventional scheme in terms of size and efficiency. The control strategy is also explained in detail in this section and the concept is validated through simulation and experiments. Section 3 proposes a simple multi-pulse diode rectifier concept using MF or HF transformers that replace bulky line frequency transformers in a conventional multi-pulse rectifier. Theory, analysis, simulation and experiments are performed for a 12-pulse rectifier configuration, but a generic scheme to extend this strategy towards 18-pulse or 24-pulse rectifier is also shown in this section. Section 3 also proposes an alternate isolated AC-DC rectifier

suitable for ASDs, WTGs, etc., especially for medium voltage (MV) applications. Here, the utility AC is converted to MF AC, which is then fed to three 1-phase MF transformers. The secondary side of the transformers are connected in star or delta configuration and then fed to 3-phase diode rectifiers as in a 6-pulse rectifier. Detailed analysis, simulation and experimental results are presented in this section.

Section 4 extends some of the concepts proposed in sections 2 and 3; and applies them to develop topologies for wind turbine generator (WTG) – medium voltage DC (MVDC) interconnection that are suitable for offshore farms and long-distance transmission line. The section starts with the introduction to offshore wind farms and some of the WTG – MVDC converters already proposed in the literature. Then the proposed topologies are explained, followed by detailed analysis and simulation results. Section 5 starts with the introduction of battery energy storage systems (BESS) in modern day grid and the benefits of employing megawatt scale BESS on the stability of the power grid. Then a MF transformer based approach is proposed for interfacing a large scale BESS system to the utility grid. As an extension, a 3-port scheme for interfacing a WTG system along with a BESS system is introduced in this section. Detailed simulation and experimental results are also shown.

Section 6 discusses about modeling the MF or HF transformer using ANSYS Maxwell software. The approaches proposed in the earlier sections are evaluated for their transformer design under the criteria of size and losses. Comparison in terms of size and losses in the MF or HF transformers (using electrical steel, amorphous and ferrite core materials) with respect to the line frequency transformer are also shown. The

section concludes by explaining about the variation of overall size and efficiency of the power converter system for different transformer core materials.

Section 7 provides a summary of the research work reported in this dissertation and concludes with recommendations for future research topics in this area.

2. HIGH POWER AC-DC CONVERTER WITH BOOST PFC

2.1. Isolated AC-DC Converters

AC-DC converters have become a commodity in consumer electronics and due to stringent safety standards; many of them either have mandatory specifications or requirements on galvanic isolation. AC-DC converters using high frequency (HF) or medium frequency (MF) transformers are popularly used in electric vehicle (EV) charging, adjustable speed drives (ASDs), server power supplies, 3-phase battery chargers, etc. [16-18]

One of the very conventional topologies involves a simple 3-phase diode rectifier front-end, a stiff DC-link follower by an isolated DC-DC converter, as shown in Figure 2-1. But this has high input current harmonics, due to the rectifier operation, which increases filter requirement. A popular topology for a 1-phase high power isolated AC-DC converter used extensively is a boost power factor correction (PFC) stage followed by a DC-DC converter stage [16, 19, 20]. Many 3-phase isolated AC-DC converters also employ a similar scheme by having the three phases connected in parallel on the output DC side, as in Figure 2-2 [21]. As seen in Figure 2-2, the boost PFC stage operation makes the inductor current in phase and shape as the diode rectified pulsating DC voltage, thereby making the utility power factor close to unity. In effect, the PFC stage emulates an ‘active resistor’ to the utility grid. Since the H-bridge of the isolated DC-DC converter stage requires a fixed DC, the boost PFC stage output DC-link capacitors have to be large (to suppress the 2nd harmonic ripple). Moreover, the square wave shape of

the waveform at the transformer primary necessitates the use of three 1-phase transformers instead of a single 3-phase transformer to have balanced flux distribution, resulting in slightly lower power density.

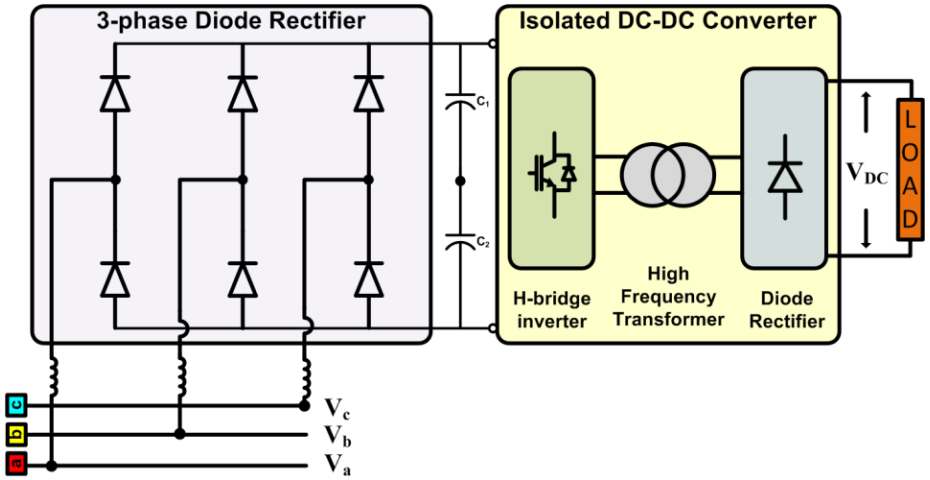

Figure 2-1: AC-DC converter with a 3-phase diode rectifier front-end and an isolated DC-DC converter

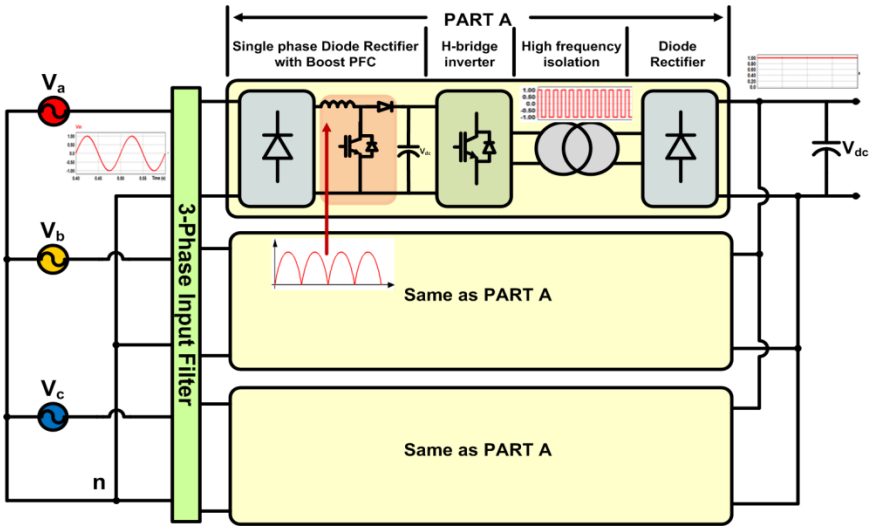

Figure 2-2: A high power AC-DC approach using three 1-phase PFC-DC-DC converter stages.

Several other AC-DC converters have been proposed in the literature [22-28]. Some of the popular configurations, namely Swiss rectifier, Vienna rectifier, Y-rectifier, etc, have been summarized in [27, 29, 30].Many of these configurations are suitable for non-isolated AC-DC converters or require a separate DC-DC converter for isolation. Some may also require additional circuitry to achieve unity power factor (UPF) at the utility side. Figure 2-3 shows a Vienna rectifier-front-end based isolated AC-DC converter, which is an improvement over the system shown in Figure 2-1, enabling better input current quality. But this topology has seven power semiconductor devices for each leg, contributing to higher conduction losses.

A single phase AC-DC power converter is proposed in [31], that uses flyback transformer and a resonant active-clamp circuit. Different PFC topologies in flyback as well as bridged configurations in interleaved structure have been proposed in [32-35]. Some approaches such as [31, 36, 37] employ soft-switching for obtaining higher efficiencies even at higher frequencies for rectifier applications. Since AC-DC conversion is a very important segment in systems involving distributed energy sources, several unidirectional and bidirectional topologies have been proposed for such applications that use either line frequency or higher frequency transformers for isolation [21, 22, 38]. Many of these topologies either use large electrolytic capacitors or employ complicated control strategies.

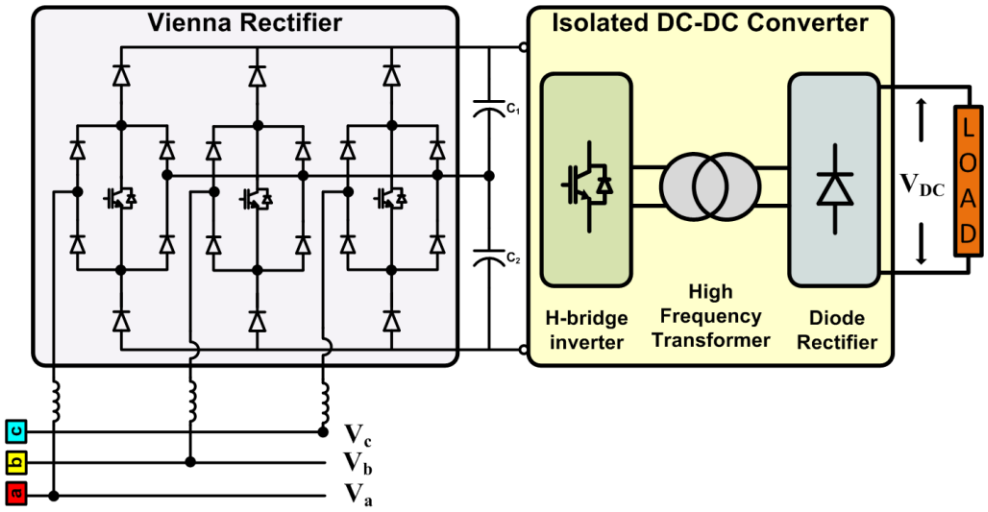

Figure 2-3: Vienna rectifier front-end based isolated AC-DC converter

In order to provide a higher power density alternative for isolated utility interface AC-DC converters, this section proposes a 3-phase HF or MF transformer based topology (see Figure 2-4) [39] that can be derived from the conventional topology shown in Figure 2-2. The proposed system has three 1-phase AC-AC converters transmuting the 3-phase utility AC to high/medium frequency AC, suitable for the transformer. The AC-AC converters can be constructed with diode front-end. Based on the application and power rating of the converter, either a medium frequency (MF) transformer (with conventional silicon steel or amorphous silicon core) or a high frequency (HF) transformer (with nano-crystalline or ferrite core) can be employed [38, 40, 41]. The secondary side has three 1-phase boost PFC stages, whose DC outputs are connected in parallel (they can be connected in series if higher DC voltage is desired) to form a single DC-bus. The modulation, control and filters are explained in subsequent sub-sections. Major advantages of the proposed topology [26, 39] are:

- It is modular in design, since each phase sub-system can be connected separately.

- The HF/MF transformer provides galvanic isolation, also improves the power density.
- The input side AC-AC converters have pulsating DC-link and avoid electrolytic capacitors, hence contribute to lower switching losses.
- A single 3-phase transformer can be used (see Figure 2-5) as the net flux is balanced in theory, due to the AC-AC converter operation. Any small imbalances can be taken care of by adding a thin fourth leg for the transformer core.
- The three 1-phase boost PFC stages on the secondary side are regulated to achieve unity power factor (UPF) at the utility input.
- The common output DC-bus enables the 3-phase reactive power balancing. This topology is suitable for battery charging, server power supplies, etc.

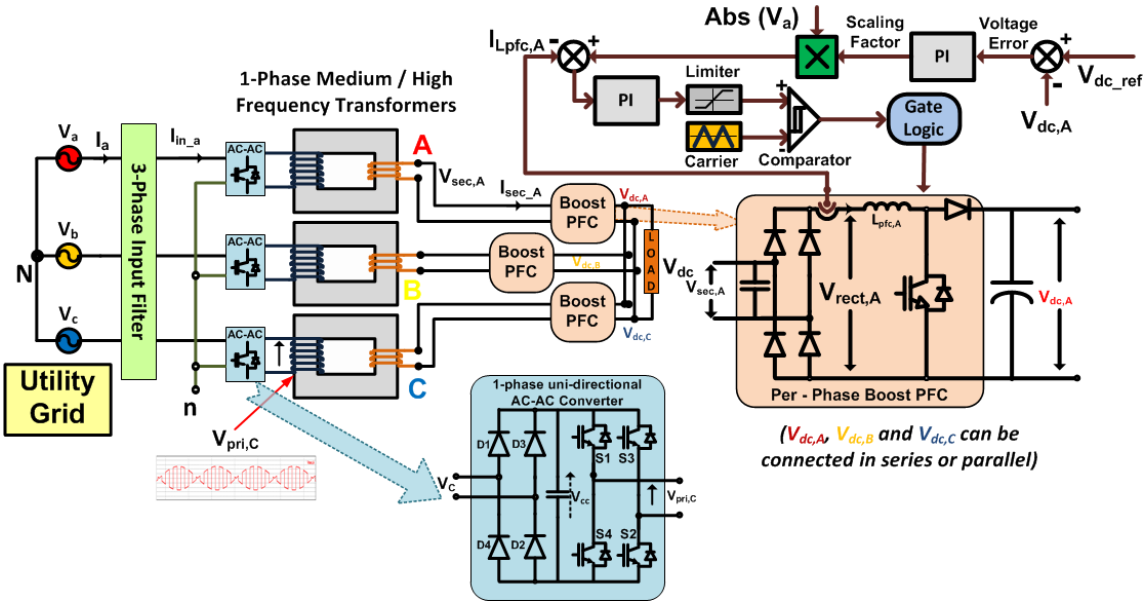

Figure 2-4: Proposed AC-DC converter with three 1-phase MF/HF transformers and boost PFC circuits (three DC outputs, $V_{dc,A}$, $V_{dc,B}$ *and* $V_{dc,C}$ of the boost PFC stages can be connected in series or parallel as required for the application)

2.2. Proposed 3-phase Isolated AC-DC Converter Topology

Figure 2-4 illustrates the proposed AC-DC converter topology, with three 1-phase MF transformers and a single 3-phase transformer, respectively. While a single 3-phase transformer can be a cheaper option compared to three 1-phase transformer bank, operating at higher frequencies can cause flux imbalance. So a dummy fourth leg can be included in the design to avoid saturation due to unintended low frequency components or resonances as in Figure 2-5. The remaining of this section explains the topology considering separate 1-phase transformers. The design of the converter can be broadly divided into the following main sub-sections: AC-AC converter, HF or MF transformer, 1-phase boost PFCs, modulation schemes and control strategy, which are explained in detail further in this section.

2.2.1. AC-AC Converter

There are three 1-phase unidirectional AC-AC converters in the proposed topology. The front-end can be constructed using AC-AC full-bridges with bidirectional switches (see Figure 1-10) or using a 1-phase diode bridge and a 1-phase inverter H-bridge (with IGBTs or FETs) connected bact-to-back (since power transfer is unidirectional) with de-coupling capacitors as shown in Figure 2-4 [26, 39]. In order to interface to a 208V, f_s = 60Hz 3-phase utility grid, 450V or lower rated standard IGBTs or MOSFETs will be sufficient. The AC-AC converter in each phase is modulated with a high frequency (HF) or medium frequency (MF) square wave ($f_{sq} = \omega_{sq}/2\pi$). The phase A utility voltage- V_a, the AC-AC converter switching function- S_{acac}, and the transformer primary voltage of phase A- $V_{pri,A}$, can be given by (2.1), (2.2) and (2.3):

(2.1)

$$V_a = \sqrt{2} \cdot V_{a,rms} \cdot \cos(\omega_s \cdot t)$$

$$S_{acac} = \frac{4}{\pi} \cdot \sum_{n=1,3,5\ldots}^{\infty} \frac{1}{n} \sin\left(n \cdot \omega_{sq} \cdot t\right) \tag{2.2}$$

$$V_{pri,A} = V_{a,rms} \cdot \begin{bmatrix} 0.9 \cdot \sin\left(\{\omega_{sq} \pm \omega_s\} \cdot t\right) \\ +0.23 \cdot \sin\left(\{3\omega_{sq} \pm \omega_s\} \cdot t\right) \\ +0.15 \cdot \sin\left(\{5\omega_{sq} \pm \omega_s\} \cdot t\right) \\ + high\ order\ terms \end{bmatrix} \tag{2.3}$$

Unlike the conventional topologies (see Figure 2-2 for example), the input voltage in the proposed topology is simply rectified to get a pulsating (weak) DC that is fed to the 1-phase inverter. The voltage fed to the transformer primary has a sinusoidal envelope that is obtained by multiplying the utility sinusoidal voltage and a HF/MF square wave. From (3), it can be seen that the transformer primary voltage $V_{pri,A}$ has frequency components only around the square wave switching frequency, f_{sq} and not at low frequencies. This enables the use of HF or MF transformers, hence reducing the size. Further, even if the frequency of AC input (V_a) varies slightly, the transformer operating frequency does not change much proportionately. This property makes the proposed topology (with slight modifications) attractive for wind turbine and adjustable speed drive (ASD) applications where the operating frequency may vary.

2.2.2. Medium or High Frequency Transformer

The High frequency (HF) or Medium frequency (MF) transformer forms a critical part of the system. While HF transformers may be preferred for relatively lower power applications (say within 50 kW - 100 kW), MF transformers may be used for even higher power applications. With the conventional line frequency transformers that are

constructed using silicon steel core (magnetic flux density of around 1.2 T to 1.5 T), the core loss is not too large as the line frequency is low. But if it is desired to reduce the size of the system by increasing the silicon steel transformer core frequency, the core losses also increase. To an extent, this increase in losses can be compensated by reducing the magnetic flux density to around 0.3 T to 0.6 T; this also helps in reducing the possibilities of core getting saturated. This strategy can work until certain 'medium frequencies' around 1 kHz to 1.5 kHz, at a lower transformer cost since the silicon steel core material used is much lesser (a *1000 Hz, 0.4 T* MF transformer with silicon steel core can be approximately *one-fourth* the size of a *60 Hz, 1.5 T* line frequency transformer for the same core losses). These aspects are explained in much more detail in section 6.

Beyond this MF range, it becomes necessary to employ amorphous silicon core or powdered iron core because the audible noise increases significantly and it becomes difficult to optimize the system for losses. But this adds to the cost of the transformer and the audible noise issues may not be solved completely. If much higher transformer operating frequencies are desired to further reduce the size, ferrite or nano-crystalline cores would be more suitable. For high power applications beyond a few hundred kilowatts, usage of ferrite core transformers get complicated due to high corona effects and possible flux leakage. The power converter losses also increase significantly. In such cases, it is more appropriate to design and use MF transformers.

If 'β' is the boost PFC gain (~ 1.5 to 2.0) and V_{dc} is the required DC output voltage, the required transformer turns-ratio, N can be calculated as per (2.4). For a

208V_{LL} utility input, 200V_{dc} DC voltage and for a β value of 1.5, the transformer turns ratio is approximately n_2:n_1 = 6:5.

$$N = \frac{n_2}{n_1} = \left(\frac{\pi}{2\sqrt{2}\cdot\beta}\right)\cdot\left(\frac{V_{DC}}{V_{a(rms)}}\right) \tag{2.4}$$

As discussed earlier, since the modulation is in such a way that the AC-AC converter output voltages add to zero, the net magnetic flux will always be balanced ideally even if a single 3-phase MF transformer is used instead of three 1-phase transformers. But in practice, there will be slight imbalances caused by converter operation, resonances, etc. To compensate for these imbalances, a thin fourth leg can be added to the 3-phase core in order to avoid saturation, as shown in Figure 2-5.

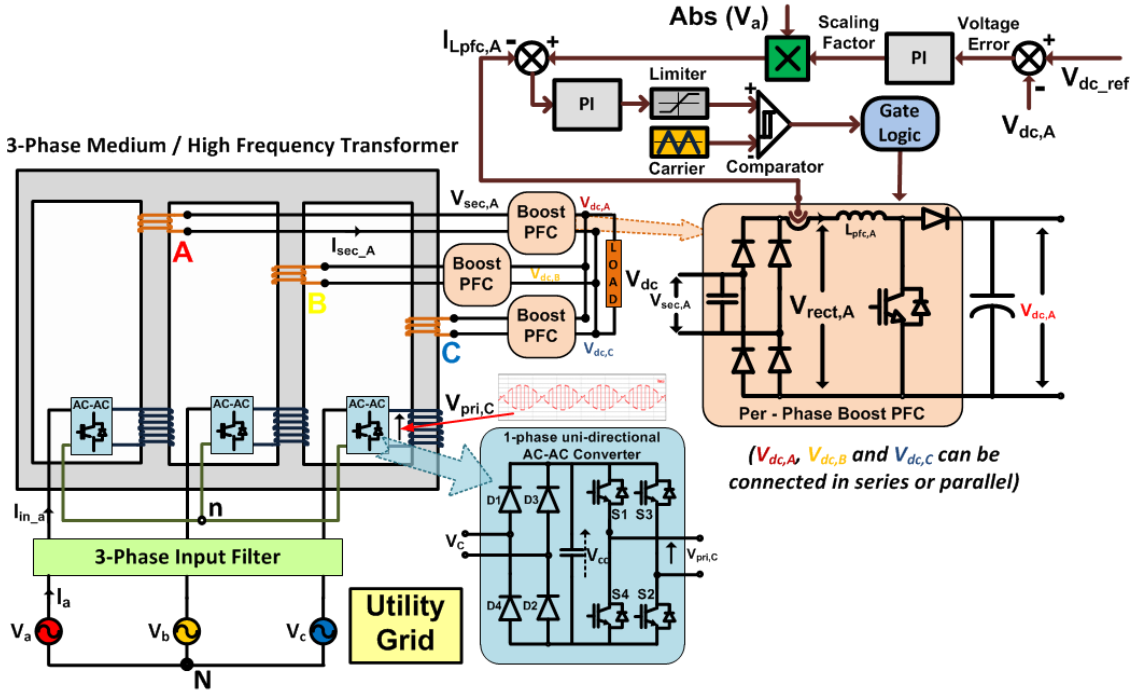

Figure 2-5: Proposed converter with a single 3-phase transformer instead of three 1-phase transformers

2.2.3. 1-phase Boost PFC Stage

The transformer secondary voltage is a 'flipped sine wave' (product of line frequency sine and HF/MF square wave as shown in Figure 2-4, slightly smoothened due to the filtering action of the transformer leakage inductance. The diode rectifiers of the boost PFC stage convert this flipped sine wave into full-wave rectified (twice-the-line-frequency) waveform. It should be noted that even though the transformer frequency is HF or MF, the diode rectifiers switch at that frequency and the rectified voltages look similar to the rectified voltage waveforms of the weak DC-link on the primary side. After this, the remaining boost converter section operates like the one in a conventional boost PFC, making the inductor current in phase and shape as the rectified voltage. Hence the design of this topology is straight forward.

The switching devices in the boost PFC stage have to be rated at least at the peak output DC voltage. If the output DC voltage has to be regulated at 200 V, then the boost PFC switches have to be rated at 350V. It is important to note that the output voltage, V_{dc} must be equal to or greater than the peak rectified voltage. The design equations for the PFC inductors L_{PFC} and the effective output capacitors C_{dc} can be given by (2.5) and (2.6). As a design rule considered, the inductors must make the boost PFC operate at continuous conduction beyond 20 % load, thus the current ripple must be less than 20 % of load current at the peak rectified voltage. Assuming the peak voltage across the inductor is V_{dc}, if 'D' is the duty cycle, 'f_{sw}' is the switching frequency and $i_{p\text{-}p}$ is the ripple current peak-to-peak (equal to 20% of load current),

$$L_{PFC} = \left(\frac{D \cdot V_{DC}}{f_{sw} \cdot i_{p-p}}\right) \tag{2.5}$$

Since the boost PFC outputs are connected in parallel, the 2nd harmonic ripples of the three phases get cancelled and hence the capacitor only needs to be designed for the switching frequency of the boost PFC stage. Otherwise, the capacitor design is completely dependent upon the subsequent stage after the PFC. Assuming the PWM signals to the PFCs for the three phases are phase shifted by 120°, the ripple voltage across the capacitor will be at thrice the switching frequency. As a thumb rule, the capacitor can be designed as:

$$C_{DC} = \left(\frac{i_{p-p}}{2 \cdot \pi \cdot f_{sw} \cdot v_{p-p}}\right) \tag{2.6}$$

where $v_{p\text{-}p}$ is the ripple voltage pk-pk allowed at the output capacitor. If $i_{p\text{-}p}$ = 4 A, f_{sw} = 3.6 kHz, V_{dc} = 200 V, D = 0.2 and $v_{p\text{-}p}$ = 10 V, then $\boldsymbol{L_{PFC}}$ **~= 2.5 mH** and $\boldsymbol{C_{DC}}$ **~= 25 uF**. A 330 uF capacitor is chosen to support the subsequent stage.

2.2.4. Control Strategy

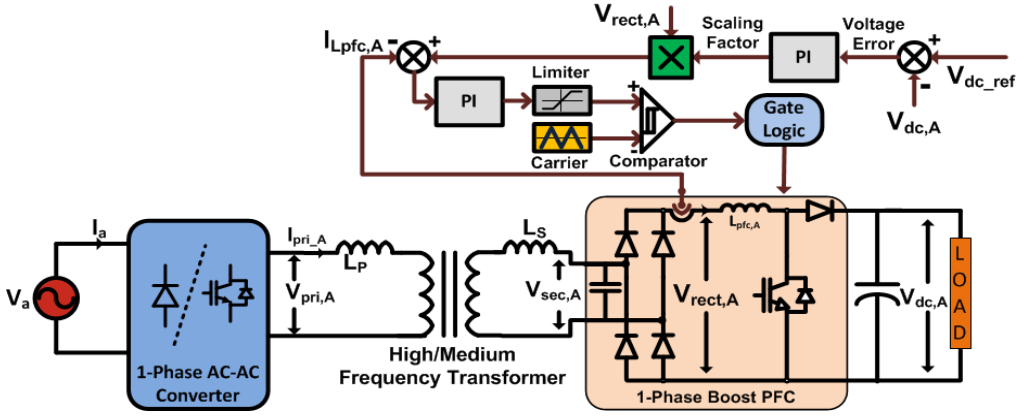

Figure 2-6: Single-phase equivalent circuit with control system for the proposed topology (Figure 2-4)

It should be noted that there is no closed loop control involved on the primary side of the proposed system since the AC-AC converters are operated using simple HF/MF square wave modulation. The utility input current and output DC voltage are regulated through the control of the boost PFC stage. The control objective is similar to that of the boost PFC stage in a conventional AC-DC converter (Figure 2-2), which is to emulate an active resistor that makes the input current's shape and phase follow that of the input voltage. Here the boost PFC stages try to make the transformer currents' shape and phase follow that of the primary voltages, $V_{pri,ph}$. Figure 2-6 depicts the control strategy employed in proposed topology. Depending upon the load power, the magnitude of the PFC inductor current, $I_{Lpfc,A,}$ is varied by adjusting the scaling factor that is generated from the output DC voltage ($V_{dc,A}$) regulation; keeping the shape same as that of the rectified voltage, $V_{rect,A}$. Since $V_{rect,A}$ is the same as the rectified voltage of a conventional boost PFC system, the design and control here are similar to a conventional boost PFC.

The inner current control loop must be faster than the outer voltage loop. For tuning the control parameters, methods such as Ziegler Nichols can be used. When the DC outputs of the boost PFC stages corresponding to the three phases are connected either in series or parallel, the second harmonic power gets cancelled and hence the DC capacitor need not be very large. In the topology shown in Figure 2-2, the DC capacitors at the output of the boost PFC stages on the transformer primary side need to suppress the second harmonic current ripple will be large. This is a notable advantage of the proposed topology. Other advantages are reduction in size and switching losses, which

are explained in the next section. The utility currents will have small twice the MF components due to transformer current transients; these are filtered using LC filter [27].

2.3. Size and Loss Comparison

The major difference between the conventional AC-DC topology in Figure 2-2 and the proposed system in Figure 2-4 is that there is no stiff DC link in the primary side of the transformer in the proposed topology. An advantage having a weak DC-link on the primary side, apart from avoiding large electrolytic capacitors, is that since the AC-AC converter is switched with identical square wave in all the three phases, the net flux in the transformer will be balanced even if a single 3-phase transformer is used as shown in Figure 2-5. In the topology in Figure 2-2, due to a stiff DC-link on the primary side, either three 1-phase transformers need to be used or resonant power conversion strategy (like LC or LLC resonant soft-switching) needs to be used. This increases the system size. Moreover, if same devices are used in both cases, the voltage stress on the devices is lower here than in the conventional topology.

Another advantage of having a pulsating DC link on the primary side is that the switching losses are lower. Since the switching loss is proportional to the product of the DC-link voltage and current, if the average value of DC-link voltage is lower, the switching losses are lower (for the same rms current). Hence the switching losses with pulsating DC-link may become ($2/\pi$) times (~35% reduction) for the H-bridge.

A disadvantage of the proposed topology is that due to the presence of diode rectifiers on both the AC-AC converter front end and boost PFC front-end, supplying

non-unity power factor on the utility side can result in increased harmonic distortion. Also, the diode rectifiers on the boost PFC stage need to operate at HF/MF. But since most utility interface systems require unity power factor at the input and due to the increased availability of fast-switching rectifiers, these disadvantages do not possess significant challenges, at least for MF transformer based applications. Size and loss analysis for the proposed MF/HF transformer based topologies will be explained in detail in section 6.

2.4. Simulation and Experimental Results

Table 2-1: Simulation parameters and values

Parameters	Values
Input AC	208 V_{LL}, 60 Hz, 3-phase
Output DC Load	200 V, 4 kW
Transformer Core	Silicon Steel, 600 Hz (MF)
Transformer Leakage	0.05 p.u. per winding
Input AC filter capacitance	0.1 mF
DC side filter capacitance	330 uF
Boost PFC Switching Frequency	3.6 kHz

The topology in Figure 2-4 was simulated using PSIM. The specifications of the system are provided in Table 2-1. Figure 2-7 and Figure 2-8 show the important waveforms obtained during the simulation of the proposed topology using a resistive load of 4 kW. It can be seen from Figure 2-7 (a) that the utility input voltage and current are in phase and the current has very low harmonics. Figure 2-7 (b) shows the primary side rectified voltage and current at the weak DC-link of the AC-AC converter. There

are some resonances seen in the current, which is due to the input filter inductance and coupling capacitor. Figure 2-7 (c) shows the MF/HF transformer primary voltage and current, which are again in phase and similar in shape.

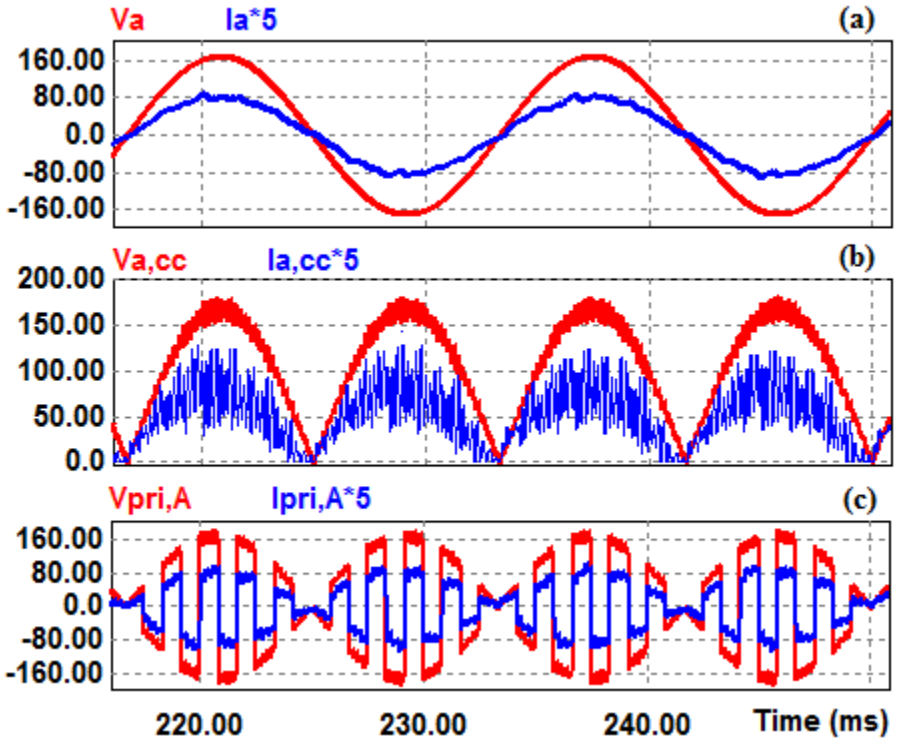

Figure 2-7: Simulation waveforms of the transformer primary side of the proposed topology - (a) Utility input phase-A voltage and current (*scale increased for better resolution of current*); (b) Pulsating DC-link voltage and current; and (c) Transformer primary phase-A voltage and current

Figure 2-8 shows the simulation waveforms on the secondary side of the transformer. Figure 2-8 (a) shows the transformer secondary phase-A voltage and current (with MF 'flipped sine' wave voltage). Figure 2-8 (b) shows the rectified voltage and inductor current of phase-A voltage and current at the PFC stage, which works with MF/HF input. It can be seen that even though the input to the PFC stage is the 'flipped sine' wave, the rectified voltage and current are in phase and very similar in shape

compared to the weak DC-link voltage at the AC-AC converter. There are some small distortions in the PFC rectified voltage, $V_{rec,A}$ that are caused due to the transformer leakage inductance. Figure 2-8 (c) shows the output DC voltage along with the three phase PFC currents on the transformer secondary side. It is clear that the output DC voltage is higher than the peak of the rectified DC value. Also, the 2nd harmonic ripple is not seen at the output DC, which are cancelled by the three phases connected together.

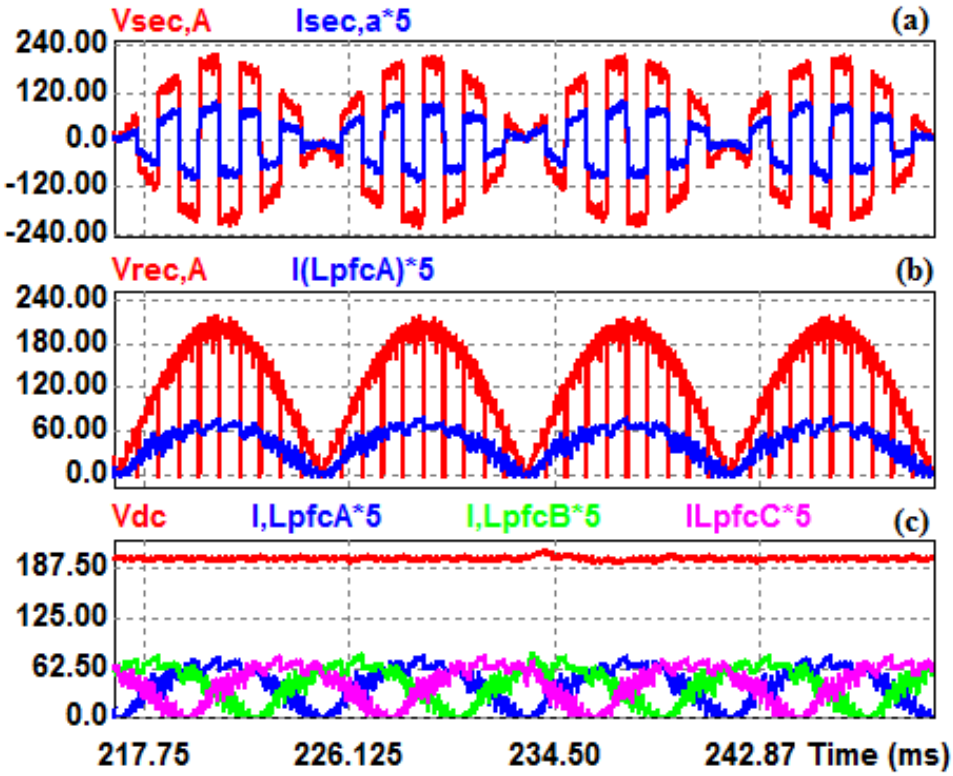

Figure 2-8: Simulation waveforms of the transformer secondary side of the proposed topology with boost PFCs- (a) Transformer secondary phase-A voltage and current (*scale increased for better resolution of current*); (b) Rectified PFC pulsating DC-link voltage and current; and (c) Load DC voltage and the three phase PFC inductor currents, phase shifted.

Experiments were carried out on scaled-down 1-phase prototypes with modulation and control implemented using TI Delfino TMS320F28335 microcontroller. Two transformers were used, one with silicon steel core with 600 Hz operating frequency and the other for operating at 6 kHz. In order to confirm that the topology and control would work as in a conventional boost PFC, a standard Murata power supply - *MVAC400* was used (after eliminating the effects of its EMI filter) on the secondary side of the transformer, which has a boost PFC active front end. The waveforms, when operated with a 600 Hz transformer of turns-ratio 1:1 (primary side AC-AC converter operating at 600 Hz), are shown in Figure 2-9. It can be seen that the experimental waveforms are similar to the simulation results. There are some small spikes in the transformer current, which is due to the slight mismatch in the zero crossing detection of the *MVAC400* power supply coupled by the transformer leakage inductance.

Figure 2-10 shows a step response on the DC load by 50 %. It can be seen that the utility current is still in phase with the voltage and the output DC voltage is regulated at 60 V. The transformer voltages and currents are also similar as in simulation waveforms. Figure 2-10 shows that the control of the *MVAC400* power supply could maintain the output voltage constant even in this application under a 50 % load step change. This proves the simplicity in the control of the proposed topology, which is comparable to a conventional boost PFC. There are some small spikes in the utility input current, which are caused due to the transformer leakage inductance.

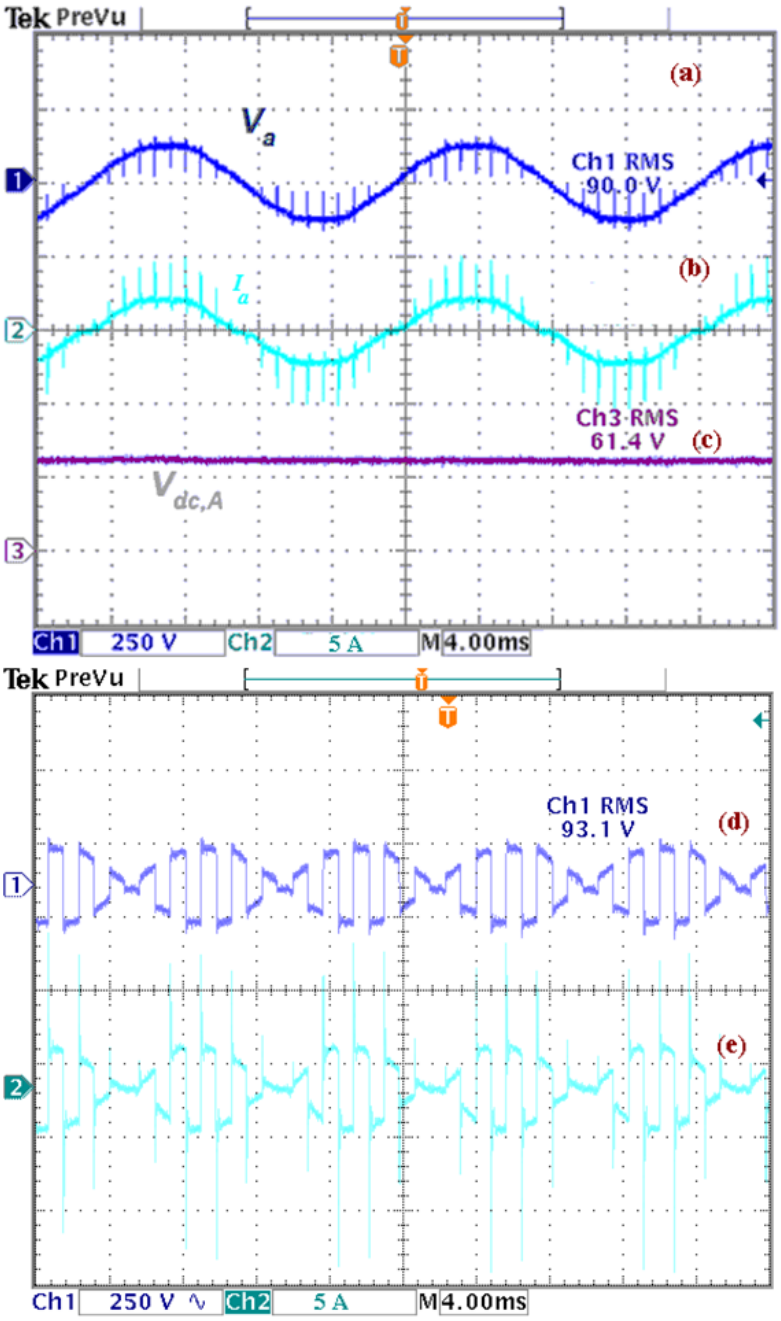

Figure 2-9: Experimental waveforms with 600 Hz transformer - (a) Utility input voltage V_a, (b) Utility input current I_a, (c) Output DC voltage V_{dc}, (d) Transformer primary voltage $V_{pri,A}$, and (e) Transformer current $I_{pri,A}$

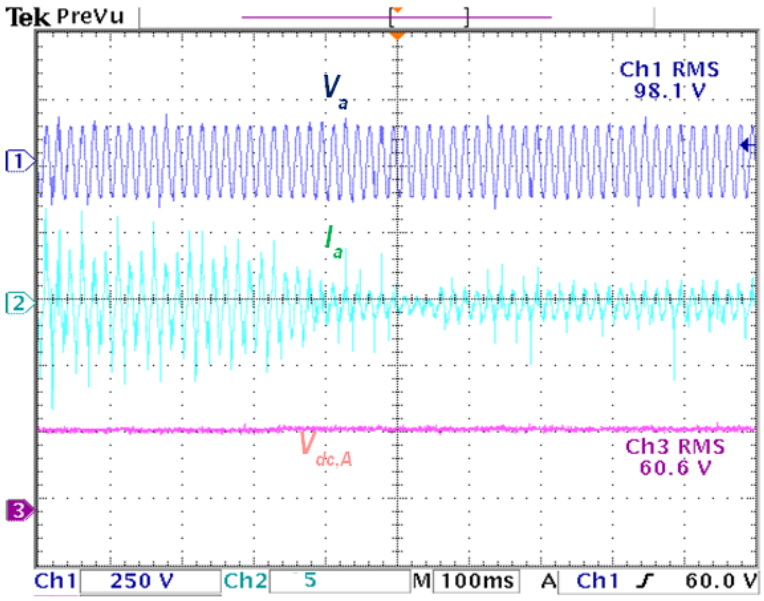

Figure 2-10: Experimental waveforms of the proposed topology with 600 Hz transformer - (a) Utility input voltage V_a, (b) Utility input current I_a, (c) Output DC voltage V_{dc}

To test the functionality of the converter using a HF transformer, the same topology was tested this time with a 6 kHz transformer. It can be seen from Figure 2-11 that the topology works similar with HF transformer too. Moreover, from the rectified voltage $V_{rect,A}$, it can be seen that it is still twice the line frequency ripple as expected. But small distortions can be seen at utility current zero-crossings, which are again due to the slight mismatch in zero-crossing detection caused by the transformer leakage inductance and *MVAC400* operation. However in a typical system with customized design, the zero-crossing detection can be performed more precisely and thus some of these distortions can be reduced. Hence this exercise shows that the conventional PFC topology itself can be used in this application with different transformer core frequencies with only small modifications in component selection.

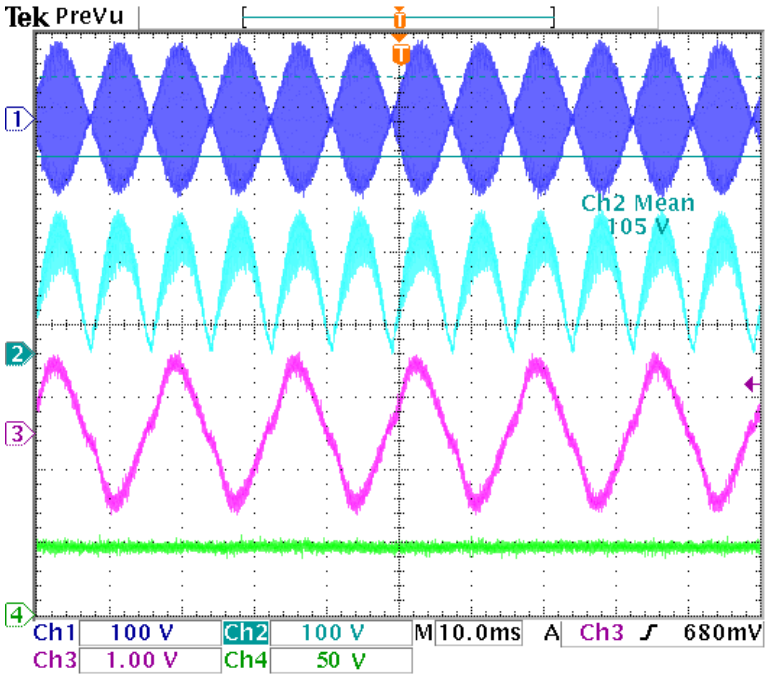

Figure 2-11: Experimental waveforms with 6 kHz transformer - (Ch. 1) Transformer primary voltage $V_{pri,A}$, (Ch. 2) Secondary side rectified voltage V_{rect}, (Ch. 3) Utility input current I_a, and (Ch. 4) Output DC voltage V_{dc}

2.5. Conclusion

An isolated AC-DC converter topology using high or medium frequency transformers has been presented in this section and its operating principles were explained. Simulation and experimental results validated the operation of the proposed system. Overall the new topology enables higher power density AC-DC conversion due to the elimination of electrolytic capacitors and usage of MF or HF transformers instead of a line frequency transformer. The control strategy is simple and conventional. The topology appears to be promising for a wide range of 3-phase high power applications like EV charging, telecom power supply, ASDs, server power conversion, etc.

3. SIMPLIFIED MEDIUM/HIGH FREQUENCY TRANSFORMER BASED MULTI-PULSE DIODE RECTIFIERS

3.1. Introduction to Adjustable Speed Drives and Multi-Pulse Rectifiers

Electric motors are an integral part of modern life and industrial production. There are more than 300 million motors installed worldwide in industries including oil and gas, petrochemicals, cement, transportation, steel and other heavy manufacturing. This figure grows each year by more than 10% and it is estimated that the motor market around the world will exceed US$ 60 billion by the year 2017. Advanced inverter configurations such as Variable Speed Drive (VSD) and Adjustable Speed Drive (ASD) have facilitated easier speed and torque control of AC motors and contribute to significant energy savings [42]. The introduction of improved power electronic topologies, development of robust motor-control techniques, and advancements in state-of-the-art semiconductor technologies like fast-switching silicon carbide (SiC) wide-band gap power devices have helped in precision regulation of speed and position [43, 44]. The aforementioned developments in ASDs offer several benefits, such as energy savings, improved process control, improved system reliability and smoother operation [13]. Further improvements in the design of power electronic inverters, utility grid interface transformers, and electric motors could reduce the cost and size of these systems and offer total savings of up to US$ 2 trillion in two decades [13].

ASDs offer several benefits, some of which are relatively easy to quantify and others of which are less tangible. The major advantages are energy savings, improved

process control, improved system reliability and smoother operation [13]. Medium voltage adjustable speed drive (MV-ASD) systems offer significant advantages in fan, pump and many process control applications with higher efficiencies combined with energy savings over a wide range of speed settings. MV-ASD systems continue to grow at a steady rate and find expanding applications [13, 44-46]. Yet, there are some drawbacks in the state-of-the art ASDs, which must be overcome. Commercial ASD systems primarily consist of a line frequency multi-winding isolation transformer, diode bridge rectifiers (12-pulse or 18-pulse) and multi-level or NPC (Neutral Point Clamped) inverters [47-50]. This configuration makes the drive size large due to the bulky line frequency transformer as well as the large DC-link capacitors as in Figure 3-1.

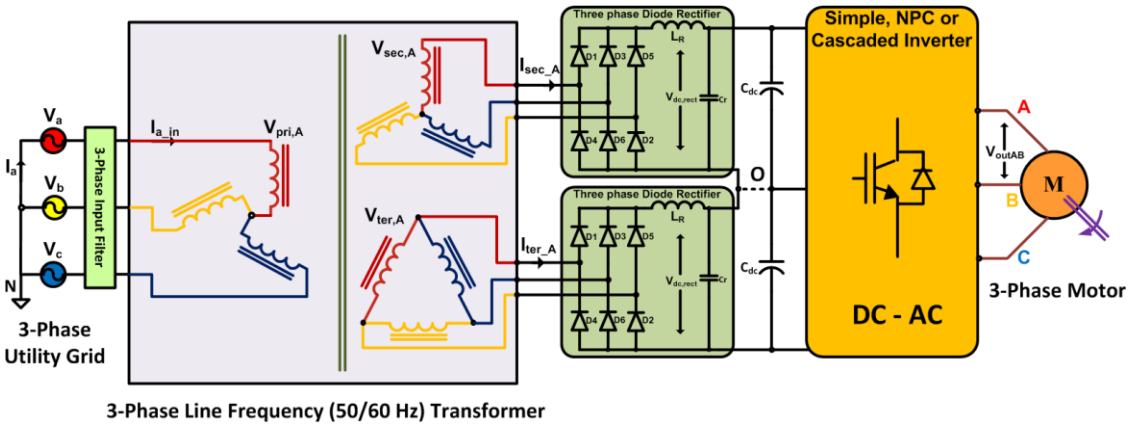

Figure 3-1: Commercial motor drives (Note the bulky 60 Hz transformer and diode bridge rectifiers)

Several AC-DC rectifier topologies employing MF and HF transformers have also been proposed [49-51]. Though these topologies offer higher density of power conversion, many of them use large DC electrolytic capacitors and have sophisticated control strategies. In order to reduce or eliminate the harmonics, Ref. [43] proposes an

active filter concept. This however, requires additional switches including energy storage elements. Moreover, the issue of bulky line frequency transformers still remains.

Commercial MV-ASD systems are mostly voltage source inverter (VSI) type and sometimes current source inverter (CSI) type. They mainly consist of a line frequency multi-winding isolation transformer, diode bridge rectifiers (24-pulse or 36-pulse configuration) and simple, cascaded or NPC inverters [13, 45, 46]. The line frequency transformer based configurations make the motor drive size larger due to the bulky magnetics as shown in Figure 3-1. Depending on the chosen multi-winding transformer configuration, line frequency current harmonics will be different. Such topologies are employed in industries such as oil and gas, aircrafts, wind turbines, etc. as well [51]. For simplicity, this section explains the 12-pulse rectifier operation, whose theory can be extended to higher configurations.

The 12-pulse rectifier shown in Figure 3-1 has a line frequency transformer followed by 3-phase diode rectifiers. The line frequency (50 Hz or 60 Hz) transformer can be constructed using a single 3-phase transformer or three 1-phase transformers, as explained earlier. The primary of the transformer is connected in star and the secondary windings are connected in star-delta configurations, with the number of windings in the delta structure '√3' times that on the star-structure. This is done to create a 30^o phase shift between the voltages applied to the diode rectifiers (V_{sec} *and* V_{ter}), while keeping the same line-to-line voltage magnitudes. This configuration creates a 30^o phase shift between the input currents of the diode rectifiers (I_{sec} *and* I_{ter}), improving the current quality of the transformer primary current (I_{a_in}) as well as the net DC voltage output

from the rectifiers (12-pulse waveform). The operation waveforms of the 12-pulse rectifier in Figure 3-1 are shown in Figure 3-2.

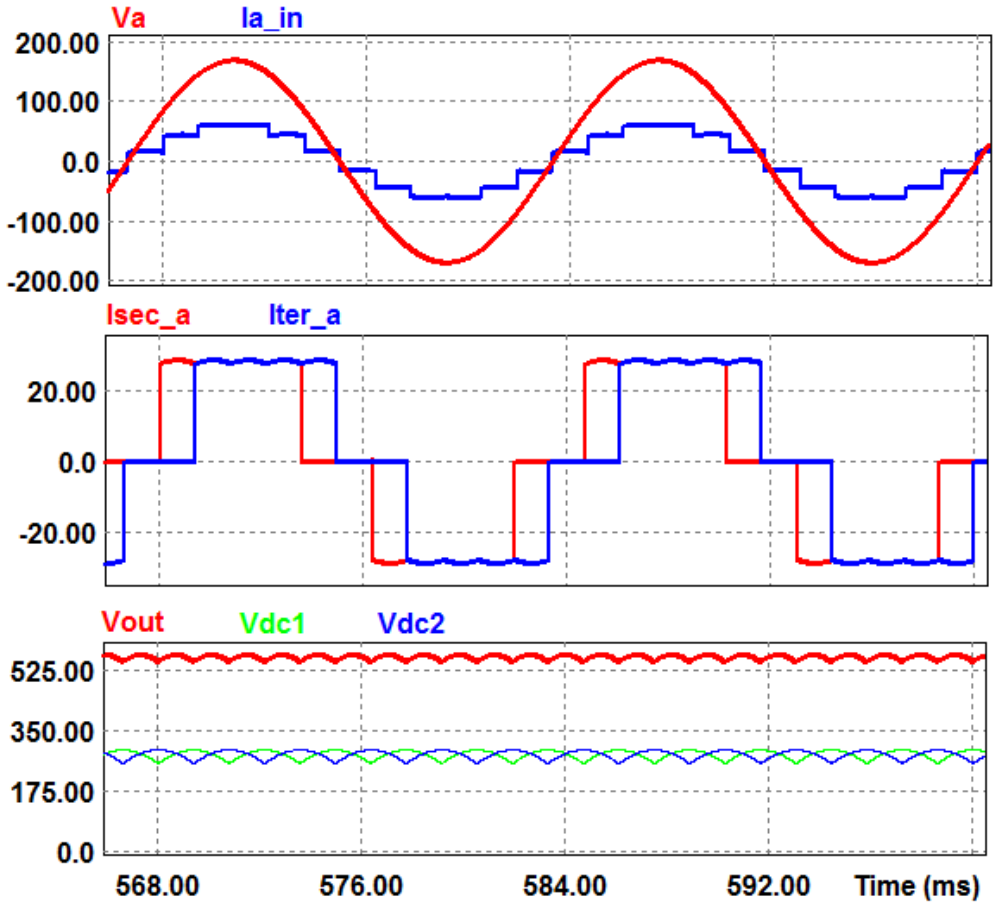

Figure 3-2: Waveforms of the conventional 12-pulse rectifier topology shown in Figure 1.

From Figure 3-2, it can be seen that though the currents on the secondary and tertiary sides of the transformer (I_{sec_a} *and* I_{ter_a}) only have three levels, the net primary current, I_{a_in} has six levels. The secondary and tertiary side currents have the fundamental frequency component and have 5^{th} and 7^{th} harmonics as the primary harmonic content. But due to the star-delta configuration of the 12-pulse rectifier, the 5^{th}

and 7^{th} harmonics cancel and the transformer primary current has only much smaller 11^{th} and 13^{th} harmonics as the primary content. Thus the net THD of the converter input current is improved over a conventional 6-pulse 3-phase rectifier. This technique has become very popular in the motor drive industry for high power applications. A major disadvantage of the conventional 12-pulse rectifier is that it needs a bulky line frequency (50/60 Hz) transformer for creating the 30^{o} phase-shift. As seen in section 1, this can typically contribute to almost 60-80 % of the total weight/volume of the system. Any reduction in the transformer weight or volume can be significant.

3.2. **12-pulse Rectifier using Higher Frequency Transformer**

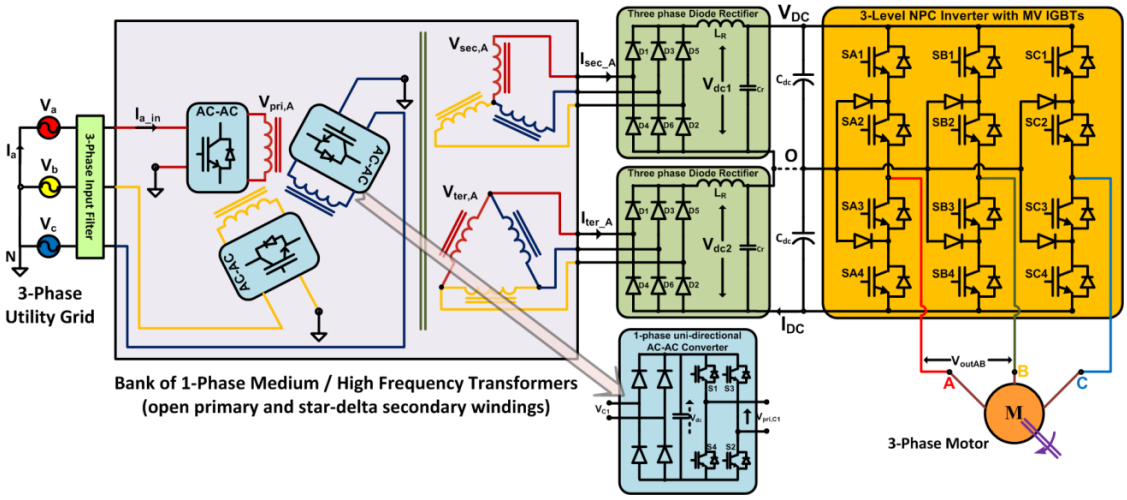

Figure 3-3: Proposed MV-ASD topology with MF/HF isolation with 12-pulse rectifier front-end

Employing MF or HF transformers can improve the power density of isolated power converters significantly. There has been renewed interest in Solid-state transformers (SST) due to the improvement in semiconductor device technology. Newer wide band-gap devices, such as Silicon Carbide (SiC) MOSFETs/diodes are able to

switch much faster due to lower losses. Based on the voltage and power ratings, different types of SSTs have been proposed, with frequencies ranging from 1 kHz to 20 kHz [47].

This section introduces a simplified medium frequency (MF) or high frequency (HF) transformer based multi-pulse rectifier system with unidirectional AC-AC converters at the input side. The diode bridge rectifier on the transformer secondary side and NPC inverter look similar to the conventional approach. Figure 3-3 shows the proposed topology. AC-AC converters are employed on the utility input side to convert the 50/60Hz line frequency voltage to higher frequency AC. The output of the AC-AC converters is then interfaced with medium/high frequency (MF/HF) transformer constructed with electrical steel or other advanced low loss magnetic materials. The secondary of the transformer constitute standard multi-pulse windings that power the rectifier DC-link, inverter systems.

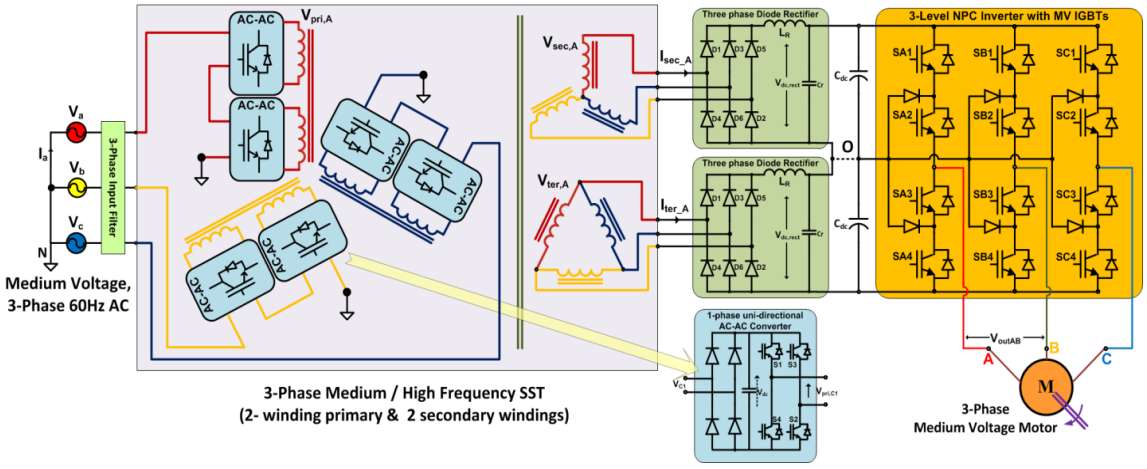

Figure 3-4: Proposed Medium Voltage ASD with series-stacked/cascaded AC-AC converter structure

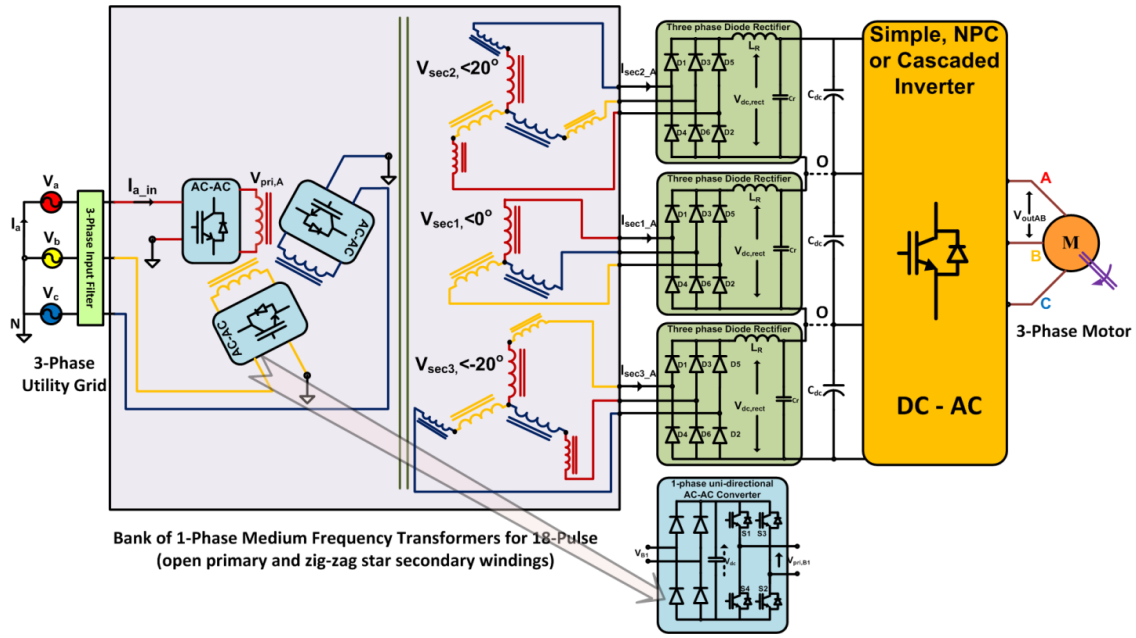

Figure 3-5: MF/HF Transformer based 18-pulse rectifier configuration

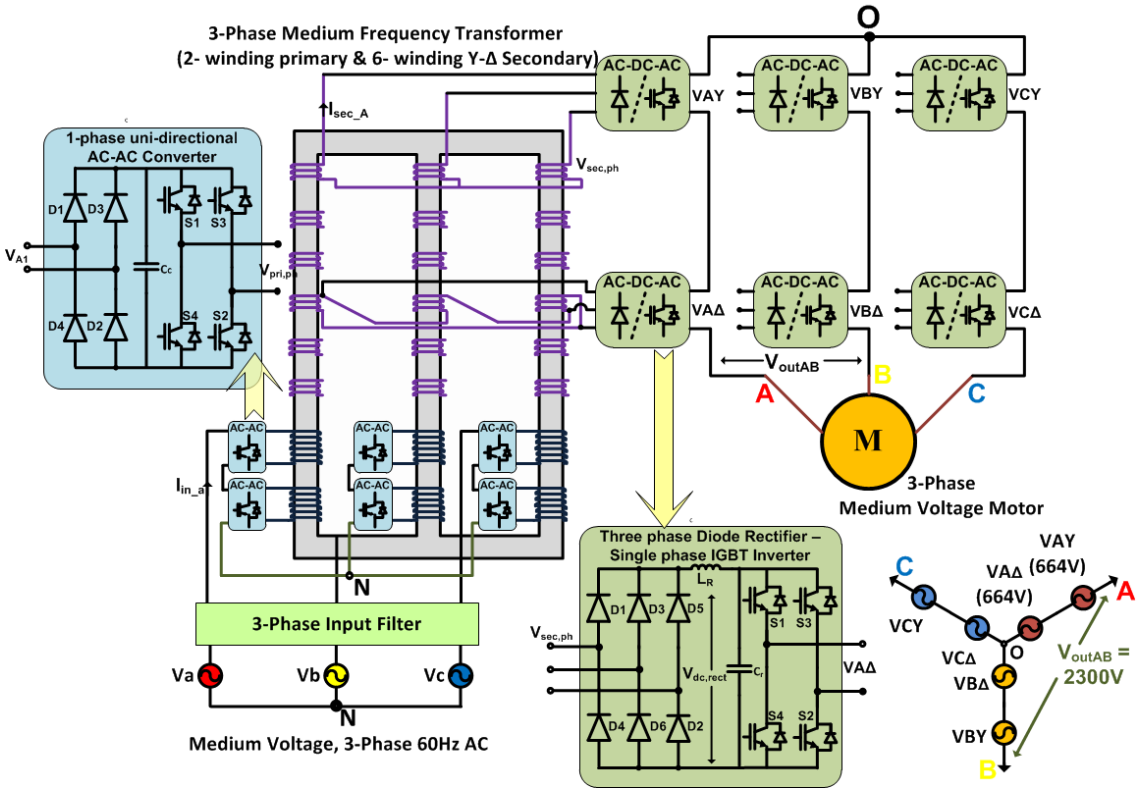

Figure 3-6: Proposed medium voltage adjustable speed drive (MV ASD) topology with medium frequency (MF) isolation with series-stacked inverter modules in the transformers secondary (derived from [52])

Figure 3-4, Figure 3-5 and Figure 3-6 show various modular ASD alternatives to the proposed topology in Figure 3-3 with higher frequency transformer isolation that have the same basic concept, but can be used under different application requirements. If the 12-pulse rectifier in Figure 3-3 has to be interfaced with a higher medium voltage (MV) utility, then a single level of AC-AC converters may not be able to withstand the entire voltage or may be sub-optimal. Then, multilevel AC-AC converters can be used as shown in Figure 3-4. The number of levels stacked in series depends upon the MV interfaced with. The capacitors at the AC-AC converter along with the transformer magnetizing inductance help in balancing the voltage across the different levels of AC-AC converter. In a large power system, resistive voltage dividers are also employed.

Figure 3-5 shows another extension of the proposed topology for 18-pulse configuration. Even higher configurations such as 24-pulse, 36-pulse, etc. are possible just by changing the MF/HF transformer arrangement similar to the corresponding conventional configuration. Figure 3-6 [53] shows stacked single phase inverters on the secondary side, as an alternative to [52, 54], suitable for high voltage high power motor drives. These variations make the proposed concept suitable for applications such as aircrafts, MV-DC inter-connection, etc. The approach is flexible and easily extendable as per the application. The advantages of the proposed system [53] are as follows:

- Employing MF/HF transformer reduces the system size [46, 50].
- Retrofit replacement of bulky line frequency transformer with MF/HF based ‘solid state transformer’ (SST).
- Primary side AC-AC converters work in simple open loop square wave modulation.

- Use of wide band-gap SiC power semiconductor devices at high frequencies, along with amorphous/ferrite core transformer will further enhance the system efficiencies.
- Passive components including the input filter, DC bus capacitor, etc. can be designed in a similar way as in a typical 12-pulse or higher pulse rectifier system.
- The use of series stacked AC-AC converters for generating medium/high frequency is inherently fault tolerant. Under converter fault conditions, one or more of the series stacked AC-AC converter modules can be actively by-passed.

As discussed, the proposed concept can be extended to 18-pulse, 24-pulse and other configurations as well, but this section focuses on design, working principle, simulation and experiments on 12-pulse rectifier system for simplicity in explanation and demonstration, considering the operation of higher configurations can be deduced from this system. Moreover, the focus of this section is on the front-end of an ASD system, so the inverter operation is not discussed in detail. The inverter is assumed to be similar to the ones in conventional ASDs, which can be simple, NPC or cascaded. The Figure 3-3 shows the motor drive inverter as a 3-level NPC structure. The design of the front-end of the proposed ASD system can be mainly divided into the following sub-sections: (i) AC-AC converter, (ii) 3-phase diode rectifier, (iii) HF or MF transformer, and (iv) Passive components.

3.2.1. AC – AC Converter and Modulation Scheme

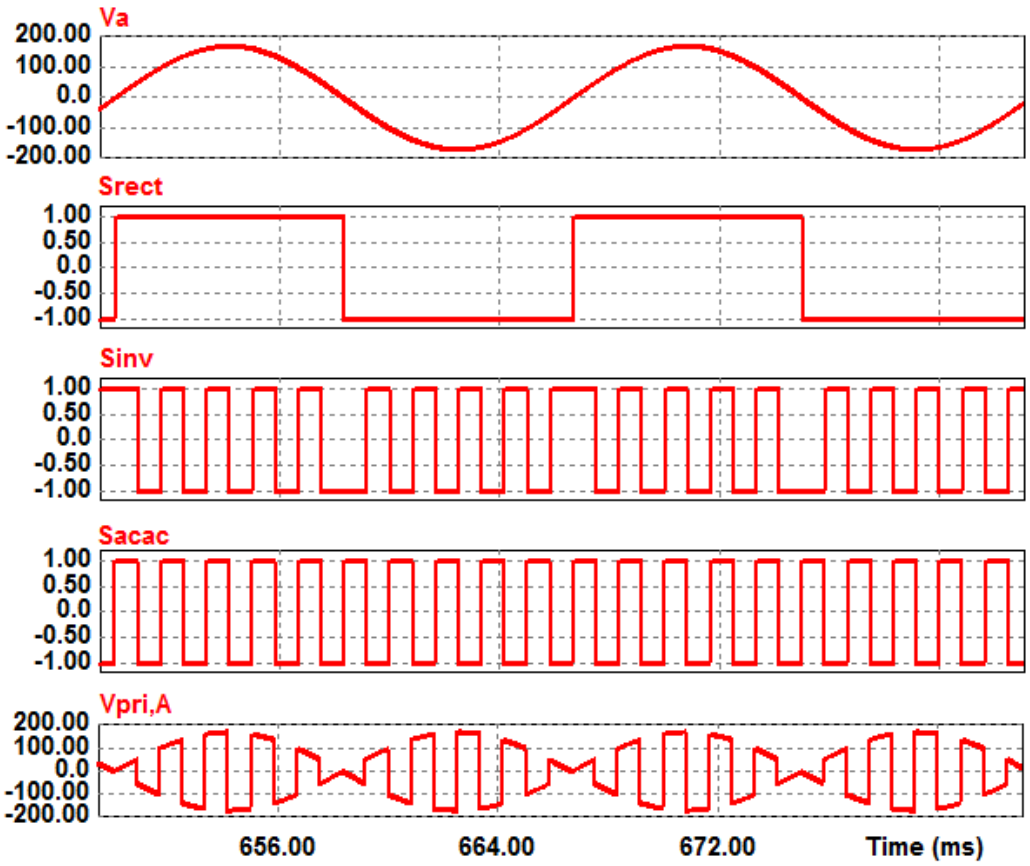

Figure 3-7: AC-AC Converter voltages and switching functions

The AC-AC converter for each phase can be made up of back to back 1-phase H-bridges with IGBTs coupled by small thin film capacitors or simply a 1-phase diode bridge followed by a H-bridge (since power flow is unidirectional) as shown in Figure 3. In order to interface to a *690* V_{LL}, $\boldsymbol{f_s}$ = 60 Hz utility grid, 1200 V or lower rated standard IGBTs will be sufficient. The AC-AC converter in each phase is modulated with a medium or high frequency ($f_{sq} = \omega_{sq}/2\pi$) square wave. The phase A utility voltage- V_a, the AC-AC converter switching function- S_{acac}, and the transformer primary voltage of

phase A- $V_{pri,A}$, can be given by eqns. (2.1), (2.2) and (2.3) discussed in section 2.2.1. The modulating square wave must be synchronized across the three phases. This is done in order to make the net flux balanced on the primary side of the transformer, which can be achieved if the net sum of primary voltages → $V_{pri,A} + V_{pri,B} + V_{pri,C}$ is equal to zero ($= 0$) at every instant.

The voltage fed to the transformer primary has a sinusoidal envelope that is obtained by multiplying the utility sinusoidal voltage and a HF/MF square wave. From (3), it can be seen that the transformer primary voltage $V_{pri,a}$ has frequency components only around the square wave switching frequency, f_{sq} and not at low frequencies. This enables the use of HF or MF transformers, hence reducing the system size. Further, even if the frequency of AC input (V_a) varies slightly, the transformer operating frequency does not change much. This property makes the proposed topologies (with slight extensions) attractive for applications where the input frequency can vary over a wide range. It should be noted that the switching function of the AC-AC converter overall, represented as S_{acac} in eqn. (2), is MF/HF square wave. But the diode rectifier section of the AC-AC converter introduces a switching function of a line frequency square wave (S_{rect}), which must be compensated in the modulation of the H-bridge (S_{inv}) of the AC-AC converter by multiplying the MF square switching function S_{acac} with the diode rectifier switching function. These waveforms are shown in Figure 3-7.

One of the major advantages of the proposed concept is the simplicity in the modulation scheme. No closed loop control scheme is required for the front-end since the topology intends to replicate the performance of a conventional line frequency

transformer. The utility grid voltage zero-crossing has to be sensed to synchronize the modulation signals. The modulation of the AC-AC converters is purely MF or HF square wave. Another advantage of this topology is that if the DC bus voltage is desired to be changed, it is possible to vary and control it by changing the duty-cycle of the AC-AC converter's square wave modulation; a closed loop control would be desired in this case. Moreover in case of a fault on the utility side, it is easy to isolate the ASD system by removing the gating signals since there are no large capacitors on the front-end.

3.2.2. 3-Phase Diode Rectifier (for 12-pulse Configuration)

The 3-phase diode rectifier bridge acts in the same way as in a conventional 12-pulse rectifier, but the diodes have to switch at the MF/HF at which the primary side AC-AC converters operate (depending upon the transformer). Hence, fast-switching Schottky or SiC diodes are preferred for this application. In a conventional 12-pulse rectifier, the switching function of each leg of the 3-phase diode bridge is a quasi-square wave, which is the ideal waveform of the input current of the diode rectifiers (say $I_{sec,A}$ and $I_{ter,A}$ in Figure 3-1). Since the transformer primary voltage, $V_{pri,A}$ has a line frequency envelope over MF/HF square wave, the diode rectifier switching function is also multiplied by the same square wave switching function, which in-turn applies the same switching function on the transformer secondary and tertiary currents as well. The Fourier series expansion of the transformer phase-A currents of the star, delta and the resultant on the primary windings can be respectively given by the eqns. (3.1), (3.2) and (3.3). Note the harmonic terms in the primary current equation.

$$I_{sec,A} = S_{acac} \cdot \left(\frac{2\sqrt{3}}{\pi}\right) \cdot I_{DC} \cdot \begin{bmatrix} \sin(\omega_s \cdot t) \\ -(1/5) \cdot \sin(5 \cdot \omega_s \cdot t) \\ +(1/7) \cdot \sin(7 \cdot \omega_s \cdot t) \\ -(1/11) \cdot \sin(11 \cdot \omega_s \cdot t) + \cdots \end{bmatrix} \quad (3.1)$$

$$I_{ter,A} = S_{acac} \cdot \left(\frac{2\sqrt{3}}{\pi}\right) \cdot I_{DC} \cdot \begin{bmatrix} \sin(\omega_s \cdot t) \\ +(1/5) \cdot \sin(5 \cdot \omega_s \cdot t) \\ -(1/7) \cdot \sin(7 \cdot \omega_s \cdot t) \\ -(1/11) \cdot \sin(11 \cdot \omega_s \cdot t) + \cdots \end{bmatrix} \quad (3.2)$$

$$I_{pri,A} = I_{sec,A} + I_{ter,A} = S_{acac} \cdot \left(\frac{4\sqrt{3}}{\pi}\right) \cdot I_{DC} \cdot \begin{bmatrix} \sin(\omega_s \cdot t) \\ -(1/11) \cdot \sin(11 \cdot \omega_s \cdot t) \\ +(1/13) \cdot \sin(13 \cdot \omega_s \cdot t) \\ -(1/23) \cdot \sin(23 \cdot \omega_s \cdot t) + \cdots \end{bmatrix} \quad (3.3)$$

Now, the utility input unfiltered phase-A current I_{a_in} is obtained by operating the transformer primary current, $I_{pri,A}$ on the AC-AC converter switching function, S_{acac}. Since S_{acac} is a square wave switching function with 50 % duty cycle as shown in Figure 4, multiplication with the same switching function yields a constant '*1.0*'. So the overall unfiltered utility current, I_{a_in} can be obtained as in (3.4). This equation is identical to the input current equation of a conventional 12-pulse rectifier [55]. This proves that introduction of the AC-AC converter and MF/HF transformer does not affect the operation of the entire converter as such, but only replaces the bulky line frequency transformer with a more power dense MF/HF transformer. This makes the proposed system a retrofit to existing 12-pulse rectifier systems.

$$I_{a\_in} = \left(\frac{4\sqrt{3}}{\pi}\right) \cdot I_{DC} \cdot \begin{bmatrix} \sin(\omega_s \cdot t) \\ -(1/11) \cdot \sin(11 \cdot \omega_s \cdot t) \\ +(1/13) \cdot \sin(13 \cdot \omega_s \cdot t) \\ -(1/23) \cdot \sin(23 \cdot \omega_s \cdot t) + \cdots \end{bmatrix} \quad (3.4)$$

3.2.3. Medium Frequency (MF) or High Frequency (HF) Transformer

As discussed earlier, based on the required power density and efficiency, the transformer can be designed with conventional silicon steel or amorphous cores to operate at a MF (400 Hz to 2 kHz) or at HF (5 kHz to 20 kHz). It may be noted that since the audible noise is typically high for the frequency range between 2 kHz and 5 kHz, it becomes physically challenging to design the transformer core in that range. For high power applications, MF is desired since the converter switching loss can increase significantly is operated at high frequencies. The construction is otherwise similar to the line frequency transformer in a typical 12-pulse rectifier. If three 1-phase transformers are used, they should have three windings on each transformer with the turns ratio – $N_{pri}:N_{sec}:N_{ter} = 1:1:\sqrt{3}$ as in the conventional system shown in Figure 3-1. The transformer also needs to handle the harmonic currents that flow through primary, secondary and tertiary windings. Detailed transformer design is covered in section 6.

3.2.4. Passive Components and Filter Design

The input LC filter is designed similar to the corresponding multi-pulse rectifier's typical filter design since the input currents will have similar harmonics (*fundamental, 11^{th}, 13^{th}*, etc.). The input filter can be designed at around 400 Hz cut-off

frequency. The design of the DC bus capacitor primarily depends on the requirement for the motor drive inverter, which is not focused in this section.

3.2.5. Simulation Results

The front-end of the proposed topology (as in Figure 3-3), including the AC-AC converter, MF/HF transformer and the rectifiers, was simulated using PSIM for a power rating of *100 H.P.* with a 3-phase utility voltage of *690* V_{LL}. Figure 3-8 and Figure 3-9 show the different simulation waveforms on the transformer primary side and their FFTs, respectively for the AC-AC converter and diode rectifier sections. These simulations were performed with only a *30 uF* capacitor at the utility side and no additional filter, to compare with a conventional 12-pulse rectifier system.

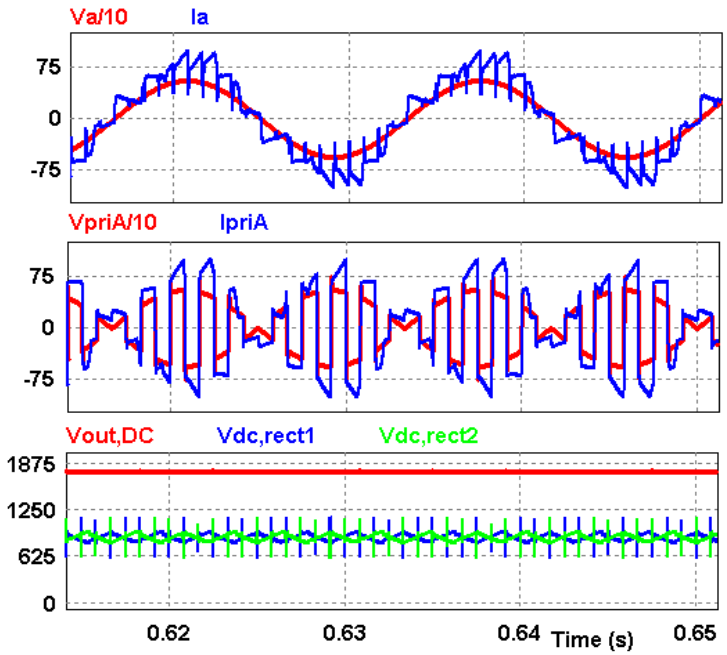

Figure 3-8: (i) Input current and voltage (*reduced scale)* (ii) transformer primary voltage and current; (iii) DC-link voltages

It can be seen that the quality of input current and the diode rectifier output voltage are similar as in a typical 12-pulse rectifier (harmonics are *11th, 13th*, etc.). It can also be seen that the individual DC bus voltages are phase-shifted to get 12-pulse rectifier operation. Yet the transformer operates at MF/HF (here 600 Hz), which reduces the size. There are some low-energy spikes in the input current, which is a result of the transformer leakage inductance. These spikes can be easily dealt with adding a filter. It can also be seen that there is a small amount of *3rd* harmonic current at the utility input caused by the interaction of the transformer primary current with the AC-AC converter switching frequency. Since the simulations were carried out using a 600 Hz transformer (to match experiment set-up), which is close to the *11th and 13th* harmonic frequency of utility input current; this creates a small amount of *3rd* harmonic that appears as a by-product. The overtones can be reduced if a 720 Hz or higher frequency is used.

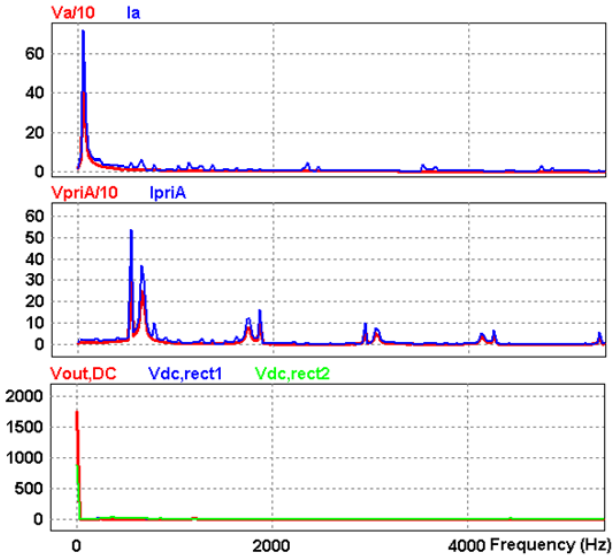

Figure 3-9: FFTs of waveforms in Figure 3-8

From Figure 3-10, the phase shift between the transformer secondary voltages and currents are evident. Transformer primary current is the result of sum of the secondary and tertiary currents. From the graph (iii) in Figure 3-10, it can be seen that the secondary and tertiary currents, when operated on by the AC-AC converter switching function, look similar to the ones in a conventional 12-pulse rectifier system. This enables the input utility current to have similar features as in the conventional system.

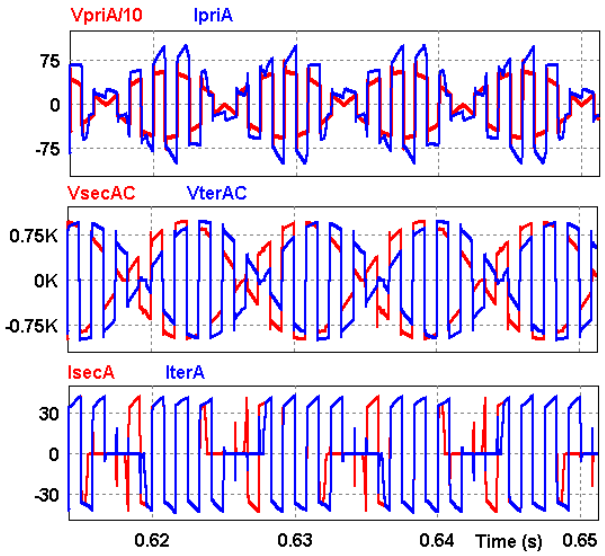

Figure 3-10: Simulation waveforms at the transformer - (i) Primary voltage (*reduced scale*) and current, (ii) Secondary and tertiary line-to-line voltages; (iii) Secondary and tertiary diode rectifier input currents

3.2.6. Experimental Results

Based on the simulation results and the transformer designs done earlier, experiments were conducted on a scaled down laboratory prototype of 1 kW 12-pulse rectifier configuration. Similar to the simulation results, experiments were conducted with and without input filter. Three 1-phase 600 Hz transformers were used for the experiments, whose secondary and tertiary windings were connected in star-delta

configuration as in Figure 3-3. Modulation scheme was implemented using TI Delfino *TMS320F28335* microcontroller.

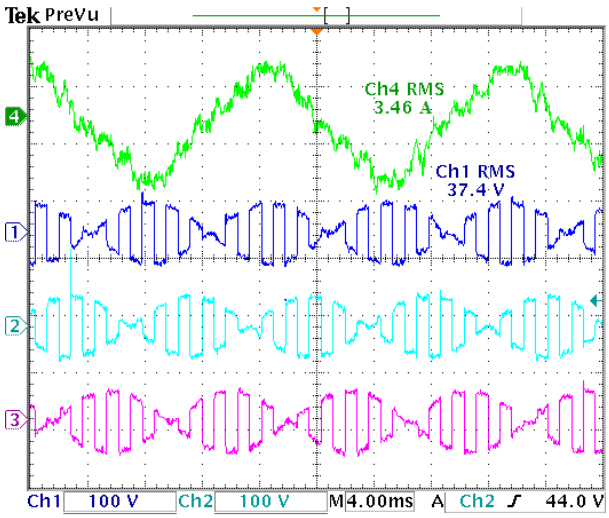

Figure 3-11: Ch. (1), (2), (3) show the three transformer primary voltages and Ch. (4) shows the unfiltered utility current

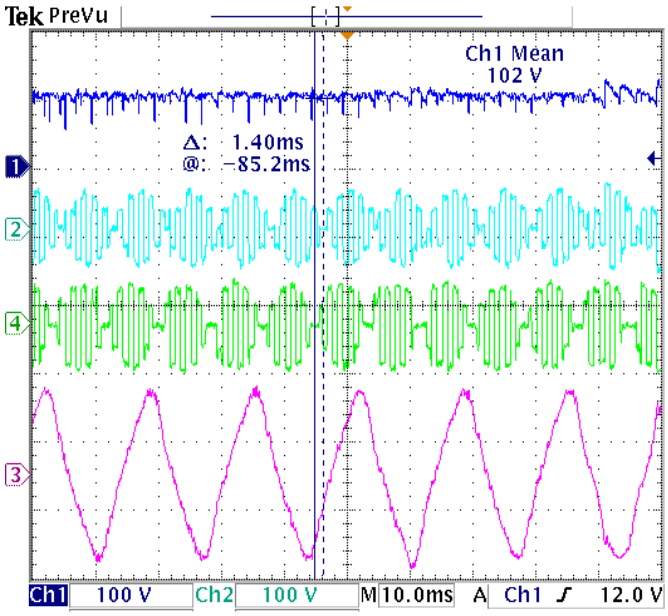

Figure 3-12: Experimental waveforms: DC bus voltage, transformer secondary/tertiary voltages and filtered utility input current (Ch. 3)

Figure 3-11 shows the experimental waveforms of the utility input current and the three transformer primary voltages with just a *30 uF* film capacitor as the input filter. Figure 3-12 shows the net output DC voltage ($V_{out,DC}$), transformer secondary and tertiary voltages of phase A (V_{secA} *and* V_{terA}) and the filtered (*500 Hz cut-off*) utility input current (I_a). Small spikes can be seen on the net DC bus voltage that is due to transformer leakage inductance and fast-switching diode transients. The 30^o phase-shift between the transformers' secondary and tertiary voltages are also evident (*1.4 ms*) from the waveform. Figure 3-13 shows the waveforms of the individual DC voltages (V_{outDC}, $V_{dcrect1}$ and $V_{dcrect2}$) along with the utility input current. As seen in the simulation results, there was a small 3^{rd} harmonic component in the utility current, which is due to the interaction of the different frequency tones.

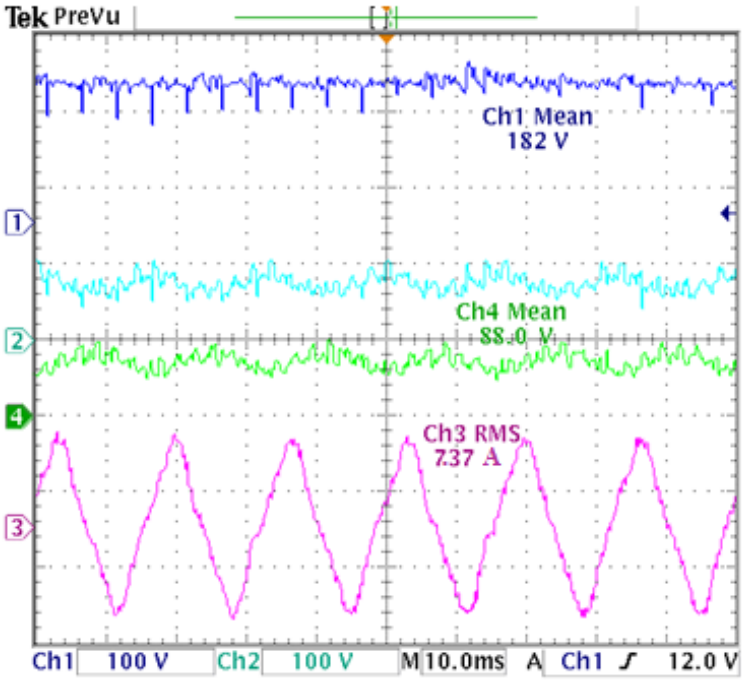

Figure 3-13: Experimental waveforms: individual DC bus voltages and utility input current (Ch. 3)

3.3. MF Transformer based ASD Topology with PWM Front-End

In this sub-section a medium frequency transformer with AC-AC converters at the input side is shown to obtain good input current performance with simultaneous reduction in size, weight and volume, especially for lower voltage 3-phase utility (*480 V_{LL}, 690 V_{LL}, etc.)*. The transformer primary side structure is similar to the one explained in the previous sub-section (see Figure 3-3). An AC-AC converter using bidirectional switches (see Figure 1-10) is more suitable than the unidirectional AC-AC converter if operated at high PWM frequencies. The AC-AC converter gating signals are generated by a product of unipolar line frequency sine PWM and a MF square function. The modulation strategy is flexible and allows for higher PWM switching frequency operation of the AC-AC converter, while ensuring that the transformer core is operated at MF over the entire range of operation. The secondary side of the transformer is delta-connected to a 6-pulse rectifier, with a simple or NPC motor drive inverter as discussed earlier. Here, the filter sizes are smaller due to the use of higher frequency PWM. The main features of the proposed system in Figure 3-14 are as follows:

- The input current harmonics are of higher order, at least twice the MF; therefore the input filter size is smaller.
- The secondary side diode rectifier output is of higher-quality as well.
- Since PWM operating frequency has to be at least 3 - 4 times that of the MF, the power converter losses are higher than the earlier case with square wave modulation.

- Though it is possible to use unidirectional AC-AC converter here, the diode rectifier may cause EMI issues if the PWM frequency current components are not filtered.

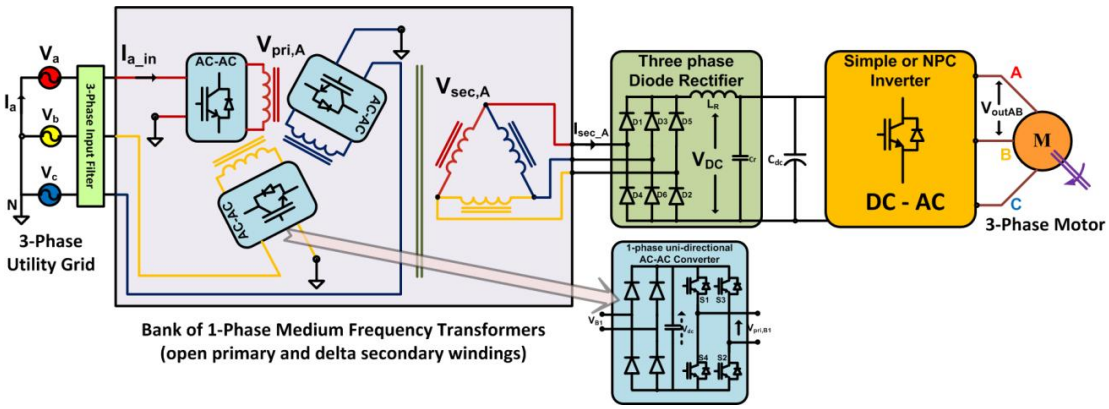

Figure 3-14: ASD topology with PWM modulation at the front-end instead of square wave. Note the unidirectional AC-AC converter (can be constructed using bidirectional AC-AC converter also)

Figure 3-14 shows the proposed ASD topologies with medium frequency (MF) isolation and PWM front-end. The operation and performance of this topology are explained through the following sub-sections: AC-AC converter, 3-phase diode rectifier, MF transformer, drive inverter, simulation and experimental results.

3.3.1. AC-AC Converter Operation

Each phase of the proposed AC-AC converter consists of 1-phase H-bridges with bidirectional switches; can also be constructed using back-to-back H-bridges or with unidirectional AC-AC converter as shown in Figure 3-14. The AC-AC converters can be visualized as 1-phase 1x1 matrix converters, modulated with a multiplication of a synchronized MF square wave function and a 3-phase utility unipolar sine PWM. If ω_s is the utility line frequency, ω_{sq} is the square wave MF and ω_c is the PWM carrier frequency ($\omega_c = m_f.\omega_s$); then the output of the AC-AC converters have mainly three

frequency components – ω_{sq} and ($\omega_{sq}\pm 2.\omega_s$), in addition to the higher frequency components at or above the PWM switching frequency. The PWM switching frequency should be selected to be approximately 3 to 5 times the MF. Equations (3.5), (3.6), (3.7), (3.8) and (3.9), derived assuming a diode front-end, show the phase-A utility input voltage (V_a), diode rectifier switching function (S_d), sine PWM switching function (S_{AB}), square wave switching function (S_{sq}) and transformer primary voltage ($V_{pri,A}$) respectively. Overall AC-AC switching function can be given by $S_{acac} = V_{pri,A}/V_a$.

$$V_a = \sqrt{2} \cdot V_{a,rms} \cdot \sin(\omega_s \cdot t) \tag{3.5}$$

$$S_d = \frac{4}{\pi} \cdot \sum_{n=1,3,5\ldots}^{\infty} \frac{1}{n} sin(n \cdot \omega_s \cdot t) \tag{3.6}$$

$$S_{AB} = \begin{bmatrix} 0.866 \cdot m_a \cdot \sin(\omega_s \cdot t) \\ +0.275\ \sin\big(\{m_f \pm 2\} \cdot \omega_s \cdot t\big) + 0.014\ \sin\big(\{m_f \pm 4\} \cdot \omega_s \cdot t\big) \\ +0.156\ \sin\big(\{2m_f \pm 1\} \cdot \omega_s \cdot t\big) + 0.028\ \sin\big(\{2m_f \pm 5\} \cdot \omega_s \cdot t\big) \\ +\ higher\ order\ terms \end{bmatrix} \tag{3.7}$$

$$S_{sq} = \frac{4}{\pi} \cdot \sum_{n=1,3,5\ldots}^{\infty} \frac{1}{n} cos\big(n \cdot \omega_{sq} \cdot t\big) \tag{3.8}$$

$$V_{pri,A} = m_a \cdot V_{a,rms} \cdot \begin{bmatrix} 0.76 \cdot \sin\big(\{\omega_{sq} \pm \omega_s\} \cdot t\big) \\ (+/-)\ 0.13 \cdot \sin\big(\{\omega_{sq} \pm 3\omega_s\} \cdot t\big) \\ +0.25 \cdot \sin\big(\{3 \cdot \omega_{sq} \pm \omega_s\} \cdot t\big) \\ +\ other\ terms \end{bmatrix} \tag{3.9}$$

The AC-AC converter waveforms of the proposed topology (see Figure 3-14) with 3- phase, 60 Hz utility input are shown in Figure 3-15. Figure 3-15 (a) shows the utility line to neutral (phase A) voltage, V_a. Figure 3-15 (b) is the unipolar PWM switching function (S_{AB}) obtained by intersecting a line frequency sinusoidal modulating waveform (ω_s) with a triangular carrier frequency [48]. Further, the shape of the input current (I_{a_in}) in Figure 3-14 is identical to S_{AB} and is of high quality at near-unity input

power factor. It can also be seen from Figure 3-15 (d) that the transformer secondary voltage has the envelope of sine PWM as well as that of the MF square wave.

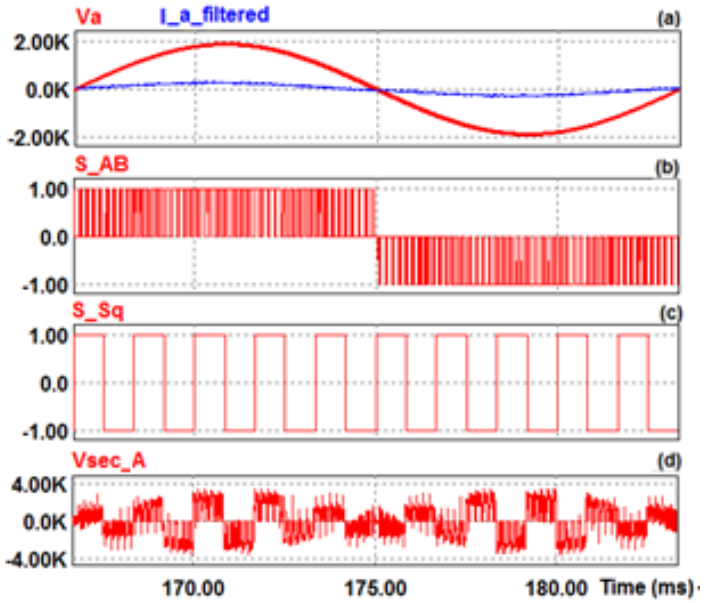

Figure 3-15: AC-AC converter waveforms from Figure 3 topology. (a) Input grid voltage and current, (b) Unipolar Sine PWM switching function, (c) Square wave switching function and (d) Transformer secondary voltage

3.3.2. Three-Phase Diode Rectifier

Since the 3-phase diode rectifier is connected across a delta winding, the operation of the rectifiers is governed directly by the primary side phase voltages. In this case, the transformer primary voltage is a product of MF square wave and unipolar sine PWM, which makes the diode rectifier operate like a PWM rectifier. This PWM property enables this topology to eventually make the utility input current of high quality. But it should be noted that since the diodes operate at the PWM frequency, fast-switching SiC or fast-recovery diodes must be used to reduce the switching losses.

If I_{DC} is the DC-link current, which is the output of the 3-phase rectifier, and assuming that the ripple on I_{DC} is negligible, then the diode rectifier behaves like a PWM rectifier, as discussed above; but the MF square wave modulation super-imposes the PWM rectifier switching function (3.7) with a MF square-wave function (3.8). So, the transformer primary (or secondary) current can be given by (3.10), assuming unity MF transformer turns-ratio. Now, the unfiltered utility input phase-A current, I_{a_in}, can be derived by operating the AC-AC converter switching function, S_{acac}, over the transformer primary current, $I_{pri,A}$ (other phase currents can be derived in a similar way). The input current equation (unfiltered) can be given by (3.11). The 3-phase rectifier DC voltage (unfiltered) can be derived using (3.12). From (3.11), it is clear that the utility input current has the fundamental, followed by harmonics close to PWM switching frequency, so it is of better quality, compared to the proposed topology in Figure 3-3. But this scheme also has a small 3rd harmonic frequency components (around 8 %) generated as a by-product of the switching functions and can be filtered by an L-C filter.

$$I_{pri,A} = \frac{I_{DC}}{m_a} \cdot \begin{bmatrix} 0.55 \cdot \sin(\{\omega_{sq} \pm \omega_s\} \cdot t) \\ +0.18 \cdot \sin(\{3 \cdot \omega_{sq} \pm \omega_s\} \cdot t) \\ +0.11 \cdot \sin(\{5 \cdot \omega_{sq} \pm \omega_s\} \cdot t) \\ + other\ terms \end{bmatrix} \tag{3.10}$$

$$I_{a\_in}\sim = \frac{I_{DC}}{m_a} \cdot \begin{bmatrix} 0.93 \cdot \sin(\{\omega_s\} \cdot t) \\ (+/-)\ 0.23 \cdot \ \sin(\{m_f \pm 2\} \cdot \omega_s \cdot t) \\ (+/-)\ 0.08 \cdot \sin(\{3 \cdot \omega_s\} \cdot t) \\ + other\ terms \end{bmatrix} \tag{3.11}$$

$$\overline{V_{DC}} = \frac{9 \cdot m_a}{\sqrt{2} \cdot \pi} \cdot V_{a,rms} \tag{3.12}$$

3.3.3. Medium Frequency Transformer

The MF transformer design is similar to the ones explained earlier. Based on the diode rectifier and the inverter equations, the minimum transformer turns ratio (secondary to primary) was calculated as per (3.13). This is considering that the DC-link voltage reduces to almost 86% of the level that is usually associated with a 3-phase diode rectifier ($1.35.V_{LL}$) and that the inverter operates with sine PWM.

$$N = \left(\frac{4 \cdot \pi}{9}\right) \cdot \left(\frac{1}{m_a \cdot m_{inv}}\right) \cdot \left(\frac{V_{inv\_a,rms}}{V_{a,rms}}\right) \tag{3.13}$$

where m_a and m_{inv} are the modulation indices of AC-AC converter and inverter, respectively. $V_{a,rms}$ and $V_{inv\_a,rms}$ are the grid and motor phase voltages, respectively. For unity modulation indices (peak), the turns-ratio was selected to be 1.0 in the simulations.

3.3.4. ASD with Motor Drive Inverter

Apart from the above explained circuits, the design of the proposed topology mainly consists of a simple or NPC inverter. The inverter is designed to supply variable voltage to the motor [45]. Conventional unipolar sinusoidal PWM or space vector PWM technique can be employed along with V/F control for the speed control of the motor. While a 2-level inverter is simpler in construction and modulation, NPC inverter topology presents certain other benefits to the system. First, voltage stress across the switches is divided into half. Furthermore, output current ripple and switching/conduction losses are mitigated. From a motor drive perspective, the use of a PWM-controlled NPC inverter improves dynamic performance, lowers stresses on the motor bearings/windings, and reduces noise influence on nearby devices. Variable

Voltage Variable Frequency (VVVF) is used to control the inverter. In constant torque applications, magnitude and direction of the motor flux can be locked together in direct proportion to the ratio of the inverter's output voltage to its fundamental frequency.

3.3.5. Simulation Results

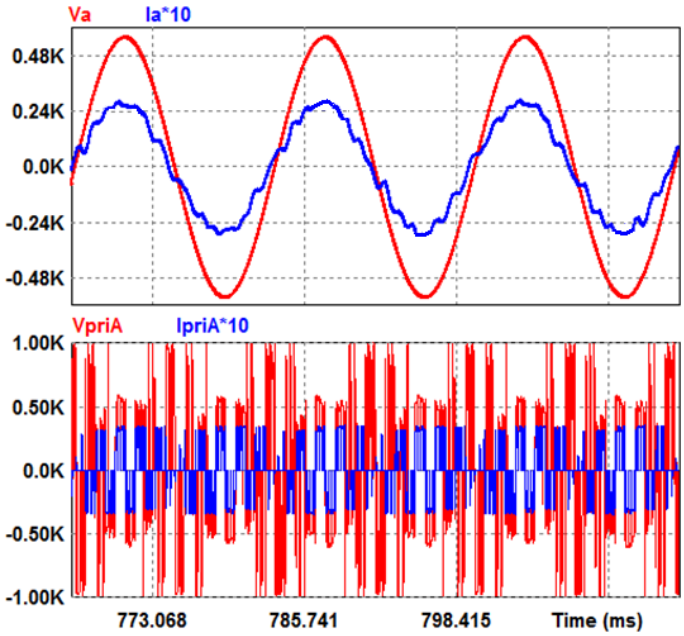

Figure 3-16: (i) Utility voltage (V_a), current (*scaled*), (ii) Transformer primary voltage ($V_{pri,A}$) and current

The proposed topology in Figure 3-14 was simulated using PSIM for a *690* V_{LL}, 60 Hz, 3-phase utility for a *30 H.P.* motor drive front-end system. Figure 3-16 shows the input current, I_a along with input voltage, V_a and transformer primary current, $I_{pri,A}$ along with the transformer primary voltage, $V_{pri,A}$. It can be seen that the input displacement power factor is close to unity and the input current is of good quality, when a 700 Hz cut-off input filter was employed. There are small 600 Hz resonances caused due to the interaction of the filter with the MF (here, 600 Hz) harmonics in the current. Figure 3-17

shows the simulation waveforms on the transformer secondary side. It can be seen that the transformer voltages are of sine PWM shape and the DC-link voltage is maintained fairly constant that can be supplied to the inverter.

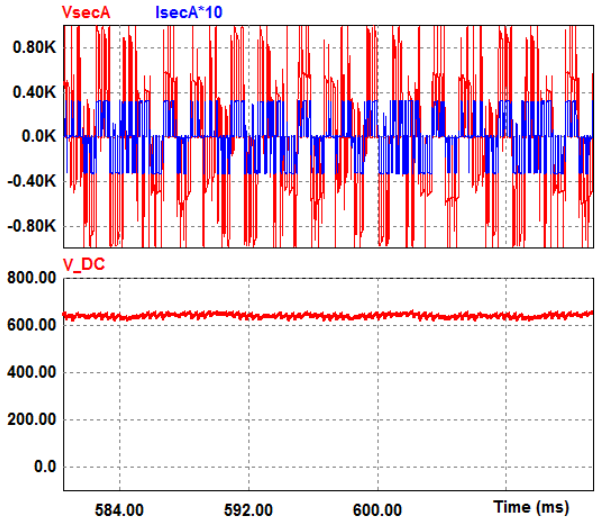

Figure 3-17: (i) Transformer secondary voltage ($V_{sec,A}$) and current (*scaled*); (ii) DC bus voltage, (V_{DC})

3.3.6. Experimental Results

Laboratory experiments were performed on a 3-phase scaled-down prototype of the front-end of the system similar to Figure 3-14 (with diode front-end), with the set-up similar as explained in the previous sub-section (0). Figure 3-18 shows the transformer phase-A and phase-B voltages along with the utility current and DC output voltage. It can be seen that the input current is of good quality, but has similar distortions as seen in the simulation results (see Figure 3-16) caused due to the interaction of filter resonance with the MF harmonics. It can also be seen that though no DC electrolytic capacitor was used, the DC-link voltage is also of good quality with an inductive load (almost 5 % inductance for line frequency).

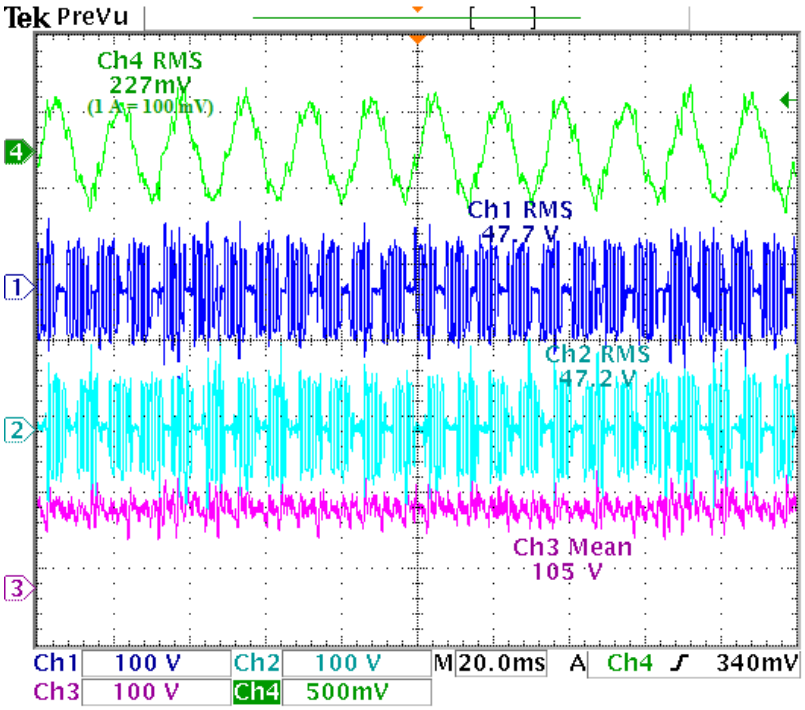

Figure 3-18: Experimental results for the topology in Figure 3-14: (Ch1) Transformer phase-A voltage, (Ch2) Transformer phase-B voltage, (Ch3) DC voltage with inductive load

3.4. **Conclusion**

In this section, a new MF/HF transformer based front-end topology for multi-pulse rectifiers was proposed, taking a 12-pulse rectifier based ASD application as an example. The topology consisted of AC-AC converters, MF/HF transformers and 3-phase diode bridges to replicate the behavior of a conventional 12-pulse or higher pulse rectifier. This approach could be a retrofit replacement to bulky line frequency transformers, providing higher power density in multi-pulse rectifier applications. Though the introduction of AC-AC converters provided many advantages to the system, it comes with certain implications on efficiency.

Another ASD topology/modulation scheme with medium frequency (MF) transformer isolation was also introduced. The modifications compared to the 12-pulse rectifier have only the delta windings on the secondary side. The performance of the overall system has been shown to be good: a) input current is of higher quality, with near unity PF, b) the DC-link capacitor size is reduced due to better quality rectified voltage, c) The proposed modulation strategy has been shown to be flexible to allow higher switching frequency operation of the AC-AC converter while the transformer core is operated at MF. Several other advantages of the proposed topologies have been discussed in detail. Experimental results on the medium frequency transformer have been shown to achieve efficiencies above 97.5 % and can be a good choice for ASD applications. Further, the overall size and weight of the transformer could be reduced by more than 50 % with a reduction of more than 60 % on the transformer. Further reduction in weight/size is possible through the use of better MF transformer core materials.

4. A NEW WIND TURBINE – MEDIUM VOLTAGE DC (MVDC) INTERCONNECTION

4.1. Introduction to Wind Turbine Generators (WTGs)

The world is entering a new era in energy generation, where the renewable energy sources such as solar, wind, etc. have started to achieve grid parity in price with the conventional sources of energy such as coal, oil, natural gas, etc. Driven by government subsidies and improved technologies, the cost of generation for renewable energy sources have been constantly falling and may extensively become cheaper than conventional generation within 2020, even if the government subsidies subside [56, 57]. These studies have further made renewable energy sources, such as wind even more attractive because of the opportunity to install them on a much wider scale, both economically as well as technologically.

Wind turbine generators (WTGs) have been traditionally installed as large farms on the land at locations where winds are steady and sufficiently strong. The WTGs are usually induction generators (in direct or doubly-fed configurations). As the size of the WTGs have been growing over the years, increasing their energy harvesting, direct-drive WTGs are also becoming very popular [58]. The most popular direct power converter architecture for interfacing WTGs to the utility grid is shown in Figure 4-1. It consists of a PWM rectifier that converts the variable WTG frequency voltage to a regulated DC-bus. The PWM inverter converts the DC to line frequency AC voltage, which is then interfaced with the utility through a large line frequency transformer.

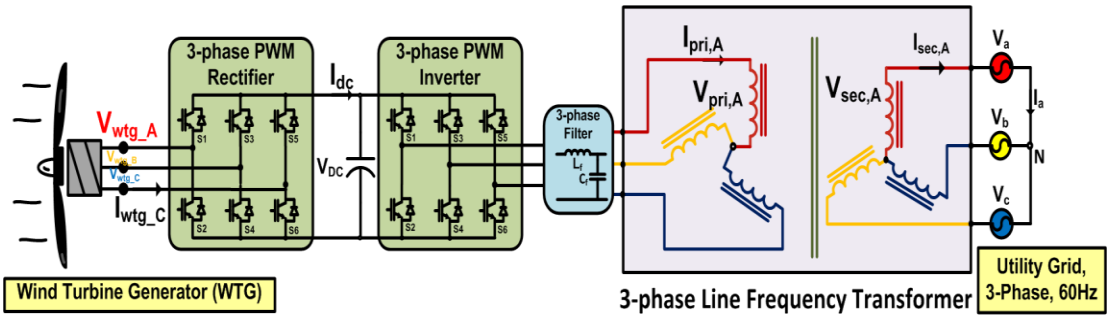

Figure 4-1: Conventional WTG – utility grid interface using a line frequency transformer

4.2. Introduction to Offshore Wind Farms

In order to further increase the energy harvesting and install even larger capacity from WTGs, off-shore wind farms are being extensively used and studied at present [59]. As the state of the art offshore wind farms are sited beyond 50 km or so from shore, there is interest in further advancing technology by using high voltage direct current (HVDC) for transmission of the collected energy to shore. However, a local collection grid is necessary to first condition the energy from each WTG and aggregate the energy in preparation for transmission via HVDC (see Figure 4-2). It is anticipated that use of an MVDC collection grid may have significant advantages over a traditional medium voltage AC (MVAC) collection grid when interfacing with an HVDC converter station for transmission to shore. Furthermore, as individual WTG size as well as overall wind farm size both increase, there will be a corresponding increase in the cable lengths within the wind farm collection grid. Use of an MVDC collection grid may have a further advantage in this case due to the elimination of AC reactive power requirements within the collection grid. With many state of the art WTGs now offering close to 100% of power processed through power electronics, the possibility of

connecting directly to an MVDC grid without the use of a line frequency transformer also yields advantages.

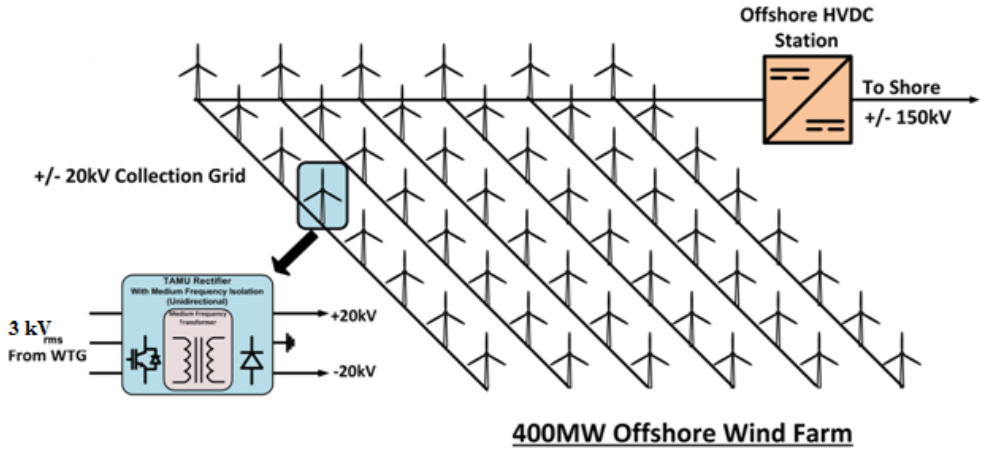

Figure 4-2: An example 400 MW offshore wind turbine generator architecture with MVDC-HVDC interconnection

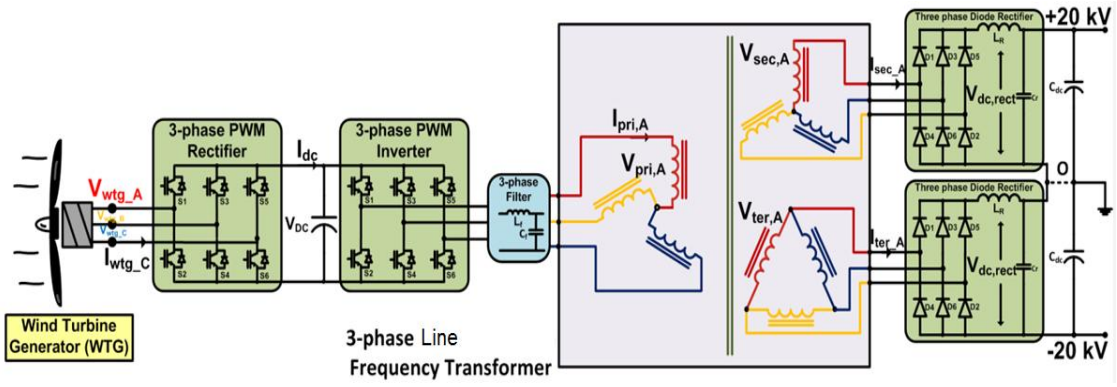

Figure 4-3: WTG Utility Interface with a line frequency transformer in 12-pulse configuration

4.3. State of the Art

This sub-section considers the current state of the art in power conversion technology for collection of energy from offshore wind turbines. The traditional method for interfacing a WTG to a collection grid with a full-power-rated converter relies on the

use of front-end back-to-back PWM rectifiers as in Figure 4-1, followed by line frequency transformer and diode rectifier systems in 12-pulse rectifier configuration. However, this arrangement can be replaced with a single matrix converter, as done in [60]. Not only has the traditional back-to-back converter arrangement in Figure 4-3 been consolidated into a single converter, but a medium frequency transformer has been added to the topology, which is facilitated by the ability of the matrix converter to directly convert the output frequency of the WTG to a fixed medium frequency. The inventors acknowledge the ability of medium frequency isolation to reduce the overall mass and volume of the conversion solution. Following the medium frequency isolation stage, several possible implementations of the AC to DC rectifier stage have been described, including a multistage solution as well as a simple passive rectifier.

Although originally intended as a method for interfacing a stiff AC power system to an HVDC link, the method proposed in [61] could likely be applied to an offshore wind farm collection grid. In such a case, the multilevel topology featured would be connected to the 3- phase outputs of the WTG and used to synthesize a suitable MVDC output voltage. The obvious disadvantage in this case is the requirement of a front-end transformer operating at the WTG electrical frequency, which can be anywhere from 10 Hz to 60 Hz. However, an advantage of such a topology is the ability to increase reliability via multiple levels. Similar to the configuration proposed in [61], the more fully developed modular multilevel converter (MMC) could be suited for use in connecting individual WTGs to an MVDC collection grid. The lack of a front-end WTG frequency transformer is an advantage of this approach; however a series inductance is

still required, although the generator impedance may be sufficient in the case of a Permanent Magnet Synchronous Generator (PMSG). The lack of isolation between the WTG and MVDC grid with this approach is a clear disadvantage, especially in a large wind farm. Also, capacitor charge balancing becomes difficult for many levels.

The approach proposed in [62] provides a simple and effective way to interface the WTG to an MVDC grid, although there are a few unique disadvantages as well. The use of MF isolation is desirable and significantly reduces system mass and volume; however, this approach assumes the WTG to have an operating frequency of 1.2 kHz, requiring a large number of poles which results in a larger diameter machine. The secondary side of the MF transformer is tied to the MVDC grid via a passive diode rectifier, which is simple and reliable, but is unidirectional and requires a secondary power converter to supply reactive power to the WTG. It may introduce significant harmonics. Furthermore, there is no obvious strategy for controlling the MVDC collection grid voltage. Some other topologies have also been published in the literature, which can be adapted to a WTG-MVDC interconnection [11, 13]

This section investigates a new approach to the conversion and collection of energy from offshore wind turbine generators (WTGs) and the interconnection between individual WTGs and a medium voltage DC (MVDC) collection grid. Several candidate converter topologies and MVDC collection grid architectures were investigated throughout this work, including series/parallel connection of WTGs, as well as various MVDC collection grid voltages. Following the investigation of various MVDC collection grid architectures, a voltage of +/- 20 kV was arrived at for the MVDC. The

proposed approach includes passive rectification on the front-end, MF isolation, and multilevel boost power factor correction (PFC) converter at the DC output. Operating principles and unique advantages of the proposed approach are explained further.

The offshore WTG system architecture has been assumed to be as in Figure 4-2. It is assumed that the WTGs are located more than 50 miles from the shore and need to be connected via HVDC interlink. It is desired that the voltage conversion is in two main stages – (i) WTG 3-phase AC to MVDC at the tower itself and (ii) MVDC to HVDC to shore. The focus of this research is mainly on stage (i).

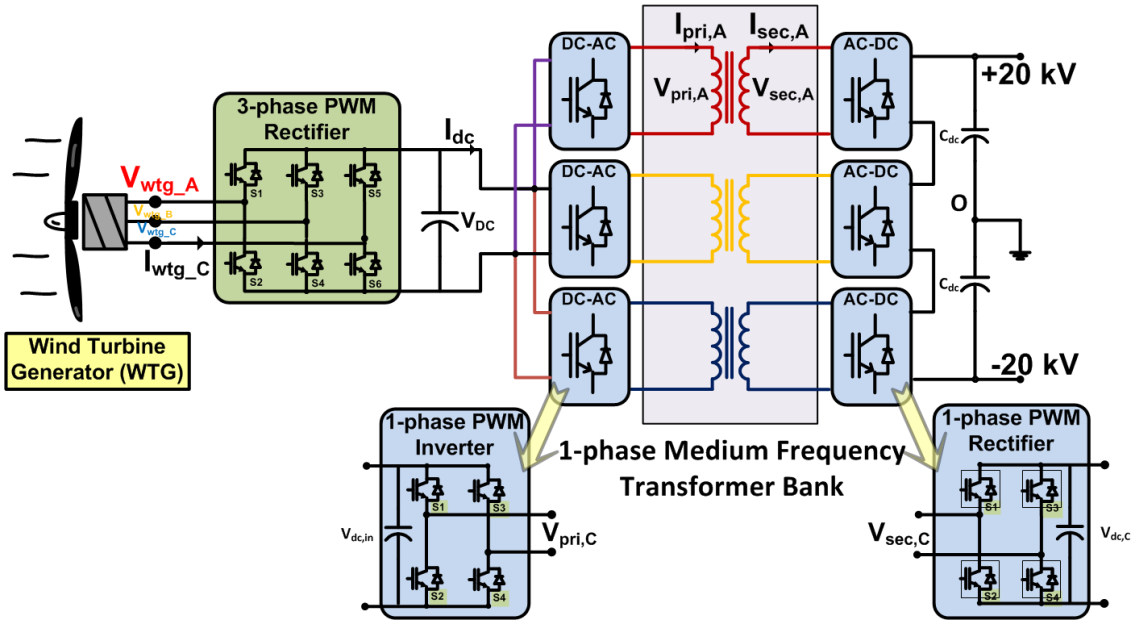

Figure 4-4: Isolated Medium Frequency WTG-MVDC interconnection via DC-DC converter

An isolated MF transformer based topology is shown in Figure 4-4 that employs interleaved multi-phase DC-DC converters to generate the required MVDC voltage from the WTG DC-bus. The PWM inverters and rectifiers can be operated in MF square wave

mode, with the primary inverters connected in parallel across the WTG DC bus and the secondary side rectifiers connected in series across the MVDC bus. This topology is simple in construction and MF operation helps reducing the switching losses in the power converters. A drawback of this topology is that it is not suitable for MV WTGs. Moreover the electrolytic capacitors on the WTG side can affect the system reliability.

4.4. A New WTG-MVDC Interconnection using 3-level Boost PFC

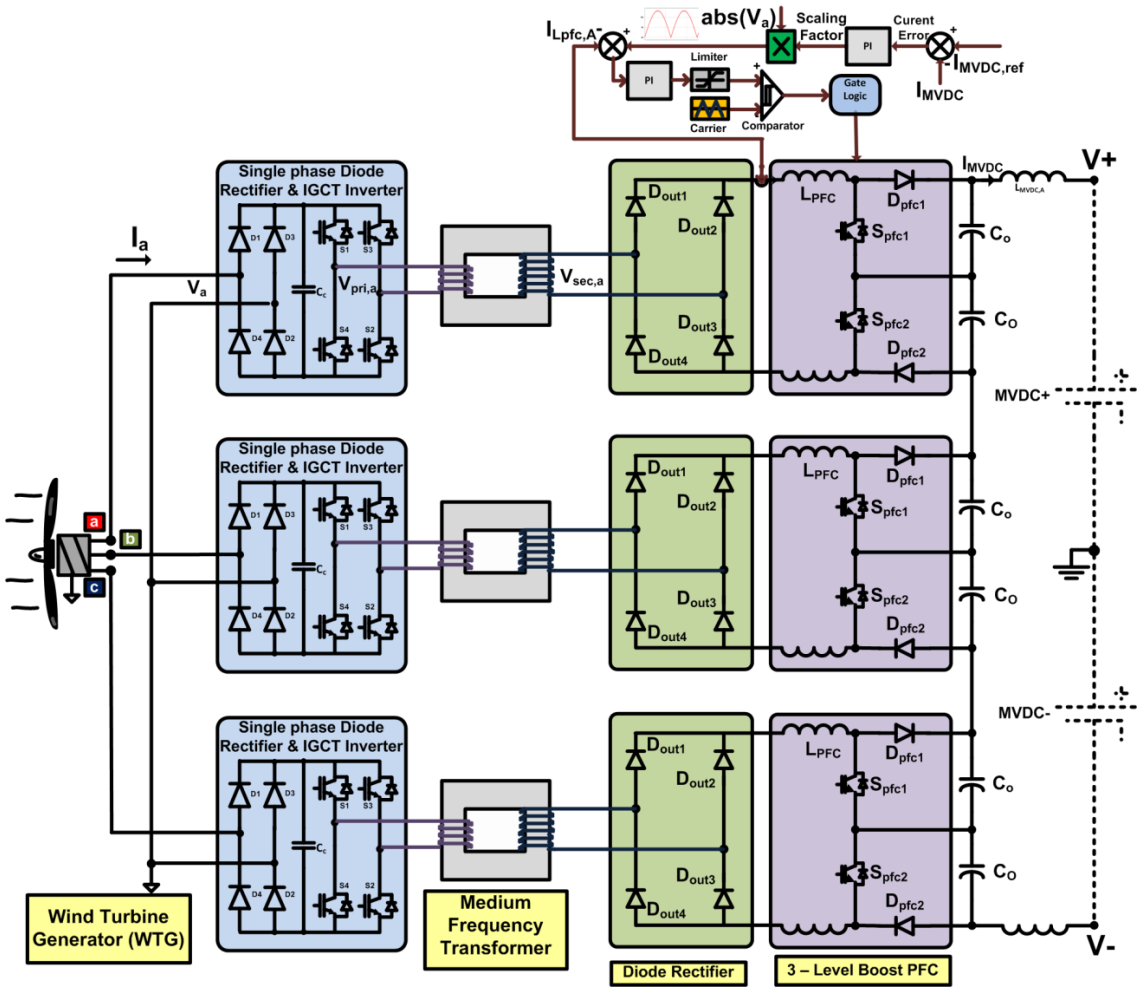

Figure 4-5: Proposed WTG-MVDC interconnection using MF transformer and 3-level boost PFC

The proposed topology is illustrated in Figure 4-5. This topology is derived from the concept proposed in Figure 2-4 under section 2.2. The major differences are that 3-level boost PFCs are used here instead of simple PFCs and the output DC voltages are connected in series instead of parallel. Moreover the presence of large input inductances in synchronous WTGs causes EMI challenges, especially with diode front-end. The design can be broadly divided into the following main sub-sections: AC-AC converter, 1-phase boost PFCs, control strategy, filter design and MF transformer.

4.4.1. AC-AC Converter

There are three 1-phase AC-AC converters in the proposed approach, similar to the ones described in earlier sections. Here too, the converters can be constructed using AC-AC H-bridge using bidirectional switches. Each AC-AC converter consists of a 1-phase diode bridge and a 1-phase inverter H-bridge (with IGCTs) connected by de-coupling capacitors. In order to interface to a $3.0\ kV_{LL(max)}$, f_s = 60 $Hz_{(max)}$ 3-phase wind turbine generator (WTG), 5.5 kV rated diodes and IGCTs will be sufficient or series stacked lower voltage devices can be used. The AC-AC converter switching functions are given by (2.1), (2.2) and (2.3) from section 2.2.1. Even if the frequency of WTG AC varies, the transformer operating frequency does not change much. This property can make the proposed topology attractive for wind turbine and adjustable speed drive applications where the operating frequency varies.

4.4.2. Single Phase 3-level Boost PFCs

The transformer secondary voltage is a ‘flipped sine wave’ (product of line frequency sine and MF square wave, slightly smoothened due to the filtering action of

the transformer leakage inductance. The diode rectifier of the boost PFC stage converts this flipped sine wave into full-wave rectified (twice-the-WTG-frequency) waveform. It should be noted that even though the transformer frequency is HF or MF, the diode rectifier switches at that frequency and the rectified voltage on the transformer secondary looks similar to the rectified voltage waveform of the weak DC-link on the primary (WTG) side. After this, the remaining boost converter in the PFC operates like a conventional 3-level PFC, making the inductor current in phase/shape as the rectified voltage [13, 14, 63, 64]. Thus, the design of this topology is straight forward. Since the transformer leakage inductance filters the high frequency components in the voltage, a small capacitor has to be plugged-in across the secondary to suppress transient voltages.

If 'β' is the minimum boost PFC gain (~ 1.5 to 2.0). If V_{dc} is the required DC output voltage, the required transformer turns-ration, N can be calculated as per (4.1):

$$N = \frac{n_2}{n_1} = \left(\frac{\pi}{2\sqrt{2}\cdot\beta}\right) \cdot \left(\frac{V_{DC}}{V_{a(rms)}}\right) \tag{4.1}$$

For a 3 kV_{LL} WTG input, MVDC voltage of 14 kV_{dc} per phase (~2*20/3 kV) and for a β value of 1.5, the transformer turns ratio is approximately $n_2{:}n_1$ = 6:1. Higher turns-ration in a MF transformer or HF transformer can cause significant *corona* losses that affect size advantage. Boost PFC [64] switches have to be rated (after 50% derating) at nearly 30 kV, that amounts to nearly six IGCTs in series. While the current rating of the primary side converters is nearly 2000 $A_{(pk)}$, the secondary side converters have to be rated (with 30% derating) at nearly 400 $A_{(pk)}$.

4.4.3. Control Strategy

The control objective for the boost PFC stage is to emulate an active resistor that makes the transformer currents' shape and phase follow the primary voltages, say $V_{pri,A}$. Figure 4-6 depicts the control strategy employed in the proposed approach (shown only for phase-A, but the control is similar for other phases too). Depending upon the WTG available power, the magnitude of the PFC inductor current, $I_{Lpfc,A,}$ is varied by adjusting the scaling factor that is generated from the output MVDC current (I_{MVDC}) regulation; keeping the shape same as that of the rectified voltage, $V_{rect,A}$. It may be noted that since $V_{rect,A}$ has the same shape as the rectified voltage of a conventional boost PFC system, the design and control are very similar to a conventional 3-level boost PFC. It is important to note that the boost PFC current control is not much affected by the MF since the rectified voltage on the secondary side has twice-the-WTG-frequency envelope (with small MF resonances). The inner current control loop must be faster than the outer voltage loop. For tuning the control parameters, conventional methods like Ziegler Nichols can be used. When the DC outputs of the boost PFC stages corresponding to the three phases are connected in series, the second harmonic power gets compensated and hence the DC capacitor need not be very large to maintain the MVDC. This is a notable advantage of the proposed modulation scheme. Another advantage is in terms of reduction in size, which is explained in later sections.

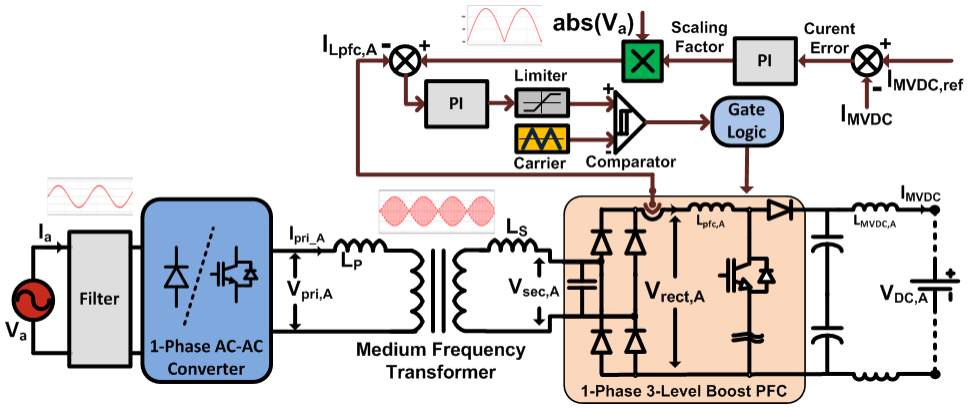

Figure 4-6: Control strategy for the proposed approach in Figure 4-5 (shown only phase-A)

4.4.4. Medium Frequency (MF) Transformer

The MF transformer design is evaluated in detail under section 6.

4.4.5. Filter Design

Due to the large WTG inductance, MF resonances are generated in the system that have to be suppressed using a filter at the WTG terminals. The single phase equivalent diagram of the filter is shown in Figure 4-7. Since the oscillations are not very large, a filter can be designed with a cut-off at $2*f_{sq}$ as shown in (4.2). Table 4-1 shows the selected values of the filtering components for this design.

$$f_{cut-off} = 2 * f_{MF} = \frac{1}{2 \cdot \pi \cdot \sqrt{Lwtg \cdot Cfwtg}} \tag{4.2}$$

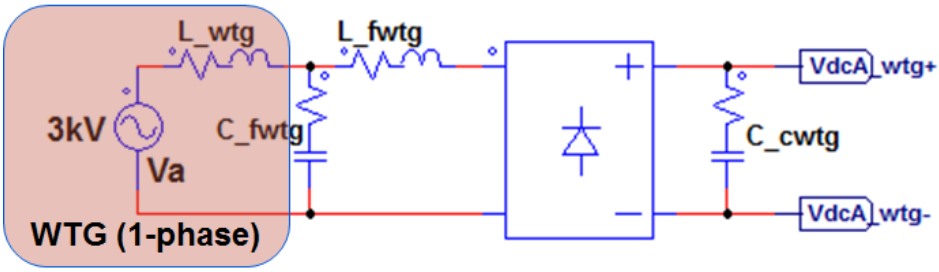

Figure 4-7: Equivalent diagram at the WTG for the filter design

Table 4-1: Filter design parameters and values

Parameters	Values
Generator Voltage (V_a)	3 $kV_{rms(LL)}$ to 1.5 $kV_{rms(LL)}$
Generator Frequency	60 Hz to 30 Hz
Inverter Frequency (f_{MF})	600 Hz
Generator Impedance (L_{wtg})	4 mH (1.0 p.u. per phase), 10mOhms
Input filter Capacitor (C_{fwtg})	10 uF
Input filter Inductor (L_{fwtg})	10.0 uH
WTG DC Bus Capacitor (C_{cwtg})	1.0 uF

4.5. Maximum Power Point Tracking (MPPT)

The direct-drive PMSG based WTGs typically follow the curves mentioned in Figure 4-8 [65]. At low wind speeds, the turbine is operated at maximum aerodynamic efficiency up to the rated rotor speed of around 14 RPM (for an 8 MVA machine); at high wind speeds, the pitch control keeps the rotor speed at 14 rpm. For any wind velocity, there is a particular WTG speed at which the power generated is maximized. The equations mentioned in [66] can be modeled in a block with wind velocity as input and used to generate the reference speed and voltage at a particular wind speed. There are three main MPPT methods used (shown in [66]). In this topology, the power signal feedback (PSF) algorithm can be used along with the Hill-Climb Search (HCS) algorithm in such a way that the fast convergence of the former and precision of the latter can be clubbed. Salient features of both the algorithms are explained through [66].

PSF algorithm requires the knowledge of the WTG's MPP curve and tracks this curve through its control mechanisms. The maximum power curves need to be obtained via simulations or off-line experiment on individual wind turbines. Reference power is

generated either using a recorded MPP curve or using the mechanical power equation of the WTG where wind speed or the rotor speed is used as the input. Once this is known, the MPP can be estimated using the power curve and the reference $I_{MVDC,ref}$ can be derived accordingly. While the HCS control algorithm continuously searches for the MPP of the WTG. Depending upon the location of the operating point and relation between the changes in power and speed, HCS algorithm computes the desired optimum signal (frequency and magnitude) in order to drive the system to the MPP.

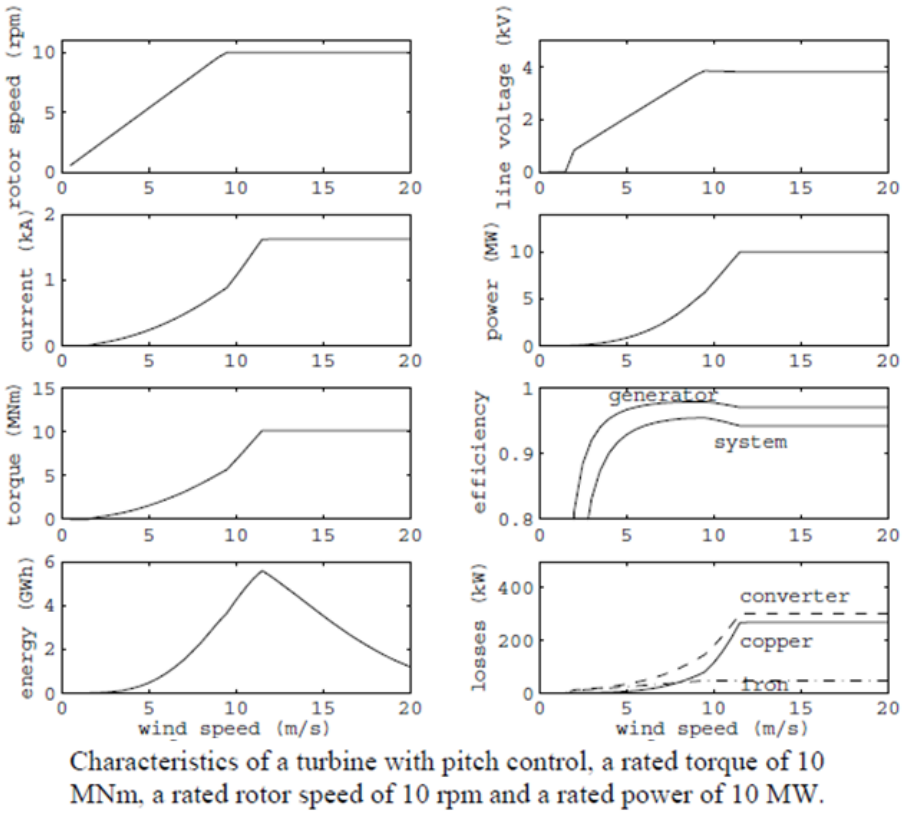

Figure 4-8: Characteristics of pitch control in a 10 MVA WTG (© 2007 IEEE [65] - Adapted with permission from the IEEE)

4.6. Simulation

The specifications of each WTG have been assumed to be as in Table 4-2. The WTG is assumed to be a permanent magnet synchronous generator (PMSG) with direct-drive. Though, the methods discussed in this report may be difficult to be employed for a doubly-fed induction generator since a WTG frequency transformer is desired to interface with the utility. Figure 4-8 shows a typical power-to-speed plot of a PMSG at different wind. Even other different characteristics of a 10 MVA WTG under active pitch control have been shown in Figure 4-8. It can be seen that the cut-in speed is approximately one fourth of the rated speed. These aspects were simulated on the proposed topology in Figure 4-5 and the results are shown in this sub-section.

Table 4-2: System parameters used in simulation of proposed approach

Parameters	**Values**
Generator Voltage	3 $kV_{rms(LL)}$ to 0.75 $kV_{rms(LL)}$
Generator Impedance	4 mH (1.0 p.u. per phase), 10mOhms
Generator Frequency	60 Hz to 15 Hz
Inverter Frequency	600 Hz
XFMR Frequency	600 Hz
XFMR Turns Ratio	1 : 6
Boost PFC Frequency	720 Hz (**Selected to reduce resonances*)
Boost PFC Inductance	20 mH (~ 0.1 p.u. of MVDC w.r.to 60 Hz)
Boost PFC Capacitor	Two 2 mF capacitors in series per phase
Input filter Capacitor	5 uF
Input Power	8 MVA maximum
Output Voltage	+/- 20 kV
Number of IGCTs (5.5kV)	12 (primary) + 18 (secondary)
Number of Diodes (5.5kV)	12 (primary) + 54 (secondary)

The Table 4-2 shows the design parameters and simulation set-up information for the simulations. The MVDC voltage is restricted based on the maximum turns-ratio that can be possible in the given MF transformer. Here it is assumed that *1:6* is the maximum and for the specified WTG voltage, +/- 20 kV MVDC voltage is the optimum. PSIM simulation model was developed as in Figure 4-5. Figure 4-9 and Figure 4-10 show the simulation waveforms of the system at 100% power (wind speed of 15 m/s) and 25% power (wind speed of 7 m/s), respectively. The MVDC was assumed to be a constant DC, fixed by the HVDC link-converter. The control strategy was employed as in Figure 4-6. It can be seen from Figure 4-9 and Figure 4-10 that the MVDC current is regulated around the set point through the MVDC inductor.

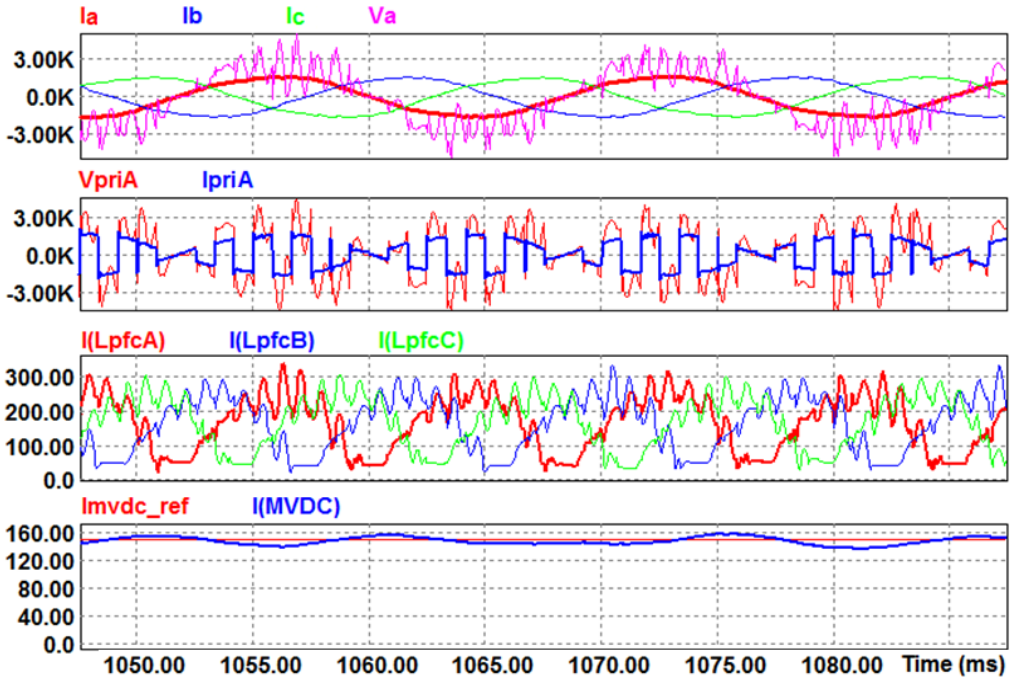

Figure 4-9: PSIM Simulation waveforms at 100% WTG power and 15 m/s wind speed

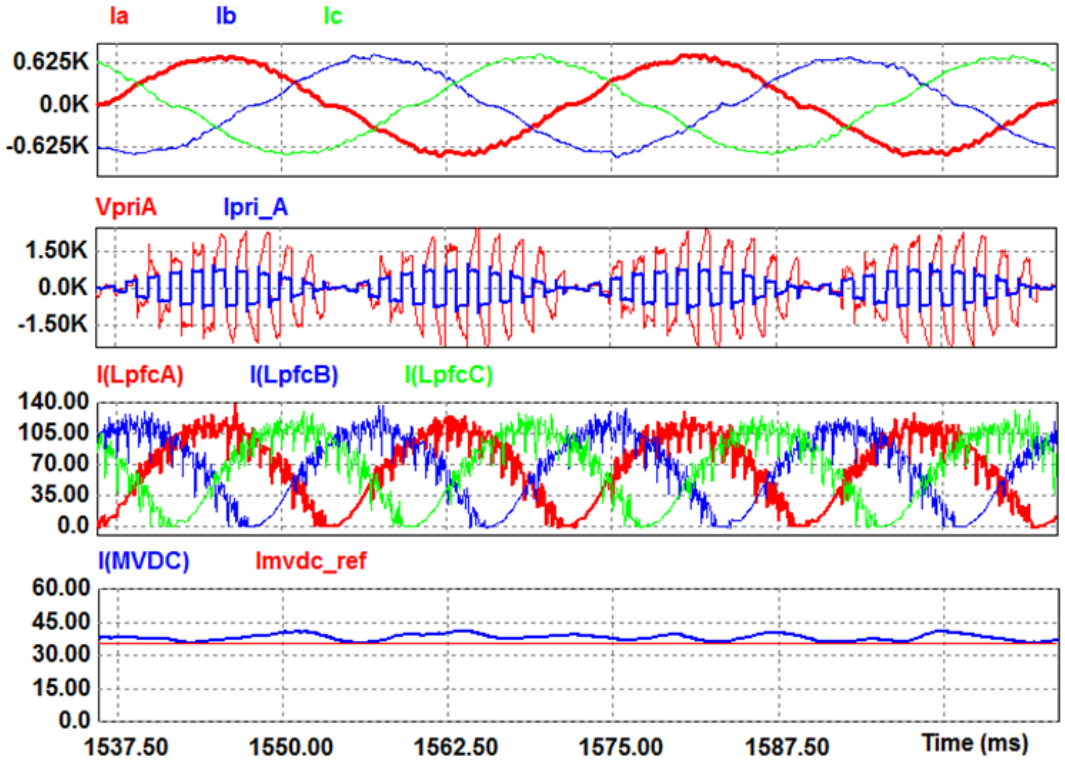

Figure 4-10: PSIM Simulation waveforms at 25% WTG power and 7 m/s wind speed

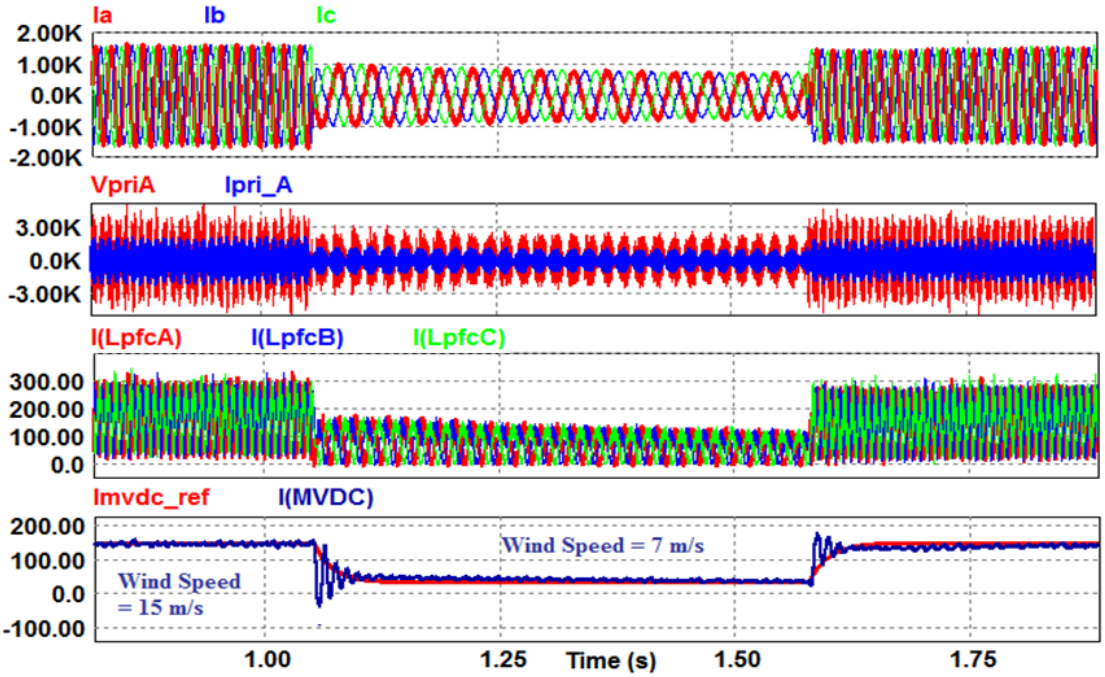

Figure 4-11: Simulation waveforms of step change between 100% and 25% WTG power (15 m/s to 7 m/s)

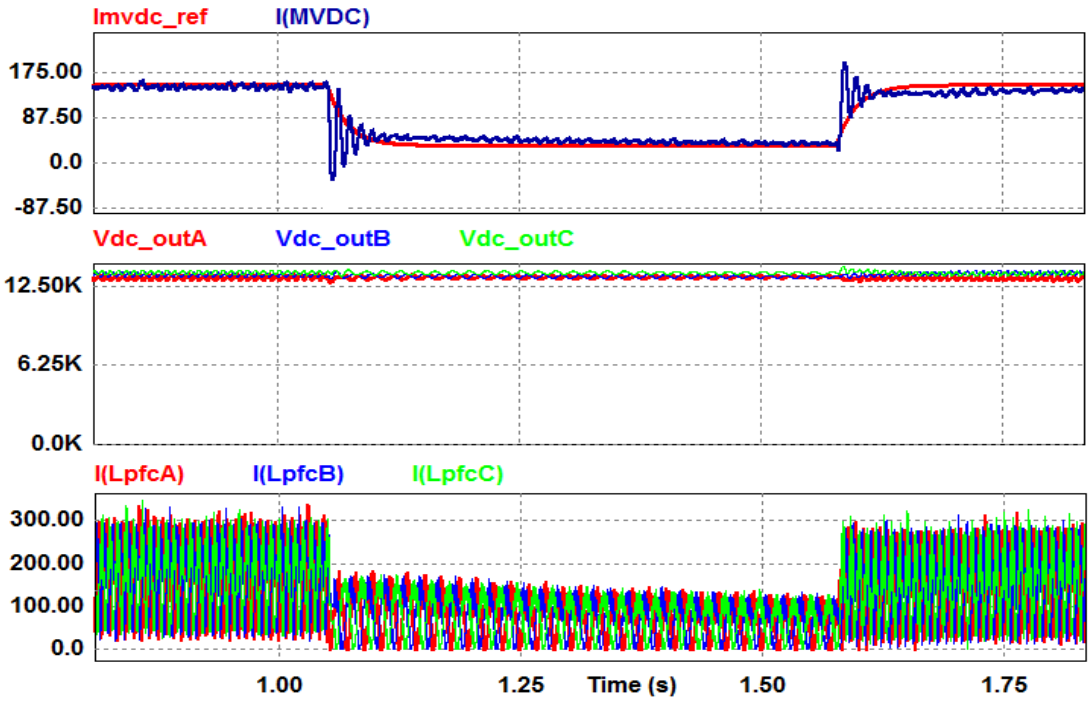

Figure 4-12: PSIM Simulation step change – boost PFC voltages

There are some oscillations in the boost PFC inductor currents, caused due to the L-C resonances between the output capacitor and the MVDC inductor, and triggered by the voltage resonances at the WTG terminals (see V_a in the first plot of Figure 4-9). The three WTG currents are near sinusoidal. The boost PFC inductor currents and the transformer currents also reflect the resonances at the WTG terminals. Since these oscillations are not large and the WTG & MVDC currents are of good quality, these intermediate voltage and current levels can be accepted. Figure 4-11 and Figure 4-12 show the step change in wind velocity from 15 m/s to 7 m/s, which changes the power reference from 100% to 25% based on Figure 4-8. It can be seen that there are some transient oscillations in the MVDC current but these are within the rating boundaries. Moreover in a real system, the moment of inertia of the WTG will make the transients

slower. Figure 4-11 shows that the WTG currents' frequency has changed to track the frequency change in voltage and the MVDC current tracks the generated reference. From Figure 4-12, it can be seen that the DC output voltages of PFC stages from each phase are well regulated around the required 13.5 kV_{dc} levels. This shows that there are no voltage balancing issues while series connecting the systems. At still lower MVDC currents, the boost PFC current would go to discontinuous conduction.

The DC output capacitors output of PFC stages have to be pre-charged to near the required MVDC voltage before connecting the converter system to the MVDC bus. This will reduce large in-rush currents. The diodes in the PFC avoid circulating currents in the system. When there is less wind power available, the MVDC current can be slowly ramped down similar to how it is done in conventional systems. Once the wind velocity becomes less than cut-in speed of the WTG (around 3.5 m/s), the system does not transfer any power to the MVDC grid. This time, since the boost PFC operates in discontinuous conduction mode and due to the presence of diodes in the boost PFC, the output capacitors can retain their voltages. The advantage of the MVDC current control is that during a fault on the grid side, the current can be regulated at a low value so that there is no over-current. To implement the HCS algorithm along with the PSF MPPT, boost PFC reference voltage and frequency can be adjusted to reach the peak power.

4.7. Conclusion

This section proposed different MF transformer based approaches for the development of next-generation MVDC collection grids and associated converter topologies for offshore wind farms. The proposed WTG converter topology has been

shown to be suitable over a conventional approach for interfacing WTGs to an MVDC collection grid of +/- 20 kV in terms of mass and volume, which is anticipated to reduce the overall cost of delivering energy from offshore wind farms to shore. Different operating modes of the proposed approach have been analyzed and the proposed converter topology has been shown to be feasible with current state-of-the-art power semiconductor technology and transformer materials. The simulation results provided initial proof for the concepts and it could be seen that the control can support the typical WTG features such as MPPT, fault regulation, soft-start, etc.

5. WIND TURBINE - BATTERY ENERGY STORAGE UTILITY INTERFACE WITH MEDIUM FREQUENCY TRANSFORMER

5.1. Introduction to Energy Storage in Renewable Energy Systems

Renewable energy sources, such as wind and solar, have vast potential to reduce dependence on fossil fuels and greenhouse gas emissions in the electric sector. Climate change concerns, state initiatives including renewable portfolio standards, and consumer efforts are resulting in increased deployments of both technologies. Both solar photovoltaics (PV) and wind energy have variable and uncertain (sometimes referred to as "intermittent"). Because the wind doesn't always blow and the sun doesn't always shine at any given location, there has been an increased call for the deployment of energy storage as an essential component of future energy systems that use large amounts of variable renewable resources.

Interconnecting these intermittent sources to the utility grid at Mega-Watt scale may affect the voltage and/or frequency regulation. These conditions may jeopardize the stability of the grid, leading to severe power quality issues or even black-outs. Employing energy storage technologies to supplement the power produced from wind turbine generators (WTG), photovoltaic (PV) panels, etc. helps to address three main challenges: smoothing, capacity firming, and time-shifting. Thus an energy storage system is indispensable for the regulation of active power in a modern day grid. The storage elements used in the vicinity of WTGs can be batteries, electric double-layer capacitors (EDLCs), flywheels, etc. Among these, batteries and EDLCs have been of

major focus in the power electronics industry. However, their interface to the utility grid is challenging, especially in the medium voltage (MV) scale [67-70] WTGs can operate at maximum power coefficient over a wide range of wind speeds if operated in a variable speed mode [70]. Permanent Magnet (PM) WTGs are becoming more prominent for high power energy conversion mainly because of high power density and flexibility in operation. Direct drive power conversion scheme is popularly used for PM WTGs.

Several approaches have been reported in the literature to interface battery energy storage systems (BESS) with the utility [43, 71-73]. Figure 5-1 shows the conventional approach employing a line frequency transformer to charge/discharge a low voltage battery energy storage bank [71]. This approach requires a line frequency step-up transformer in order to be connected to a medium voltage grid. Figure 5-2 shows a PWM rectifier followed by a high frequency link DC-DC converter interfaced to a battery bank. This approach may not be suitable for MV utility interface, due to the presence of the simple 3-phase inverter. NPC inverters can be used if interfacing with a higher utility voltage is desired.

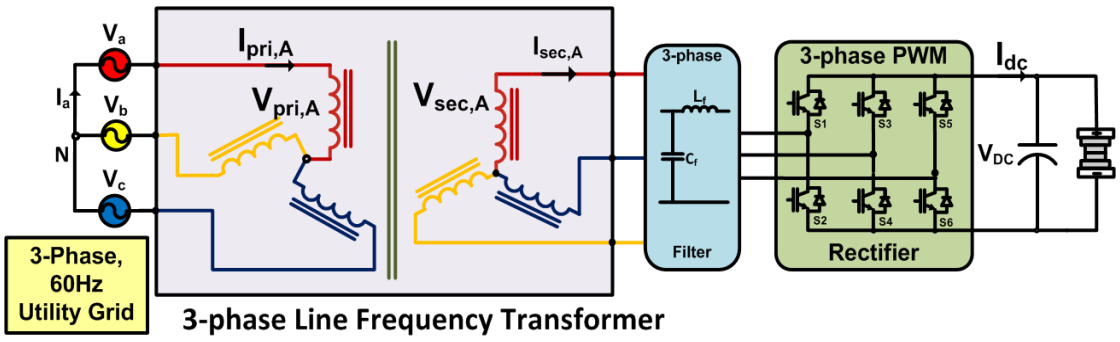

Figure 5-1: Medium voltage (or low voltage) utility - energy storage interface topology with line frequency transformer and PWM Rectifier

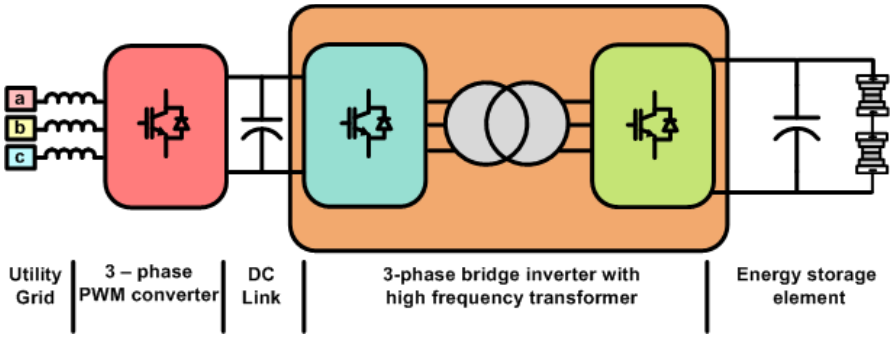

Figure 5-2: Lower voltage utility - energy storage interface topology involving high frequency transformer and two converter stages [73]

Reference [73] illustrates cascaded H-bridge based PWM rectifiers interfaced via a line frequency transformer. This approach requires several battery banks to be arranged in groups, thus requiring multiple charge balance approaches. A 10-MW, 40-MWh battery energy storage system has been described in the literature [74], that combines an 18-pulse voltage-source converter with lead-acid batteries where the dc voltage ranged from 1750 to 2860 V. Another concept with a 5-MVA 2.5-MWh battery energy storage system with lead-acid batteries based on parallel operation of 12-pulse converters to achieve the required power rating described in [72]. A common disadvantage with the above described approaches is the presence of bulky line frequency 50/60 Hz transformer in addition to complexity in control.

Many topologies to interface BESS with WTG systems have also been proposed and/or evaluated [75, 76]. Most of them propose different ways of integrating the BESS to the WTG system DC link, while other alternatives are interfacing the two systems at the utility side using separate line frequency transformers. The former method is good for lower power interface, but interfacing the two systems at the DC link at high power requires the use of transformers. The latter method also requires two separate bulky line

frequency transformers. If it is required to interface the BESS or WTG system with a MV at higher power density - may be in urban settings, island power systems or micro-grids - these topologies may be at a disadvantage. 3-port configurations using dual/triple active bridges to interface renewable energy sources are proposed in [8, 45, 77-79]. A similar 3-port configuration can be used for WTG-BESS MV grid integration as well, with suitable modifications in topology, which can reduce one set of transformer windings. This section first introduces a new MV BESS grid interface converter topology with medium frequency (MF) link transformer isolation, and then later explains the interconnection of a WTG-BESS system with the utility grid.

5.2. Proposed Battery Energy Storage - Utility Interface Converter

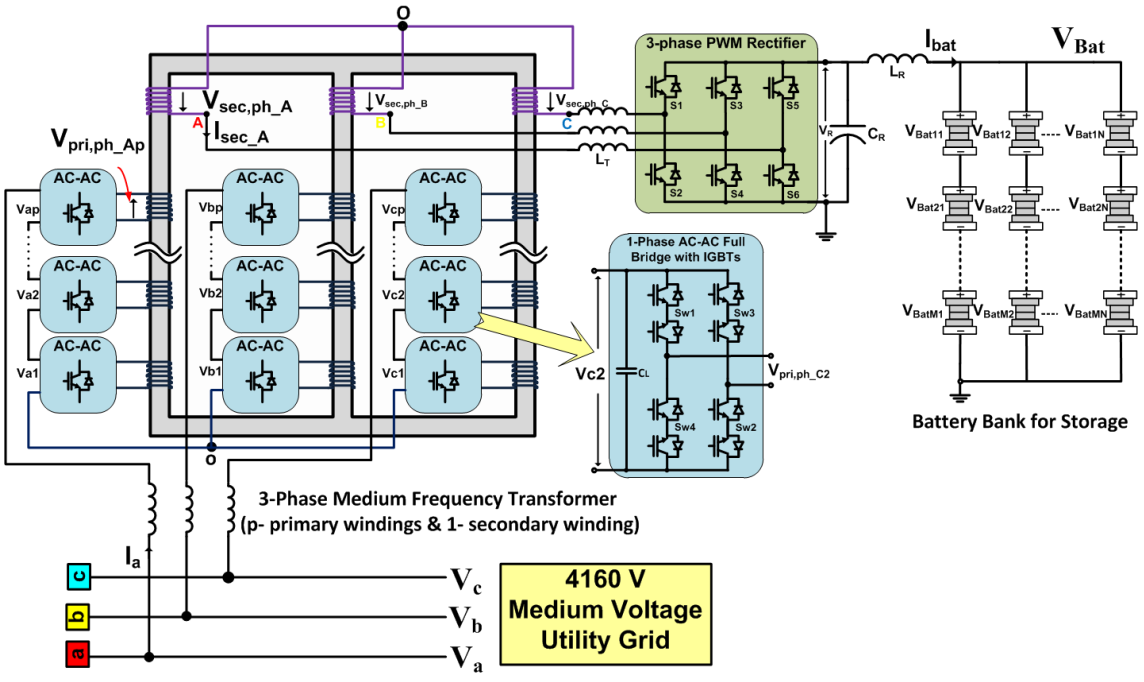

Figure 5-3: Proposed BESS - MV utility interface converter topology using MF transformer isolation

The design of the proposed topology [80] in Figure 5-3 can be divided into the following 5 sub-sections: (1) Multi-level AC-AC converter, (2) BESS, (3) 3-phase PWM rectifier, (4) Medium frequency transformer, and (5) Control strategy.

5.2.1. Multi-Level AC-AC Converter

The AC-AC converter for each phase is made up of multiple levels of 1-phase AC-AC H-bridges with bi-directional switches constructed with IGBTs/MOSFETs coupled in anti-series configuration (see Figure 5-3). Assuming that the IGBTs are rated at 1700 V, the maximum rms input voltage per each level of AC-AC converter (after sufficient derating) is 1100 V_{LL}, 3-phase. In order to interface 4160 V_{LL} ($V_{a,rms} = 4160/\sqrt{3}$), there should be at least four such AC-AC full bridges stacked in series for each phase. Each level of the AC-AC converter is modulated with a medium frequency ($f_{sq} = \omega_{sq}/2\pi$) square wave. As discussed before, the switching functions associated with the AC-AC converter can be given by (2.1), (2.2) and (2.3). Otherwise the operation of the AC-AC converter is similar to those explained in previous sections.

5.2.2. Battery Energy Storage System (BESS)

A 900 $V_{dc,\ max}$, 1 MW / 3 MWhr Lithium Ion based BESS is assumed in this system for design and simulation purposes. At times of high demand, the BESS will discharge its energy onto the grid. During low demand, the BESS will charge itself, which typically takes longer time. Thus the BESS operates based on the demand-supply gap and smoothens the power delivered to the utility grid. Typical battery types used in high power energy storage applications are: Lead-acid, Li-Ion, Ni-Cd, Zinc Bromine,

NaCl-Ni, etc. Li-Ion battery has become very attractive for high power energy storage, mainly due to high efficiency, low voltage fluctuation and high energy density. It is preferred to have the battery bank voltage within 1000 V_{dc} for having more parallel connected cells and less series connected cells. This will simplify the charge balancing process in the battery bank and will improve the power density of the system. For the proposed system, the maximum voltage of the battery bank is assumed to be 900 V_{dc} during full charge and discharged up to 450 V_{dc} during peak load. In order to support an average load of 1 MW for around 3 hours during the peak demand within a day, the battery bank has to be designed for 3 MWhrs.

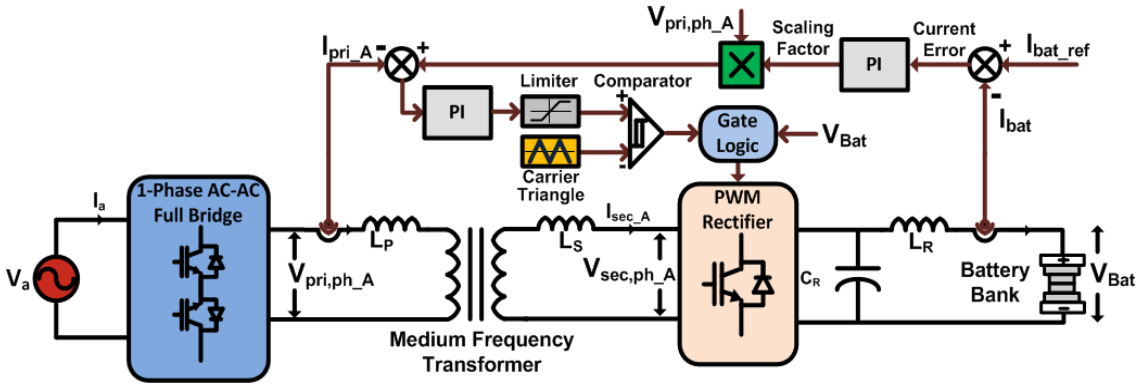

Figure 5-4: Per-phase control strategy at the MF transformer of the proposed topology for demand based power flow regulation among the grid and BESS

5.2.3. 3-Phase PWM Rectifier/Inverter

For bi-directional active power transfer across the transformer (see Figure 5-4), the BESS side rectifier (*inverter while discharging*) should generate all the major frequency components present in $V_{pri,A}$. Thus, the switching function of the PWM rectifier must be a product of a line frequency sine wave and a MF square wave,

appropriately phase-shifted depending on the amount of power to be transferred (achieved by PI control of transformer phase currents by forcing the currents' shapes to be similar to transformer primary voltages). The transformer leakage inductances act as the power transferring reactors. Considering the peak BESS voltage as 900 V_{dc}, 1700 V IGBTs can be employed to attain around 1000 A_{pk} current rating for a system power of 1 MW. The per phase active power (P_{a1}) transferred to the utility side at a single level across the transformer from the BESS can be given by (5.1) and (5.2).

$$P_{a1} = K \cdot \sum_{\substack{f=(f_{sq}+f_s),\\ (f_{sq}-f_s),\\ (3.f_{sq}+f_s),\ldots}}^{f=\infty} \left\{ V_{pri_A}^{(f)} \cdot V_{sec,wtg\_A}^{(f)} \cdot \left[\frac{\sin \delta^{(f)}}{f} \right] \right\} \tag{5.1}$$

$$K = \left(\frac{n_1 \cdot n_2}{2 \cdot \pi \cdot (n_2^2 \cdot L_p + n_1^2 \cdot L_s)} \right) \tag{5.2}$$

where n_1, n_2 are the number of transformer primary and secondary turns, respectively; L_p, L_s are the transformer primary and secondary leakage inductances (assuming that the transformer winding resistances are small); $V_{pri\_A}^{(f)}$ and $V_{sec,wtg\_A}^{(f)}$ are respectively the primary and secondary transformer phase voltage (rms) components in the frequency spectrum with a frequency of 'f'; and $\delta^{(f)}$ is the phase difference across the transformer primary and secondary voltage components with frequency, f.

5.2.4. Medium Frequency (MF) Transformer

Medium frequency (MF) transformer design is again similar as in previous sections, and will be detailed in section 6. Based on the AC-AC converter and PWM rectifier operations, the minimum transformer turns ratio can be calculated by (5.3):

$$N = \frac{n_2}{n_1} = \left(\frac{1}{2\sqrt{2}}\right) \cdot \left(\frac{V_{Bat(min)}}{V_{a(rms)}}\right) \quad (5.3)$$

For a $4160V_{LL}$ utility input, and at $450V_{dc}$ minimum battery voltage, the transformer turns ratio required is n_2:n_1 = 1:15 (considering the primary windings across all levels). If the battery voltage variation is reduced, the turns-ratio can be increased.

5.2.5. Control Strategy

The detailed control strategy adopted for the proposed system (see Figure 5-3) can be seen in Figure 5-4 (only one transformer phase is shown for simplicity, but it also applies for other transformer phases of the proposed topology) for controlling the charging/discharging of BESS. The control mainly consists of two current loops – (a) the external loop regulating the DC current, I_{bat}, with a bandwidth of close to *100 Hz* or below (as per the system speed requirement) and (b) the internal loop regulating the transformer current, $I_{pri,A}$, with a bandwidth of at least *five* times the MF (here, *3-4 kHz*); which is due to exactly replicate the transformer voltage shape to the current as well, where up to 5^{th} frequency component are essential. There will be two more such internal loops for the other transformer phase currents. The outer loop is common for all the inner loops and will typically be slower than the inner loops.

On the utility side, the input capacitors and the multiple windings in the transformer will assure the voltage to be distributed evenly across the windings. As the AC-AC converter is modulated with a square wave, the transformer windings experience such a 'multiple-frequency' voltage waveform. The controller senses these voltages for uniformity and evaluates the grid demand to calculate how much current must flow at any time. This information is used to control the BESS DC current by switching the

PWM rectifier on that side. Based on the deficit or excess of power for the particular demand, the battery current reference is adjusted to either supply or absorb power. To do that, the error from the BESS current reference and the instantaneous current is processed to calculate the scaling factor that is multiplied with the transformer primary voltage to evaluate the transformer current.

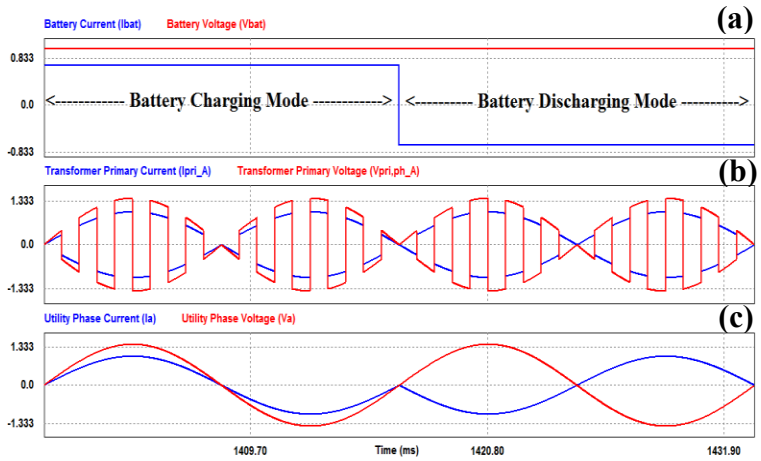

Figure 5-5: Idealized operating waveforms of the proposed system for battery charging and discharging modes - (a) Battery voltage and current, (b) MF transformer AC phase voltage and current, and (c) Input AC phase voltage and current

Figure 5-5 shows the idealized per-unit voltages and currents at different terminals of topology in Figure 5-3. Figure 5-5 (a) shows the battery DC voltage and current. It can be noticed that the battery current is positive during charging mode and negative during discharging mode. Figure 5-5 (b) shows the transformer medium frequency AC voltage and current. It can be seen that the current flips during the discharging mode and becomes out-of-phase with the voltage. Figure 5-5 (c) shows the input grid voltage and current. Here too, the input current is in phase with the input voltage during the battery charging mode when the power is fed into the battery bank

from the utility. The current then becomes out-of-phase with the input voltage during battery discharge mode, when power is transferred from the battery bank to the utility.

5.3. Proposed WTG-BESS Utility Interface Converter in 3-port Configuration

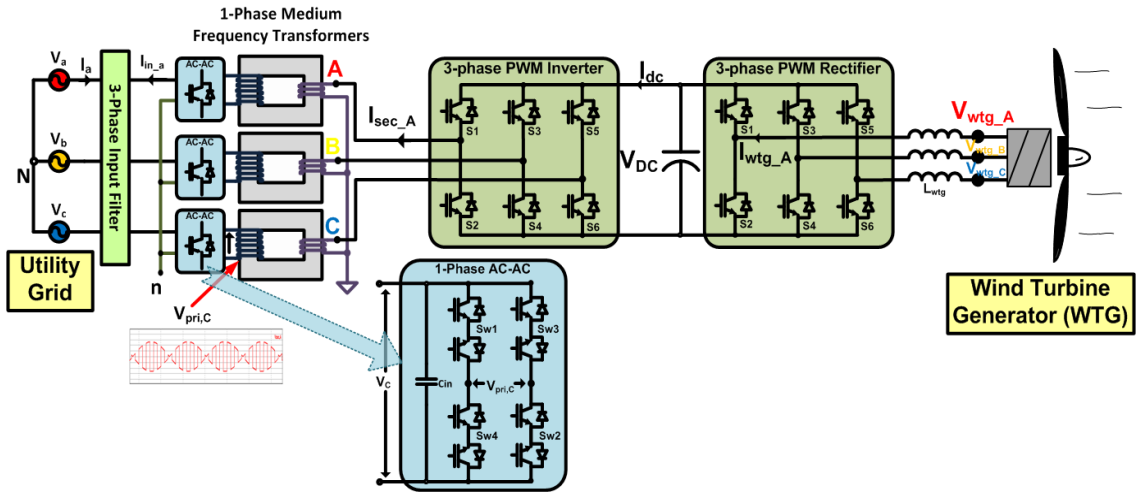

Figure 5-6: WTG Utility Interface with MF Transformer

The earlier sub-section explained the proposed BESS – utility interface converter topology. The concept can be applied to WTG – utility interconnection as well by assuming it has a PWM rectifier that converts the WTG voltage to a fixed DC, after which the operation is similar as in a BESS based system with the difference that the power flow is almost always unidirectional (flowing from the WTG to the utility). Such a system is shown in Figure 5-6. Now, the two topologies proposed in Figure 5-3 and Figure 5-6 can be combined and optimized to form a 3-port system as in Figure 5-7.

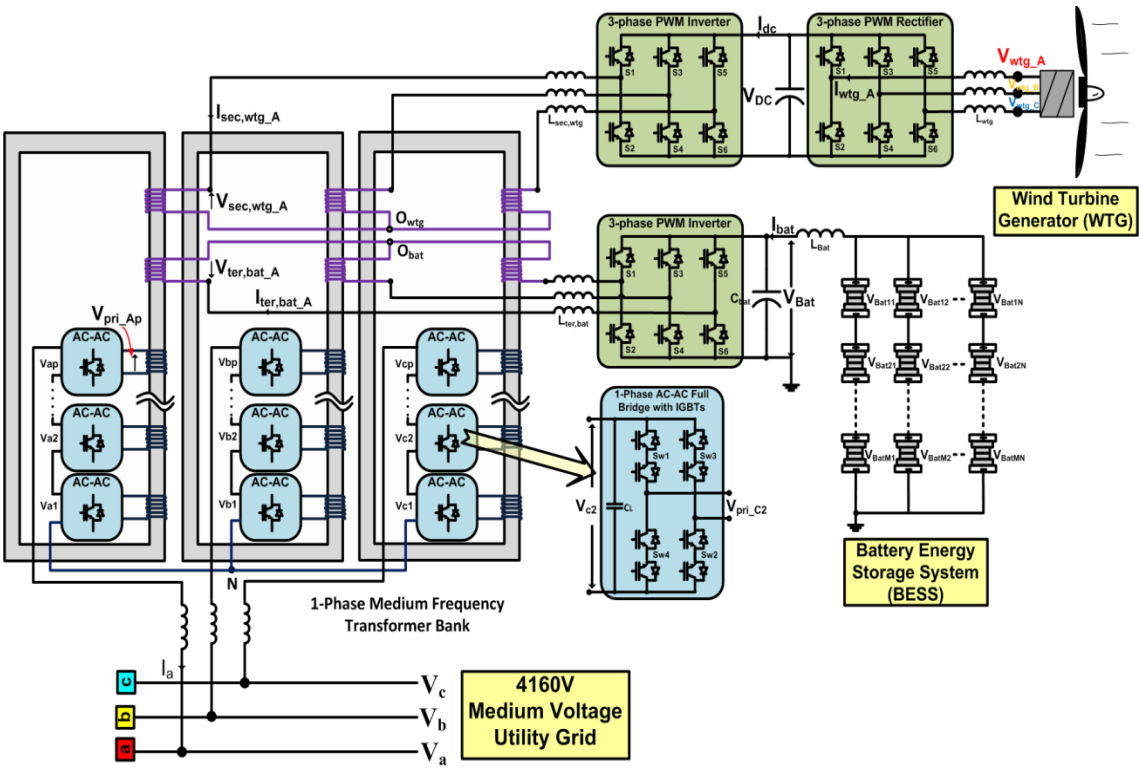

Figure 5-7: Wind Turbine Generator – Battery Energy Storage Converter 3-port Configuration with Medium Frequency Transformer Isolation for Utility Grid Integration

The WTG-BESS utility interface system in Figure 5-7 involves a MF transformer with three sets of windings to form a 3-port configuration with series stacked AC-AC converters on the MV utility side, 3-phase PWM rectifier and an inverter on the WTG side, and a 3-phase PWM inverter on the BESS side. Interconnection of BESS along with WTG provides a path for re-directing the energy flowing from WTG to the utility grid towards the BESS during low voltage ride through (LVRT). It can be shown that the utility grid sinusoidal currents, the battery current and the WTG input currents are of good quality; at the same time, the transformer voltages are of MF. The major advantages of the proposed system [27] are:

- The MF link transformer provides galvanic isolation as well as proper voltage matching between the utility, the WTG and the BESS. It also contributes to reduced size/weight while maintaining good transfer efficiency.
- A single transformer can be used for interfacing both WTG and BESS systems to the utility grid. The leakage inductances of the MF transformer are used as power transfer reactors; there is no need for external inductors. One set of windings is reduced.
- The AC-AC converters and PWM rectifiers are modulated to make utility and WTG power factor near unity.
- As the AC-AC converters are switched at MF, the switching losses are low.
- The controller can handle voltage sags and swells without any significant change in topology or strategy.
- The proposed strategy is flexible, allows for high switching frequency operation on the PWM rectifiers, ensuring that the transformer core is operated at constant MF over entire range.
- LVRT can be implemented with minimal change in the topology.

The design of the entire topology in Figure 5-7 can be broadly divided into the following 5 sub-sections as before: (1) Multi-level AC-AC converter, (2) WTG and BESS, (3) 3-phase PWM rectifier and inverter, (4) Medium frequency transformer, and (5) Control strategy.

5.3.1. Multi-Level AC-AC Converter

There is no major change in the AC-AC converter design and operation here compared to the section (*5.2.1*), discussed earlier.

5.3.2. Wind Turbine Generator (WTG) and Battery Energy Storage System (BESS)

A 1100 V_{LL}, 2 MW, 20 Hz_{max} Permanent Magnet WTG is assumed for the simulation purposes, which is interfaced with a 900 $V_{dc,\ max}$, 1 MW / 3 MWhr Lithium Ion based BESS as discussed before. At times of high demand or low wind, the BESS will try to offset the power generated by the WTG by discharging its energy onto the grid. During high wind or low demand, the BESS will charge. Thus the BESS operates based on the demand-supply gap and smoothens the power delivered to the utility grid. The WTG power is controlled in the simulation using conventional torque adjustments and DQ Control on the PWM rectifier side (not the focus of this section).

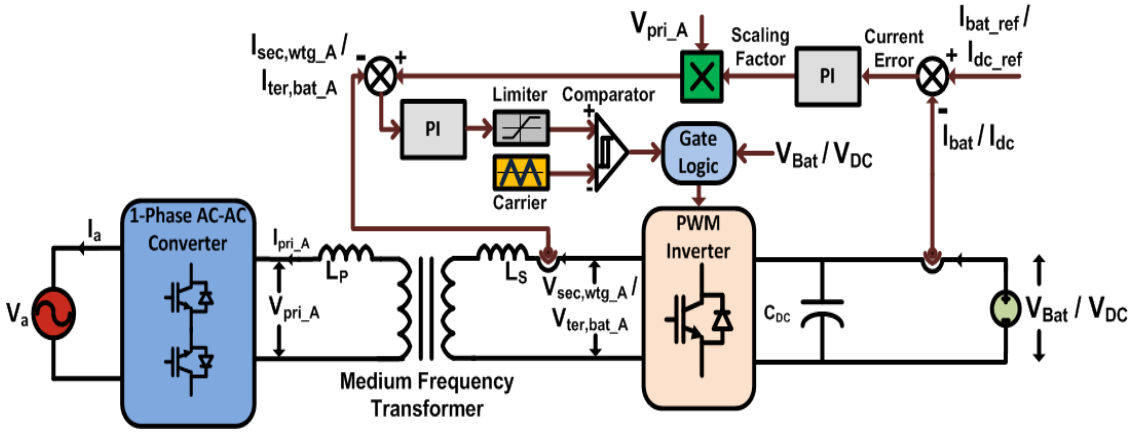

Figure 5-8: Per-phase control strategy at the MF transformer of the proposed topology for demand based power flow regulation among the grid, WTG and BESS (strategy similar for WTG as well as BESS side)

5.3.3. 3-Phase PWM Rectifier and Inverter

Figure 5-8 shows a single-level per-phase diagram of the proposed topology along with the control strategy. The voltage applied to the transformer primary, V_{pri_A} induces voltages on the secondary winding V_{sec,wtg_A} as well as the tertiary winding V_{ter,bat_A} based on the turns-ratio. The PWM rectifier at the WTG side is governed by conventional DQ control to transmit available wind power to the DC-Link. The DC-Link voltage on the WTG side, V_{DC} is regulated at 1500 V, suitable for the PWM inverter operation. Operation and control of PWM inverters on the secondary and tertiary windings is similar. Thus, the switching function of the PWM inverters is the same as discussed earlier, must be a product of a line frequency sine wave and a MF square wave. The power transfer equations are also similar and given by (5.1) and (5.2). The proposed topology in Figure 5-7 has only one set of transformer tertiary windings with a 3-phase PWM inverter for BESS. But this modular system can be expanded in terms of power rating by adding more windings along with PWM inverters and battery banks.

5.3.4. Medium Frequency (MF) Transformer

Medium frequency (MF) transformer design is detailed under section 6.

5.3.5. Control Strategy

The detailed control strategy adopted for the proposed system can be seen in Figure 5-8 (only one transformer phase is shown for simplicity, but it also applies for other transformer phases of the topology in Figure 5-7) for controlling the power flow from the WTG to the utility grid as well as charging/discharging of BESS. The control mechanism is exactly the same as before, consists of two current loops – (a) the external

loop regulating the DC current, I_{bat} or I_{dc} and (b) the internal loop regulating the transformer secondary/ tertiary currents, I_{sec,wtg_A} and I_{ter,bat_A}.

It may be noted that the WTG is controlled in such a way that it is always desired to derive the maximum power out of it. Based on the deficit or excess of power for the particular demand, the battery current reference is adjusted to either supply or absorb power. To do that, the error from the BESS current reference and the instantaneous current is processed to calculate the scaling factor that is multiplied with the transformer primary voltage to evaluate the transformer current.

Now at the WTG side PWM rectifier, DQ control regulates the DC-Link voltage. The PWM inverter on the WTG side works similar to that on the BESS side, only that the reference for the DC-link current comes from the WTG available power at any instant. The inner PI controller can be replaced with hysteresis controller, which will also yield similar performance. It should be noted that as there is a single common outer loop and scaling factor, any imbalance in the transformer phase currents will be avoided as the control will make sure that the power is transferred equally across all the phases. It will also help in appropriate division of voltage between the windings of multiple levels. Since the power flow mechanism is a current control scheme, both sides of the B-H curve are used in the transformer and thus the core saturation can be reduced. The utility currents will have small amount of twice the MF components due to transformer current transients; these harmonics can be filtered using an LC filter.

5.4. Low Voltage Ride Through (LVRT) Capability

WTGs are generally required to be capable of LVRT when the voltage in the grid is temporarily reduced due to a fault or load change in the grid. The voltage may be reduced in one, two or all the three phases of the AC grid. The severity of the voltage sag depends upon the voltage level it reduces to and the duration [81-83].

In USA, the Federal Energy Regulatory Commission (FERC) specifies an LVRT requirement in Appendix G of its Order No. 661, Large Generator Interconnection Agreement (LGIA) which was issued on June 2, 2005. An applicable WTG would be required to remain operational during a grid fault as shown in Figure 5-9. NERC proposed a more stringent requirement for WTGs to remain online even with grid voltage falling to zero volts for a few cycles [82, 83]. During unbalanced voltage sags, the grid codes require wind turbine utilities to reduce the active power and supply reactive power to support the grid till the grid comes back to normal.

In a conventional WTG system (Figure 4-1) when disturbance occurs in the utility grid, the voltage at the AC output terminals of the WTG drops. The output power of the inverter can be quickly reduced. However, the power generated by WTG cannot be reduced at the same rate. This creates an energy mismatch between the power generated by the WTG and the power delivered to the utility grid. This energy difference will cause a voltage surge at the DC-link capacitor. A very large voltage may damage the power devices as well as the capacitor [83]. These issues need to be overcome while incorporating LVRT capability. One way to reduce the voltage surge is by dumping the

excess energy into a DC-link chopper as shown in Figure 5-10. If the energy mismatch is large, then the chopper rating has to be sufficiently high.

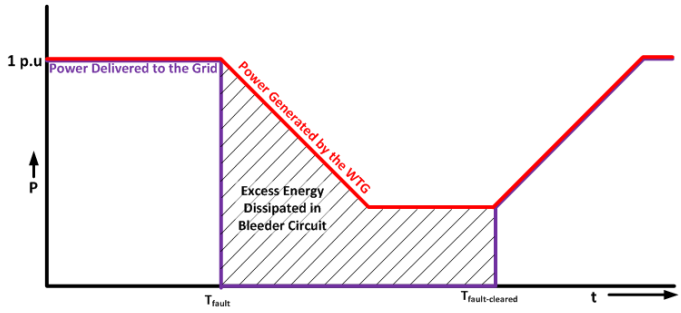

Figure 5-9: Energy Profile during conventional LVRT

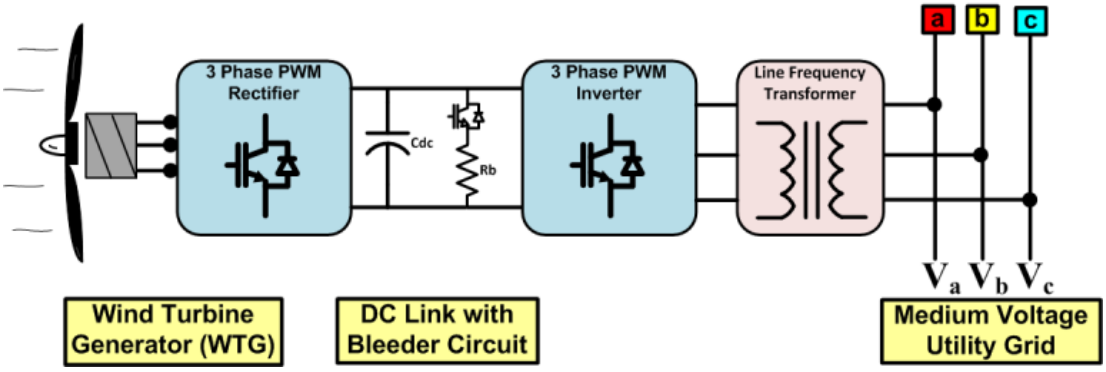

Figure 5-10: Conventional WTG Power Converter with chopper circuit for LVRT Capability [83]

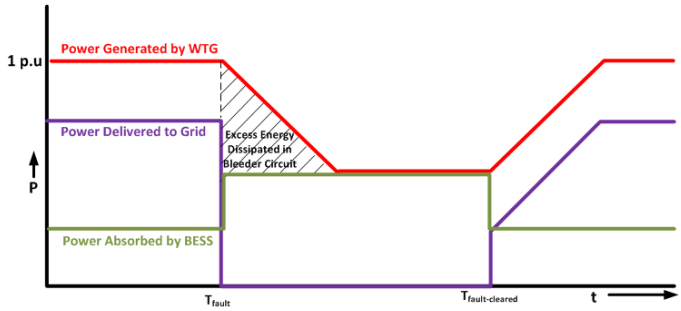

Figure 5-11: Energy profile during LVRT for the proposed topology with DC-link chopper (bleeder)

Figure 5-9 shows the energy profile of WTG during a fault condition, along with DC-link chopper based LVRT capability. It can be seen that the energy to be dissipated in the chopper is large (indicated by the shaded area) as the WTG takes some finite time to activate pitch control and reach a low power stage. During this time, there is a larger tendency of the DC-Link capacitor voltage to increase unless the chopper can absorb the excess energy during temporary fault. The WTG system has to be tripped if the fault persists for more than the stipulated number of cycles.

In the proposed system, the BESS can be controlled to reduce the amount of active power to be supplied to the grid. In case the BESS does not have enough rating to absorb any more current, a DC Chopper can be used to dump excess energy. The BESS can also supply reactive current during the sag. The controller determines the amount of reactive power to be supplied and commands tertiary battery current to be out of phase of tertiary voltages by the required angle. Once the grid is back to normal, the phase is reduced to zero and the normal supply of active power to the grid is resumed.

Figure 5-11 shows the methodology that can be employed using the proposed system for LVRT capability. When a fault occurs, it is quickly sensed and the BESS system will start absorbing the WTG energy. Just in case the WTG is operating at full power and the BESS is not rated for power equal to the WTG, a chopper circuit is still required, but the rating can be much smaller as the excess energy that needs to be dissipated is small (shown by the shaded area in Figure 5-11). The AC-AC converter at the utility side is switched normally during fault. The chopper will stop once it has consumed the excess energy. The BESS delivers the required reactive current to support

the grid until the fault clears. Thereafter, full active power can be directed to the utility grid. In case the fault is more severe, the BESS can keep absorbing the power generated by the WTG until it is fully charged and the WTG can be kept online for much longer duration. Thus, the system reliability and power availability can be improved.

5.5. Simulation Results

Table 5-1: Simulation parameters

Sl. No	Parameter	Value
1	Utility Side Specification	4.16 kV, 60 Hz
2	WTG Specification	1.2 kV, 7-15 Hz
3	BESS Specification	900 V, 3 MWhr
4	Si Steel Transformer Core	600 Hz, 0.55 T
5	Transformer Turns-ratio	15:1
6	Leakage/Filter Inductances	5%

The topology in Figure 5-7 was simulated using PSIM for a 4160V medium voltage utility grid. Table 5-1 shows the different system parameters used in simulations. Figure 5-12 and Figure 5-13 show the important current and voltage waveforms of the proposed topology during the BESS charging mode as well as BESS discharging mode, respectively. It can be seen from Figure 5-12 (a) that the real power supplied to the utility grid is the net sum of power generated by the WTG and the power generated/absorbed by the BESS. The negative value of battery current, I_{bat} shows that the batteries are charging. The WTG current, I_{wtg_A} shown in Figure 5-12 (b) are regulated by DQ control strategy that gets the information of available power using various speed/torque sensors. Figure 5-12 (c) shows the utility grid side voltage V_a and

unfiltered grid current, I_a. The current has some low energy spikes caused due to transformer current transients. It can be seen from Figure 5-12 (d) that the secondary and tertiary transformer currents (I_{sec,wtg_A} and I_{ter,bat_A}) try to follow the primary voltage (V_{pri_A}). I_{ter,bat_A} is in-phase or out-of-phase depending on whether power is being absorbed or released by the BESS, which depends on instantaneous grid demand.

Figure 5-13 shows the currents and voltages described using Figure 5-12, but during the BESS discharging mode. The battery current is positive (Figure 5-13 (a)), which shows that they are discharging. The utility current, I_a in Figure 5-13 (c) can be seen to be increased compared to the one in Figure 5-12 (c) as the utility now derives power from both the WTG as well as BESS. Thus, the transformer secondary and tertiary currents shown in Figure 5-13 (d) can be seen to be in-phase with transformer primary voltage. The battery current, I_{bat} is regulated within a pk-pk ripple of 20%.

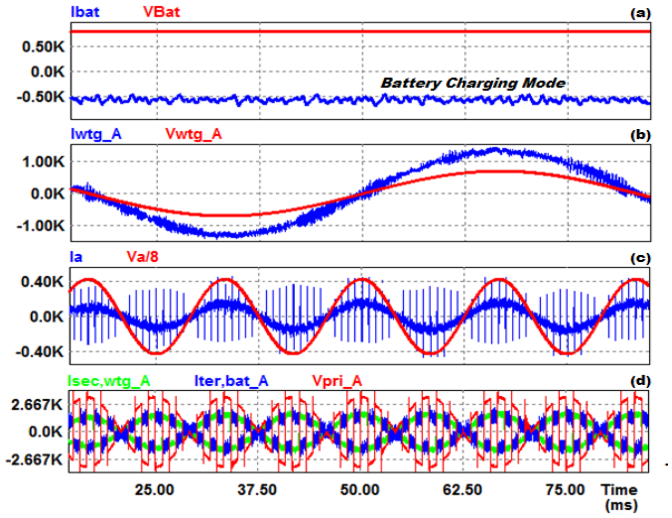

Figure 5-12: Charging mode waveforms- (a) BESS current and voltage (for V_{Bat} = 800V, I_{bat} = -500A (b) WTG phase-A current and voltage (15Hz), (c) Unfiltered utility grid phase-A current and 1/8th of utility voltage (scale reduced *for better resolution of current*) and (d) Transformer secondary current, tertiary current and cumulative primary phase-A voltage

Figure 5-14 (a), (b) show the transformer level-1 primary (V_{pri,ph_A1}) and secondary (V_{sec,ph_A}) voltages, respectively. Figure 5-14 (c) and (d) respectively show the FFTs of waveforms in (a) and (b). It can be observed that the while the primary voltage has an envelope of 60Hz sine wave, the secondary voltage has a PWM shape (being generated by the PWM inverter). Yet the FFTs of both the waveforms look similar (considering the turns-ratio). The controller modulates the PWM rectifier in such a way that all the major frequency components are present at the transformer secondary, so that active power can be transferred through the transformer.

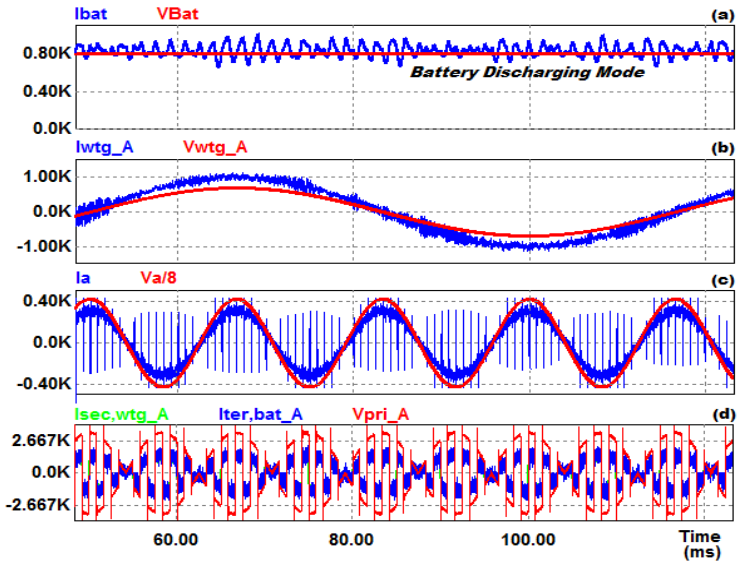

Figure 5-13: Discharging mode waveforms- (a) BESS current and voltage (for V_{Bat} = 800V, I_{bat} = 800A (b) WTG phase-A current and voltage (15Hz), (c) Unfiltered utility grid phase-A current and 1/8th of utility voltage and (d) Transformer secondary current, tertiary current and cumulative primary phase-A voltage

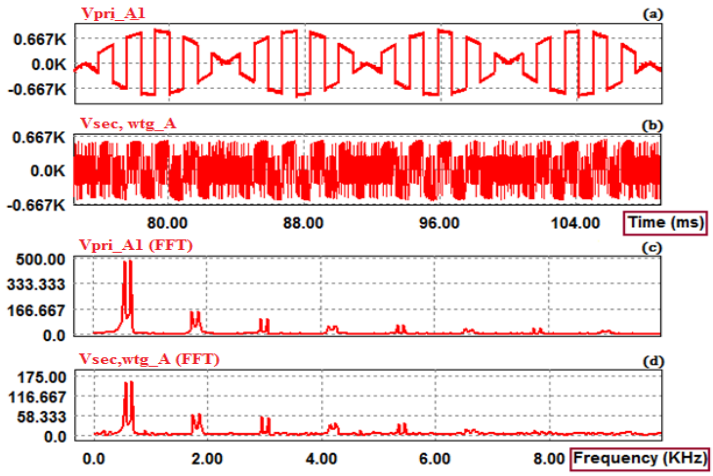

Figure 5-14: (a) Transformer phase-A primary voltage, (b) Transformer phase-A secondary voltage, (c) and (d) are respectively FFTs of (a) and (b)

Figure 5-15 shows variation in utility grid current with respect to slow step changes in BESS current as well as WTG generated power. It can be seen that for a short time, the power generated by WTG is entirely used to charge the BESS. The net power between the utility, WTG and BESS are seen to be properly balanced. Figure 5-16 (a) shows the LVRT functionality of the proposed system when WTG is delivering full power (2MW) and a fault occurs at phase-A. It can be seen that the DC-Link voltage rises only around 20%. The DC-link chopper circuit operates when the voltage crosses 1800V and quickly brings the capacitor voltage back to normal, because the BESS is absorbing the power from the WTG and the utility is drawing only a small amount of active power during this time as required. Thus, the WTG does not have to be tripped even if the fault prolongs for some more time. Figure 5-16 (b) shows that the converter can support the grid with reactive power during LVRT.

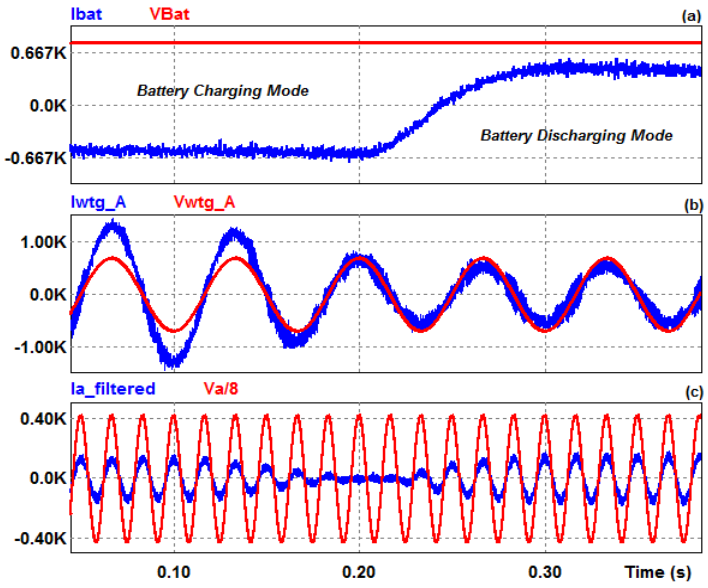

Figure 5-15: Variation in grid supply effected by WTG and BESS based on the instantaneous power demand (a) BESS voltage and current, (b) WTG voltage and current, and (c) Utility grid voltage and current (grid voltage shown on a reduced scale for better resolution)

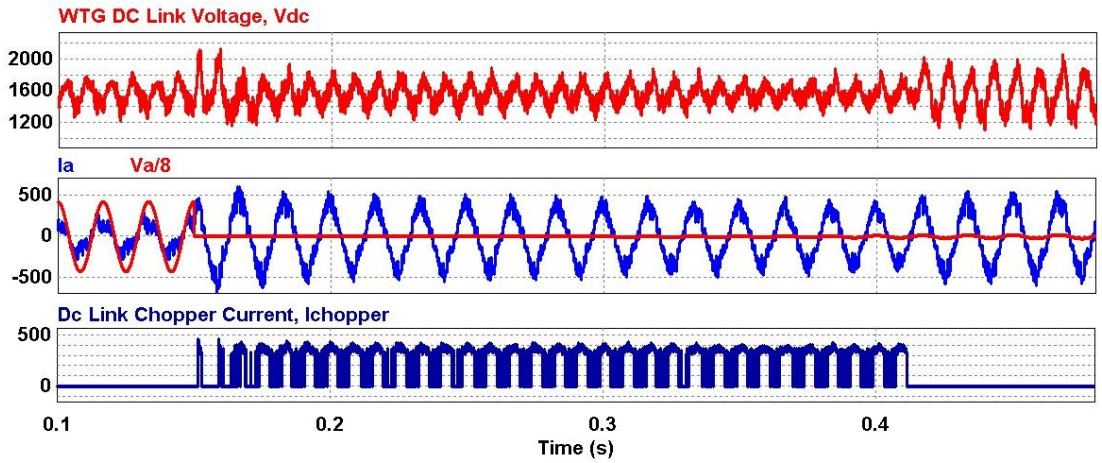

Figure 5-16 (a): Voltage rise in the WTG DC-link capacitor during a temporary line-to-ground fault in phase-A. chopper circuit operates when the DC-Link voltage crosses 1800V.

Figure 5-17: shows the operation of the proposed control strategy (see Figure 5-8) during voltage swell and sag events. The simulation was performed with 20% swell followed by 20% sag of the utility grid voltage, each persisting for 3 cycles. It was

desired that the battery current, I_{bat} adjusts itself to make the utility grid currents remain nearly the same even during voltage swell/sag events.

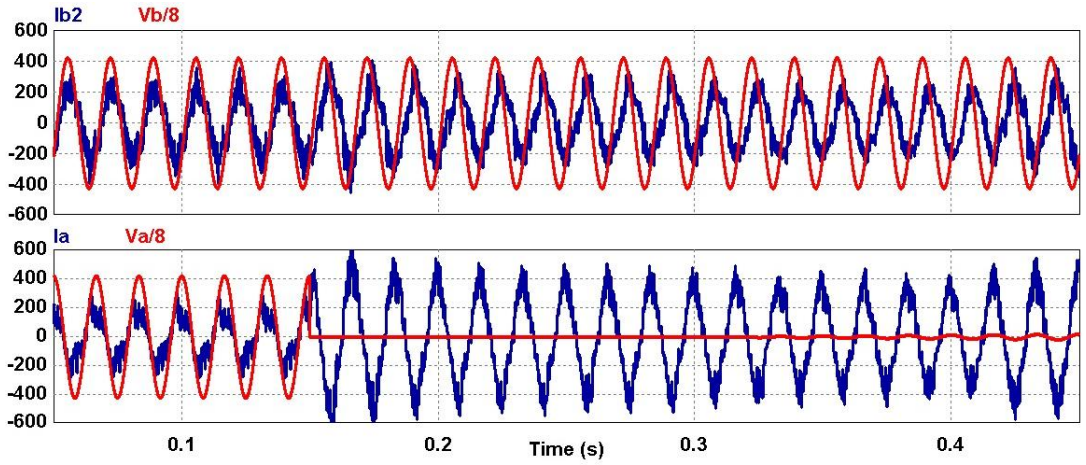

Figure 5-17: Utility voltages and currents in phase-B and phase-A during a line-to-gnd fault in phase-A.

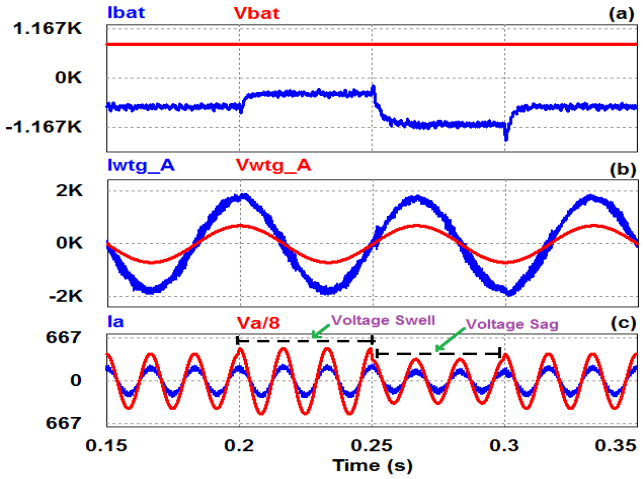

Figure 5-18: Control system performance under utility grid voltage swell and sag – (a) BESS voltage and current, (b) WTG voltage and current, and (c) Utility grid voltage and current (*grid voltage shown on a reduced scale for better resolution*)

In Figure 5-18 (a), it can be seen that the battery current adjusts itself according to the voltage swell/sag events shown in Figure 5-18 (c). The WTG current remains the same (see Figure 5-18 (b)) and the utility current also remains almost the same during

this period (see Figure 5-18 (c)). The power factor is also close to unity. Figure 5-19 shows a simulation of unbalanced sag with Line A voltage, V_a sagging to 60% and Line B Voltage, V_b sagging to 80%. Line C does not sag. Reactive power is provided by the battery till the fault is cleared and grid normalcy is restored. These simulation results show that the control is robust under various disturbances.

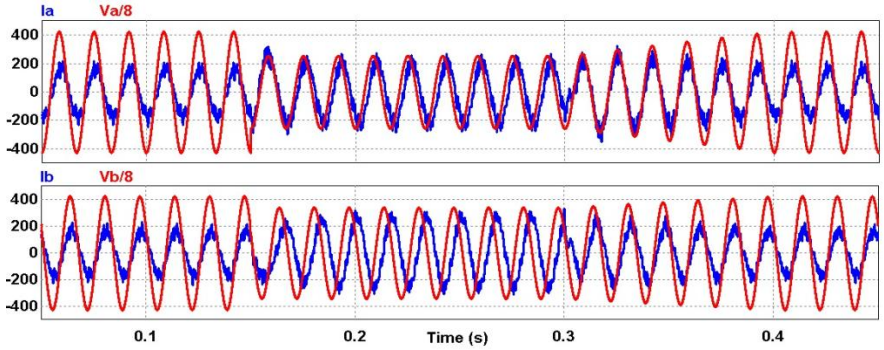

Figure 5-19: Control system performance under unbalanced sags in the utility grid voltages

5.6. Experimental Results

Table 5-2: MF transformer specifications

Parameter	Value	Unit	Parameter	Value	Unit	Parameter	Value	Unit
Ae	2.00	ADJ. ST.	*K3*	0.749		*Ww*	0.203	m
AeAc	12.48	REQ'D	*K2*K3*	0.235		*CoilW*	0.19	m
AeAc	8.00	SQ. ST.	*VA_tot*	6648	VA	*MLT*	0.232	m
AeAc	16.00	ADJ. ST.	*Bm*	0.623	T	*VOLT/T*	1.92	V/T
Wwt	2.5129	Kg	*Bac*	0.623	T	*SkinD*	0.003	m
Cwt	5.289	Kg	*Closs*	34.98	W			
Wvol	0.0012	cu. m	*Wloss*	40.01	W			
Cvol	0.0008	cu. m	*Trise*	79	deg C			

A 135V, 12A, 600Hz medium frequency transformer at 0.55 T flux density, with 4 windings was designed with the specification in Table 5-2. The efficiency of the

transformer was found by experiment to be around 97.5%. The next step was to analyze how the transformer core loss varies with the type of waveform it is operated with. For this, a scaled down prototype similar to the set-up in Figure 5-8 was built. Figure 5-20 shows AC-AC converter experimental waveforms from the prototype when supplied with 120 V utility voltage and with a *resistive load* of 1.2 kW on the secondary side, when the primary is switched with square wave modulation. Figure 5-20 also shows the thermal image of the MF transformer under test. With the core temperature rise test, it is not possible to assess the exact loss, but it provided an insight about the relative core loss variation for different waveforms. Same rms voltages and loads were applied to the transformer using the converter for the following operating conditions – i) 600 Hz sine, ii) 60 Hz sine multiplied by 600 Hz square modulation and iii) 60 Hz sine multiplied by 570 Hz square modulation. The transformer was kept running for 2 hours for each of the above conditions and the core temperatures were monitored using a thermal camera (assuming similar conduction losses).

Figure 5-21 shows the closed loop control waveforms of transformer primary and secondary voltages and current with a DC source on the secondary side as in Figure 5-8. The secondary side PWM inverter was switched at 12 kHz. The current in the transformer was regulated at the desired set point of 5A. It can be seen from Figure 5-21 that there are some high frequency components in the transformer primary current, which can be attributed to the PWM carrier frequency on the inverter that induces the current control. These components are eliminated by the filter on the utility side to maintain near-unity power factor. Since they are of low energy, LC filter will be small.

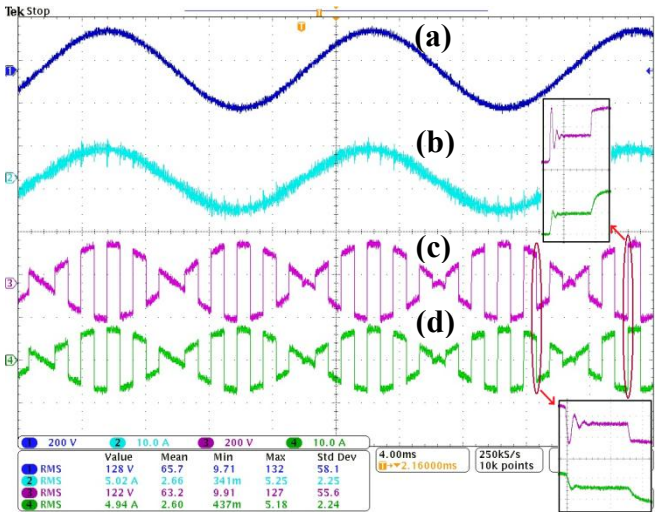

Figure 5-20: Experimental waveforms of utility side AC-AC converter phase-A with resistive load along with MF transformer. Channels 1, 2, 3 and 4 (a, b, c and d, respectively) show the grid voltage, grid current, transformer primary voltage and current, respectively.

Due to the slower ramping up of current compared to the voltage, any current control scheme will have a time constant to overcome, which appear as notches over the current envelope. Figure 5-21 also shows the transformer secondary voltage, which is generated by the PWM switching scheme. In order to transfer active power, the secondary voltage was a product of square PWM and sine PWM. The experimental waveforms look similar to the simulation waveforms. Figure 5-22 shows the step response in the current control for a 50% reduction in the primary current reference; along with the waveforms of the transformer primary voltage and utility grid voltage. It can be seen that the transformer current gets halved at middle (channel. 1)

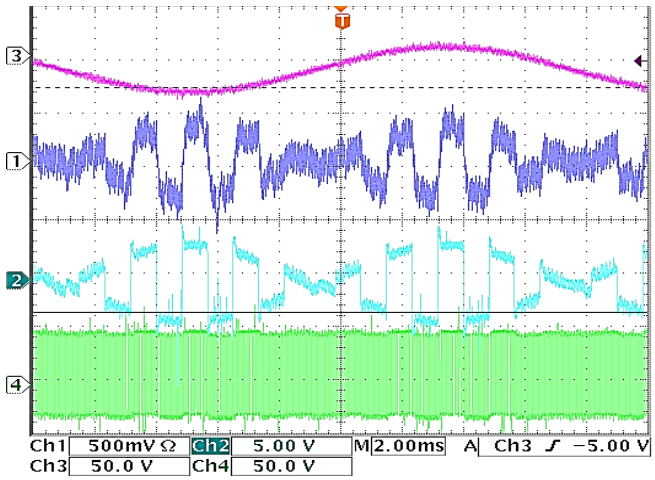

Figure 5-21: Experimental waveforms of MF transformer's (Ch.1) primary current, (Ch.2) primary voltage, (Ch.3) utility input voltage, and (Ch.4) transformer secondary voltage; with a prototype set-up as in Figure 5-8

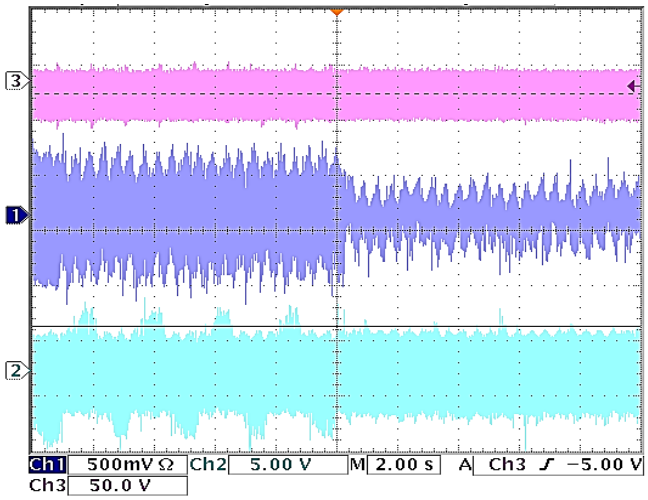

Figure 5-22: Experimental waveforms of (Ch.1) primary current, (Ch.2) primary voltage, and (Ch.3) utility grid voltage during a 50% step change in reference of grid power

Figure 5-23 shows the multi-level operation of the proposed topology on the AC-AC converter side. A 120 V voltage was applied across three series connected AC-AC converters whose outputs were fed to three windings of a 4-winding MF transformer. The fourth winding was connected to a resistive load via a rectifier. It can be seen that the voltages across all the transformer windings have balanced well with each other,

which proves that series-stacking multiple levels of AC-AC converters is possible in the proposed topologies. Figure 5-24 shows a section of the experimental set-up used for this topology, including the 600 Hz MF transformer and AC-AC converter.

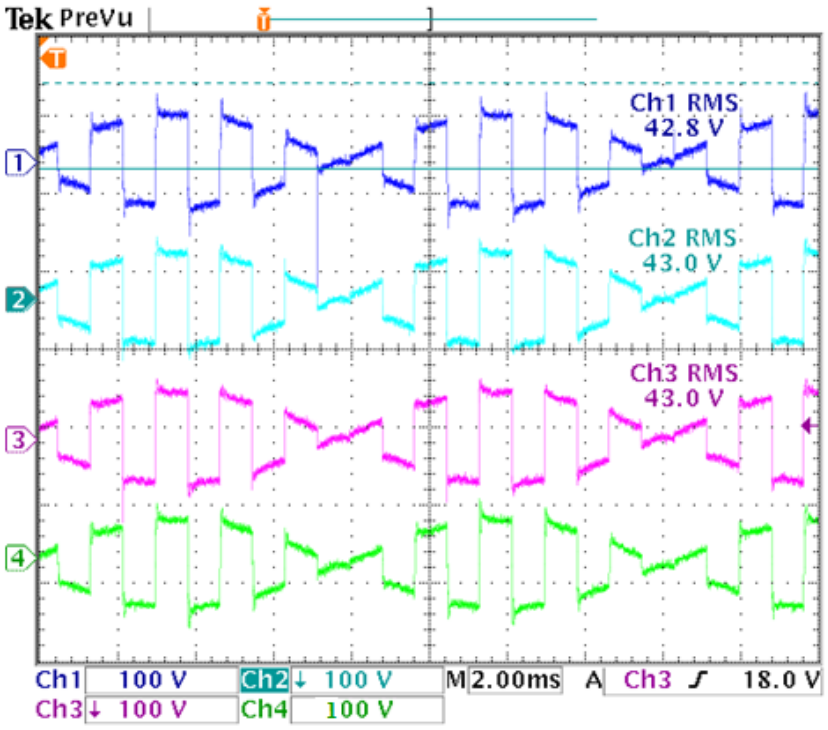

Figure 5-23: Multilevel Operation of AC-AC converter with a 4-winding MF transformer of 600 Hz connected with multilevel structure of AC-AC converters.

5.7. Conclusion

Three new topologies were proposed in this section for MV utility interface of wind turbine generators as well as battery energy storage systems. The basic concepts of the topologies and the main design equations for the voltages involving AC-AC converters, PWM rectifier and inverters were elucidated. Overall system simulation results of a 2MW WTG - BESS system were shown and experimental waveforms from

scaled down prototype were presented. This paper provided detailed analysis of the converter, along with extensive simulation results. An improved low voltage ride through (LVRT) technique was also proposed for the WTG system that needed only minor modifications in the topology. Overall, the proposed topologies resulted in smaller size and weight along with good quality power delivery that can be achieved at a competitive cost.

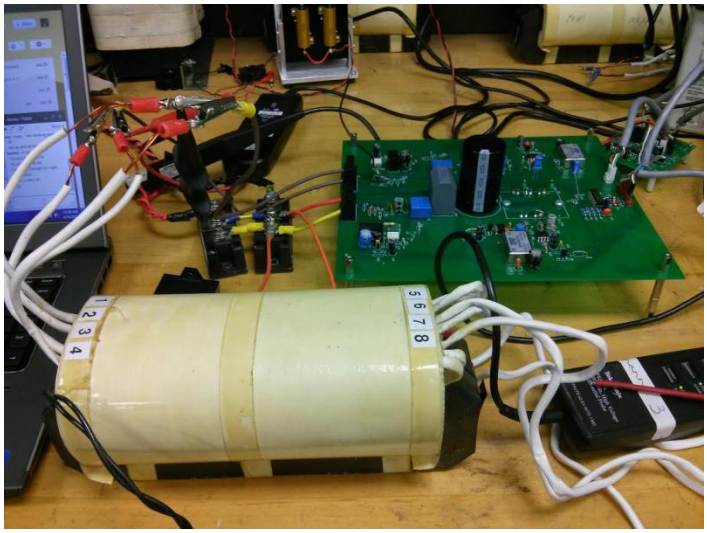

Figure 5-24: Experimental set-up, showing the 600 Hz MF transformer and AC-AC converter

6. MEDIUM AND HIGH FREQUENCY TRANSFORMER DESIGN AND SYSTEM ANALYSIS

6.1. Design of Higher Frequency Transformers for High Power Applications

As explained in the previous sections, the medium frequency (MF) or high frequency (HF) transformer forms one of the most important components of the proposed topologies. This section explains the constructional procedure of transformers in general and later specific to MF transformer design. This section also compares the design of a 1600 VA MF transformer for 60 Hz and 600 Hz operating frequencies. It also shows the comparison in terms of size, efficiency and cost. This can be extended to higher power transformers as well.

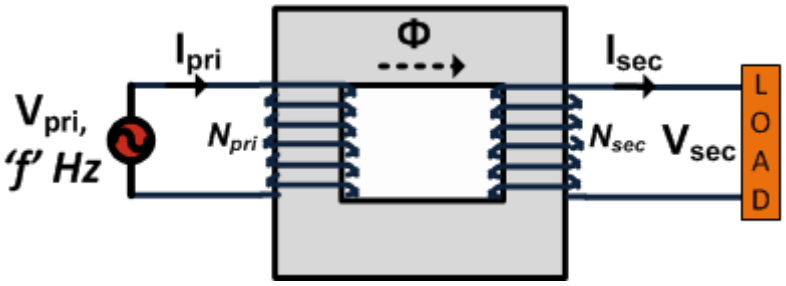

Figure 6-1: Defining terms in a transformer design

To design a transformer that is powered by a sine or square wave, the following information is necessary: the incoming line voltage (V_{pri}), the operating frequency (f), the secondary voltage (V_{sec}), the currents (I_{pri}, I_{sec}), the permissible temperature rise (T_{rise}), the target total loss (P_t), the physical size, and the cost limitations (see Figure 6-1). Once these factors are known, the design starts with the primary voltage and

frequency. The total processed power in watts (or VA) of each secondary winding is found by multiplying the voltage by the current of each coil. These are added together to get the total power the transformer processes to the load. Then the calculated/expected transformer losses added to give a total power drawn from the source. The losses are primarily from the transformer core (hysteresis and eddy current losses) as well as from the windings (I^2R losses). Since these losses are dissipated as heat the permissible temperature rise must be calculated correctly. The next step is to determine the transformer core material. The most common cores are silicon steel, amorphous, ferrite and powdered iron. Depending on the material composition and structure, the *B-H* curves and the loss characteristics with respect to flux density and frequency can vary, which are generally specified by the material manufacturer. Next step is to select the type of core by what efficiency is stated, and the value of losses to the user. Once the material is selected, the peak flux density is decided next for that material. For a transformer designed for use with a sine/square wave, the universal voltage formula is given by (6.1), considering primary side.

$$V_{pri} = \sqrt{2} \cdot \pi \cdot f \cdot N_{pri} \cdot \varphi_m = 4.44 \cdot f \cdot N_{pri} \cdot B_m \cdot A \tag{6.1}$$

where A is the cross-sectional area of the core, B_m is the peak magnetic flux density (in T). If l is the net length of the core (in m), f is the operating frequency, Φ_m is the magnetic flux, H is the magnetic field (in A/m), μ_r is the relative permeability, μ_o is the permeability of free space ($4.\pi.10^{-7}$), R is the reluctance, N is the number of turns, I_m is the magnetizing current and L is the magnetizing inductance. Other primary equations governing the transformer design are given by (6.2), (6.3), (6.4), (6.5) and (6.6).

$$\frac{N_{pri}}{N_{sec}} = \frac{V_{pri}}{V_{sec}} = \frac{I_{sec}}{I_{pri}} \tag{6.2}$$

$$\varphi_{net} = \frac{M.M.F_{net}}{R} = \frac{(N_{pri} \cdot I_{pri} - N_{sec} \cdot I_{sec})}{R} \tag{6.3}$$

$$H_{net} = \frac{(N_{pri} \cdot I_{pri} - N_{sec} \cdot I_{sec})}{l} = \frac{N \cdot I_m}{l} \tag{6.4}$$

$$R = \frac{l}{\mu_r \cdot \mu_o \cdot A} \tag{6.5}$$

$$L = \frac{N_{pri} \cdot B \cdot A}{I_{pri}} = \frac{\mu_r \cdot \mu_o \cdot A \cdot N_{pri}^2}{l} \tag{6.6}$$

From these equations, the transformer can be designed by following the below procedure [84-86]:

1. Select an operating frequency for the transformer (say 60 Hz, 600 Hz, etc.) depending on the application and specifications

2. Based on the power curves available for different cores, select the particular type of core material to use for the particular frequency. In order to use for applications such as ASDs, WTGs, etc., for frequencies less than 1 kHz silicon steel or amorphous core can be used, but would require other core materials such as ferrite in order to use at much higher frequencies.

3. Once the core is decided, using the voltage, current and peak flux density specifications, eqn. (6.1) is used to determine the minimum '*A*N*' value.

4. After that, a minimum value of magnetizing inductance, L is calculated for the selected frequency so that the magnetizing current, I_m (this is approximately "$I_{pri} - I_{sec}$" for a 1:1 transformer) is small, say less than 5 % of the transformer current rating.

5. With the expected L value, choose an 'N_{pri}' value. Then this value is used in (6.4) to arrive at a minimum length of the core.

6. Using the inequalities arrived at using equations (6.1), (6.4) and (6.6), the dimensions of the transformer and number of turns can be decided. Another constraint in this can be given by the net window area of the transformer core, which is determined by the total area of the conductors carrying the current. This factor also plays an important role in the decision of the total core length, l.

7. With the arrived dimensions, the total power loss, hence the efficiency of the transformer can be calculated. If it is either lower or higher than expected, the design steps have to be repeated with different values for number of turns, magnetizing current, etc. until the final specification is met.

6.2. Magnetization Characteristics of Different Transformer Core Materials

Substituting the specification values into the above equations, it is possible to decide the primary number of turns, flux density, area, etc. Depending upon the core material, the performance and design vary significantly. For the silicon steel B-H curve shown in Figure 6-2, the saturation flux density is above 1.5 T and the saturation does not happen until high magnetic fields of about 800 A/m. Due to this reason, the length of

the transformer need not be very high [87]. But due to relatively lower permeability and higher losses, the cross sectional area or the number of turns has to be higher.

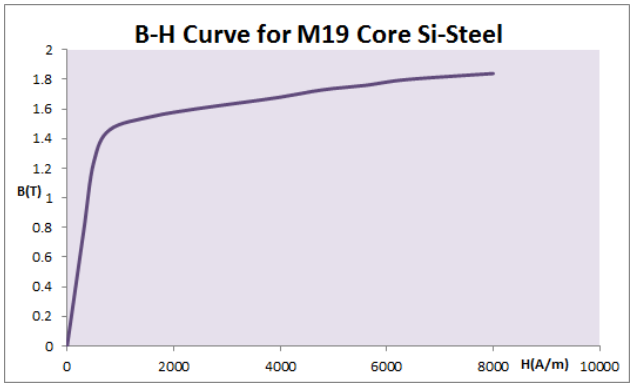

Figure 6-2: B-H Curve for M19 silicon steel core [87]

For an amorphous core B-H curve shown in Figure 6-3, the permeability is higher compared to a silicon steel core, but saturation occurs at much lower magnetic fields itself [88]. So in order to design an amorphous core transformer, either low number of turns needs to be used or the length of the core needs to be more. So this type of core does not provide a big advantage in terms of size for medium frequencies, but the power loss is much lower compared to silicon steel core.

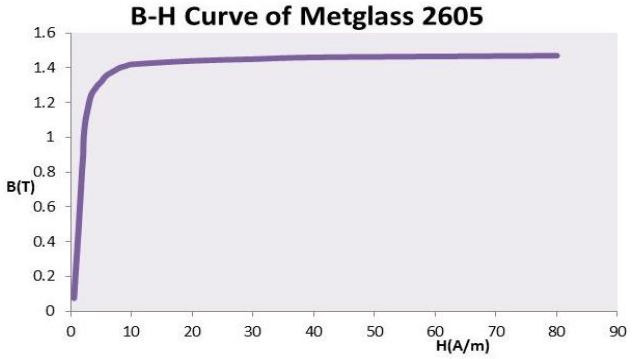

Figure 6-3: B-H curve of an amorphous core [88]

For a 3C85-material ferrite core B-H curve [89] shown in Figure 6-4, the permeability is even higher compared to an amorphous core, but then again saturation occurs at lower magnetic fields compared to M19 material. Moreover the saturating magnetic flux density value is also lower. But this core material has much lower losses compare to silicon steel or amorphous core materials, so that they can be used for high operating frequencies. The cost of such core materials is also higher. Ferrite cores are suitable for operating frequencies higher than 6 – 10 kHz due to low loss characteristics.

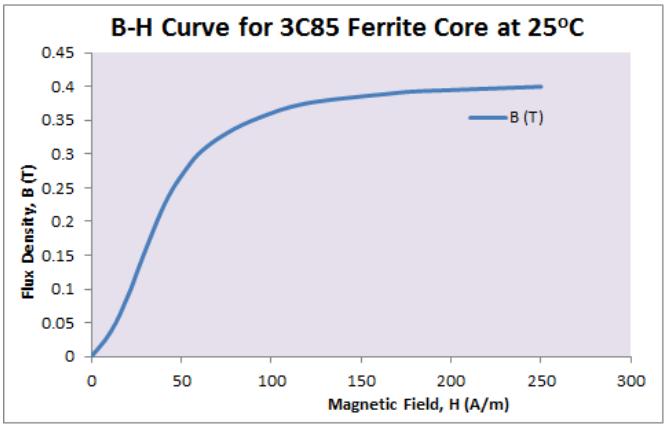

Figure 6-4: B-H curve for ferrite core – 3C85 [89]

6.3. Analysis of Core Losses at Different Voltage Waveforms

From Figure 6-5 and Figure 6-6, it is evident that the core loss per pound is almost 10 times higher in an M19 (or most other conventional electrical Si steel core) compared to an amorphous core, such as Metglass 2605 material. This way, even if it turns out that there is no major difference in the size of the transformer while using an amorphous core at MF, the core losses can be significantly lower. This reduces the cooling requirement for the transformer as well.

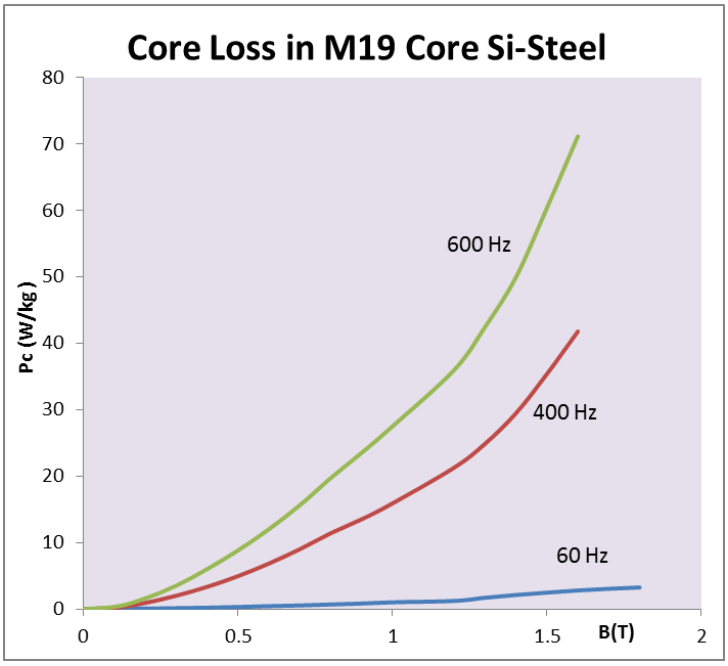

Figure 6-5: Core Loss curve for M19 electrical steel

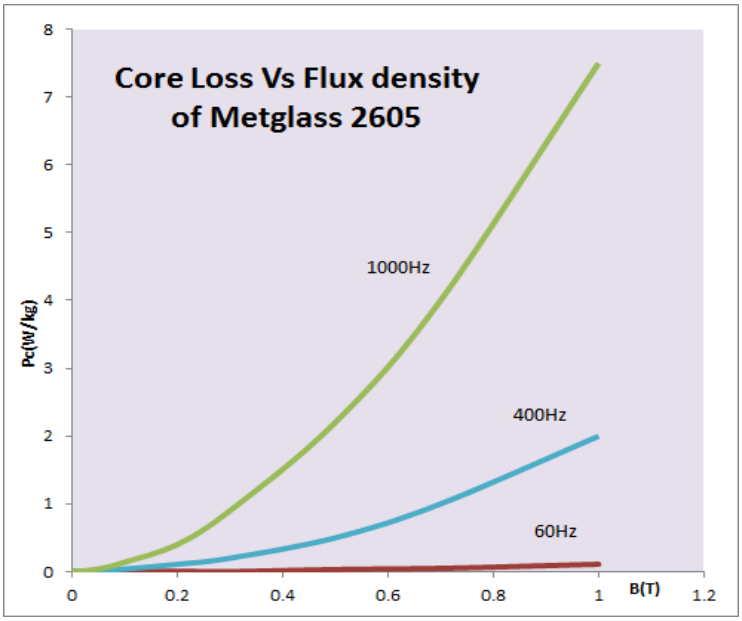

Figure 6-6: Core Loss curve for Metglass-2605 amorphous core

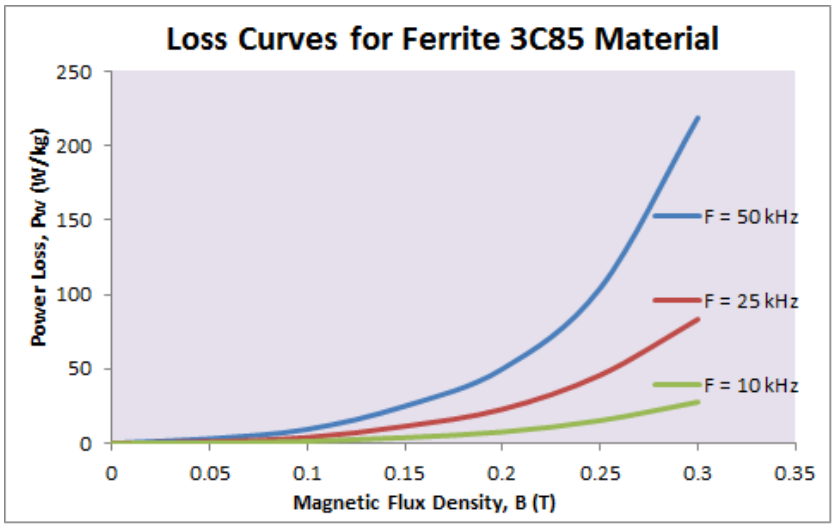

Figure 6-7: Core loss characteristics for a Ferrite 3C85-material

Figure 6-7 shows the example of core loss characteristics of ferrite 3C85-material [89]. It can be seen that the core loss per kg at a magnetic flux density of 0.3 T at 10 kHz is nearly *25 W/kg*, whereas an amorphous Metglass core, if characteristics shown in Figure 6-6 are extended, has a core loss per kg around *80 W/kg* at 10 kHz itself for 0.3 T magnetic flux density. This shows that even if operated at frequencies higher than the MF, a transformer designed using ferrite core will have much lower losses compared to a Si steel or an amorphous core material. However since the cost of the material is very high, ferrite cores are not used unless the form factor or the efficiency requirement is very tight. There are even better grades of ferrite materials commercially available.

6.4. Example Design of Transformers for the Proposed Topologies

This sub-section deals with an example design of a MF transformer that was eventually constructed and experimented for the different applications proposed in the earlier sections. As discussed earlier, the design [90] was for a 1.6 kVA transformer [91]

with a peak voltage rating of around 130 V. First, a 60 Hz transformer reference was designed, focusing on the least size aspect without saturating the core. Considering the M-19 Si steel core (with magnetic and loss characteristics as in Figure 6-2 and Figure 6-5, respectively), the maximum flux density was limited to 1.25 T (which implies magnetic field, $H < 500$ A/m) to avoid saturation. From (6.1), the relation between A and N can be determined as in (6.7).

$$A \cdot N \geq 0.43 \tag{6.7}$$

To reduce the magnetizing current to less than 0.5 A (< 5 % of rated current), using (6.4), the relation between N and l can be given by (6.8).

$$\frac{N}{l} \leq 1000 \tag{6.8}$$

Assuming AWG-14 wires are used with a current rating of at least 15 A with an area of cross section of $2*10^{(-6)}$ m^2, and a winding fill factor of 0.4 [90], another relation between N and l can be arrived at using the equation (6.9) (assuming the window area, A_w for this design as a function of core length l is given by $A_w = l^2/18$).

$$\frac{l^2}{18} \geq \frac{2*10^{(-6)}*2*N}{0.4} \rightarrow \frac{l^2}{N} \geq 0.00018 \tag{6.9}$$

One more inequality can be derived using (6.6). Considering that the maximum magnetizing current can be 0.5 A at 130 V maximum excitation and 60 Hz frequency, and assuming the maximum permeability of M-19 core in the region of interest is 0.0025, the inductance must be greater than 0.7 H. Then eqn. (6.6) leads to (6.10).

$$\frac{A \cdot N^2}{l} \geq 280 \tag{6.10}$$

Solving the inequalities in (6.7), (6.8), (6.9) and (6.10), the below values given by (6.11) were arrived at for the 60 Hz transformer:

$$N_{60} = 250; \quad l_{60} = 0.62\, m; \quad A_{60} \geq 0.003\, m^2 \tag{6.11}$$

Following similar arguments, a 600 Hz medium frequency (MF) transformer was also designed for the same specifications with the same electrical steel core and targeting same efficiency. The minor variations in the design are that the maximum flux density for the 600 Hz transformer was limited to nearly 0.55 T even at 130 V. So the maximum permeability for the range of interest is around 0.0035 T.m/A. Also, the fill factor in this case was reduced to 0.3, due to the higher operating frequency. Finally, the below design parameters were arrived at for the 600 Hz transformer, given by (6.12):

$$N_{600} = 140; \quad l_{600} = 0.54\, m; \quad A_{600} \geq 0.0012\, m^2 \tag{6.12}$$

From (6.11) and (6.12), it can be clearly seen that the overall core volume of the MF transformer was reduced to almost 35 % of the 60 Hz core. These design calculations can be extended to higher power transformers too, with slight changes in peak flux densities and fill factors. Due to almost 2.5 times larger cross-sectional area and more than 1.6 times increase in the number of turns of the 60 Hz transformer over the 600 Hz transformer design, the total copper length required by the 60 Hz transformer is almost 4 times that of the 600 Hz design, which increases the conduction losses. Using the core loss curves of M19 core from Figure 6-5, it can be seen that the core loss per kg of the 60 Hz design at 1.3 T is almost 4.5 times that of the 600 Hz design at 0.55 T. But

considering that the total weight of the 60 Hz core is at least 3 times that of the 600 Hz transformer, the net core loss is only increased by 50 %. Considering the conduction losses, the total transformer losses in the 60 Hz design as well as 600 Hz design are almost similar.

A third transformer was designed using the amorphous Metglass core material whose characteristics are shown in Figure 6-3 and Figure 6-6. Based on the B-H curve, the maximum flux density was limited to 1.1 T to avoid core saturation (at a magnetic field of close to 2.4 A/m and maximum permeability of 0.45 T.m/A). As discussed before, due to the low magnetic field for saturation (3 A/m) and at 600 Hz, the design parameters resulted in almost the same dimensions of the 600 Hz transformer derived earlier using the M19 core, but at a slightly higher number of turns; N = 180. From the loss characteristics of the Metglass 2605 core (see Figure 6-6), for the same dimensions, the total core loss came down to *~20 %* of that with the 600 Hz design using M19 core.

As stated earlier, to quantify the lower core loss of Metglass 2605 material compared to M19 core, another transformer design was constructed for a HF of 6 kHz using the same material, but the maximum flux density was limited to 0.5 T to limit the core losses. For this design, the transformer size could be reduced significantly. Due to higher operating frequency, the winding fill factor was considered to be 0.2. Using arguments similar to the inequalities in (6.7) to (6.11), the design outcome can be summarized in (6.13). From the loss characteristics of the Metglass 2605 core (see Figure 6-6), the total core loss was 14 W for this design, which is higher than the 600 Hz design with the same material, but only $(1/3)^{rd}$ of the core losses compared to 600 Hz

M19 core based design. The big improvement though was on the core volume, which became almost $(1/8)^{th}$ the size of the previously designed 600 Hz MF transformer with the same amorphous core.

$$N_{6k} = 60; \quad l_{6k} = 20\ cm; \quad A_{6k} = 2\ X\ 2 = 4\ cm^2 \tag{6.13}$$

As seen from Figure 6-4 and Figure 6-7, a ferrite core has only 35 % to 40 % loss per weight compared to a Metglass 2605 core (see Figure 6-6), when operated at a maximum flux density of 0.3 T. To complete the study of different transformer designs, a 6 kHz HF transformer was designed using the ferrite 3C85 material at a maximum flux density of 0.3 T. Owing to the lower peak permeability of the ferrite core and lower saturation flux density, the core dimension (see (6.13)) could be made to be similar, but at a slightly higher number of turns (N = 80). With this, it was possible to reduce the core losses to nearly 5 W at an almost same dimension as the previous design, leading to a 99.7 % efficiency at a power density of almost 4 kW/kg for the transformer overall. From this, it is evident that it is possible to achieve a very high transformer power density as well as high transformer efficiency using ferrite cores. But operating the power electronics converters at such frequencies at high power have much worse efficiency implications, which is explained later in this section.

All the above described designs were then modeled and simulated using Ansys Maxwell 2-D tool to validate the design, which are explained in the subsequent sub-sections.

6.5. Maxwell Simulations of Different Transformer Designs

Using the above analysis, several Maxwell simulations were performed considering a 120 V, 1.6 kVA prototype at certain different combinations of transformer core frequencies (60 Hz, 600 Hz and 6 kHz) and materials (M19 - silicon steel, Metglass - 2605 amorphous and 3C85 - ferrite).

6.5.1. M19 Silicon Steel Core with 600 Hz Base Operating Frequency

Figure 6-8 shows the model of a 600 Hz M19 silicon steel core that was also used for the experiments in the previous sections. For reduced losses at 600 Hz, the core peak flux density at the maximum input voltage (130 V) was selected to be 0.55 T. Figure 6-8 shows the maximum flux density condition under 600 Hz sinusoidal excitation. The total size of the transformer was close to *0.7 L* (56 cm X 2.5 cm X 5 cm). The total core weight was close to 5.3 kg, which contributed to nearly 37 W of core loss at 1.6 kVA.

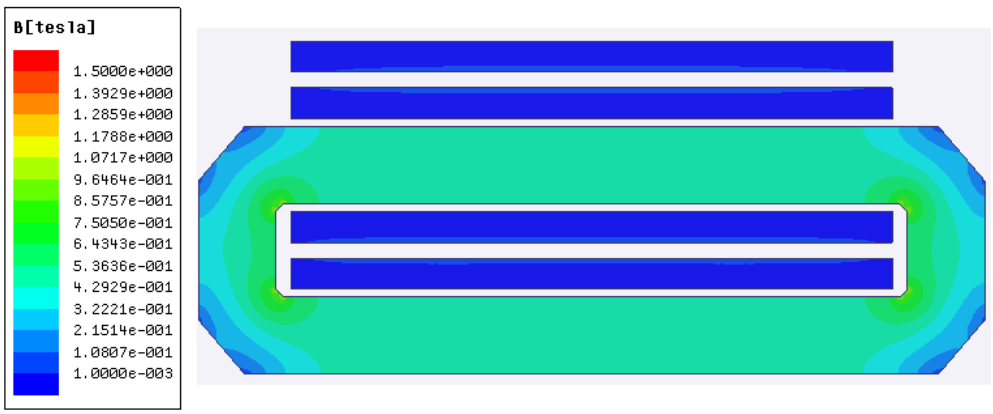

Figure 6-8: Peak flux density condition under 600 Hz MF sine wave excitation

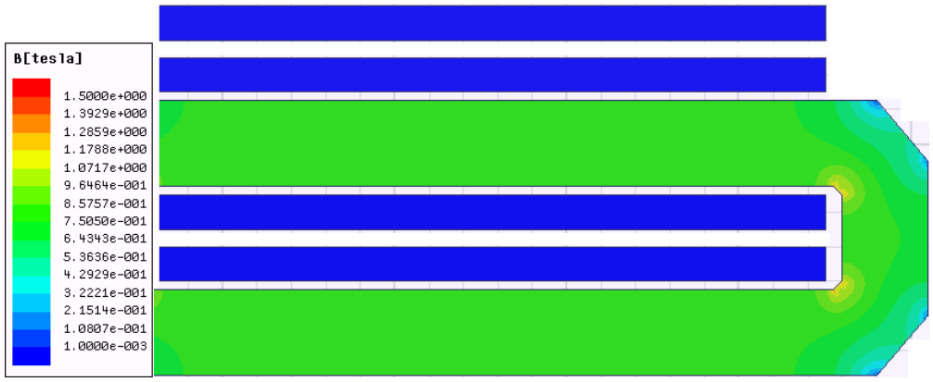

Figure 6-9: Peak flux density condition under (60 Hz sine X 600 Hz square) wave MF excitation

Figure 6-9 shows the flux density distribution with 'flipped sine' wave, i.e. 60 Hz sine multiplied by 600 Hz square. The transformer was able to operate without saturation, at lower losses. But it can be seen that the peak flux density increases in this case. At the same time, the calculations and Maxwell results revealed that the core losses with the 'flipped sine' wave was about 7 % lower than with a 600 Hz sinusoidal excitation due to the lower flux density per major frequency component (note that the 'flipped sine' wave has reduced magnitude of 540 Hz and 660 Hz components and there is no 600 Hz component).

6.5.2. M19 Silicon Steel Core with 60 Hz Base Operating Frequency

Figure 6-10 shows the design of a 60 Hz transformer with the same M19 silicon steel core to compare the size and loss between the 60 Hz and 600 Hz designs. Peak flux density was chosen to be around 1.2 T. The total size of the transformer was close to *1.9 L* (64 cm X 4 cm X 7.5 cm). The total core weight was close to 14.8 kg, which contributed to nearly 25 W of core loss at 1.6 kVA. Figure 6-11 shows the size comparison between the 60 Hz transformer and 600 Hz transformer constructed out of

M19 Si steel core for the same core losses. It can be seen that the size got reduced to nearly 35 % using the proposed 600 Hz MF design instead of 60 Hz.

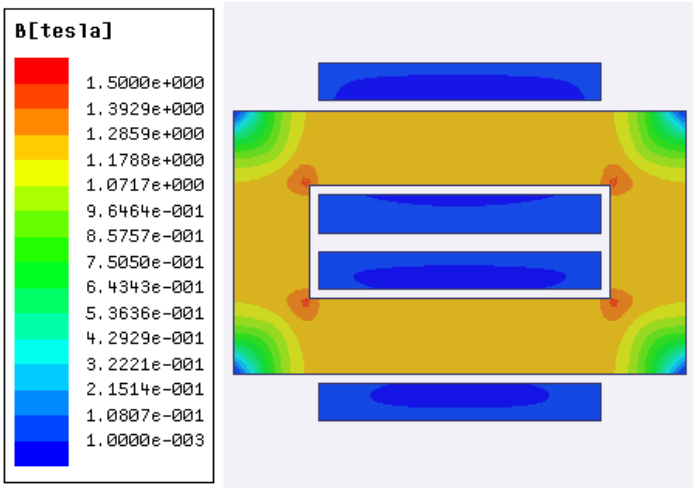

Figure 6-10: 60 Hz Transformer design with M19 core transformer

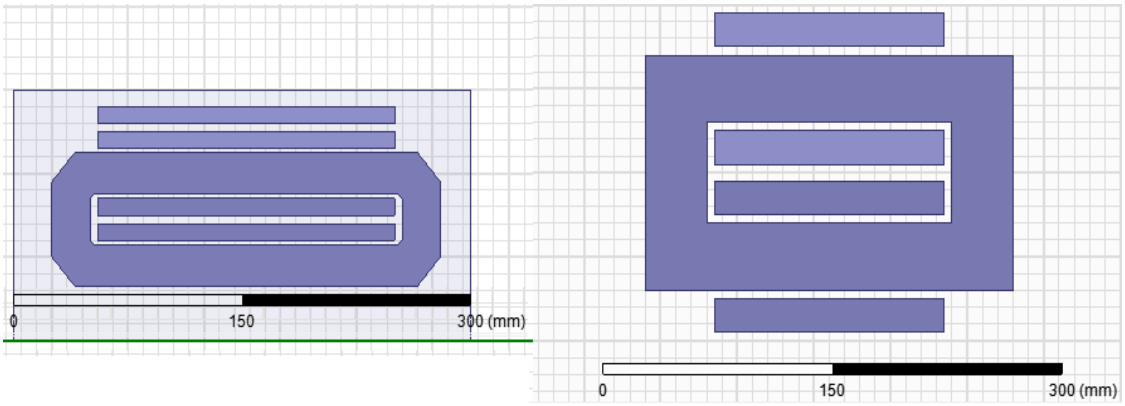

Figure 6-11: Results from a 600 Hz design (0.67 L core volume - 54 cm X 2.5 cm X 5 cm) Vs 60 Hz design (1.86 L core volume - 62 cm X 4 cm X 7.5 cm) ~3 times power density

6.5.3. Metglass 2605 Core with 600 Hz and 6 kHz Base Operating Frequencies

Figure 6-12 shows the design of a 600 Hz *Metglass - 2605* amorphous core to compare with the characteristics of the silicon steel core. The core peak flux density at the maximum input voltage was selected to be 1 T. Figure 6-12 shows the flux density

distribution at 120 V excitation. The total size of the transformer was similar to that of the 600 Hz transformer with M-19 core *0.7 L* (56 cm X 2.5 cm X 5 cm). The total core weight was close to 5 kg, which contributed to nearly 8 W of core loss at 1.6 kVA.

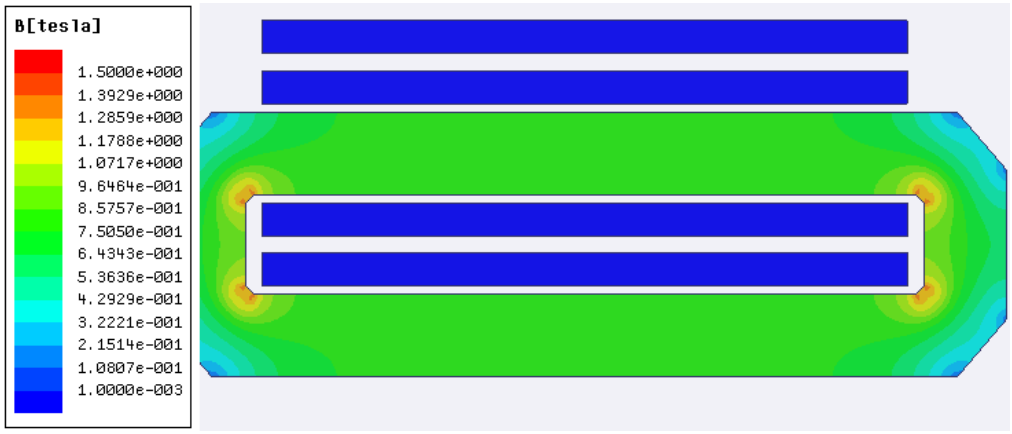

Figure 6-12: Metglass-2605SA1 core based 600 Transformer (56 cm X 2.5 cm X 5 cm) – same size as with M19 Si steel transformer

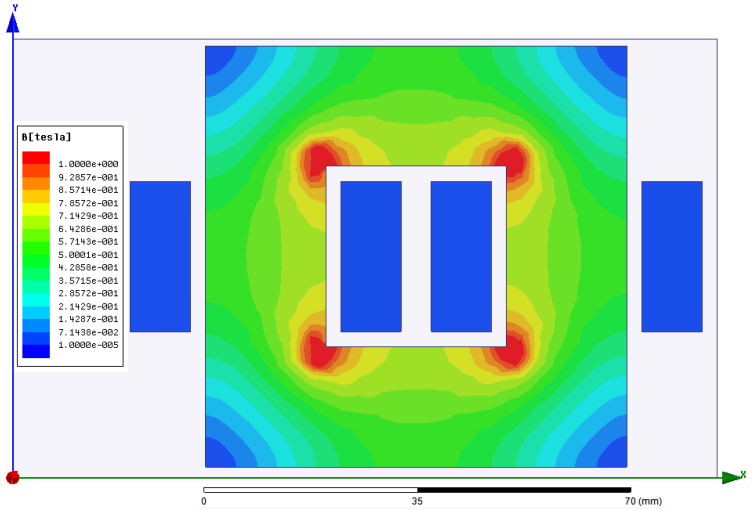

Figure 6-13: Amorphous Metglass-2605 Core based 6 kHz transformer design (*20 cm X 2 cm X 2 cm*)

Figure 6-13 shows the design of a *Metglass2605* amorphous core based transformer, operating at 6 kHz. The core peak flux density at the maximum input

voltage was designed to be 0.55 T. Figure 6-13 shows the maximum flux density condition. The total size of the transformer was *0.08 L* (20 cm X 2 cm X 2 cm). The total core weight was close to 0.6 kg, which led to nearly 14 W of core loss at 1.6 kVA.

6.5.4. Ferrite 3C85 Core with 6 kHz Base Operating Frequency

Figure 6-14 shows the alternative 6 kHz transformer design using ferrite 3C85 ferrite core based transformer. The core peak flux density at the maximum input voltage was designed to be 0.3 T. Figure 6-14 shows the maximum flux density condition. The total size of the transformer came out to be the same, as discussed before, at *0.08 L* (20 cm X 2 cm X 2 cm), but the number of turns was increased to 80 compared to 60 in the previous design (6 kHz with amorphous core). The total core weight was close to 0.4 kg, which contributed to nearly 5 W of core loss at 1.6 kVA.

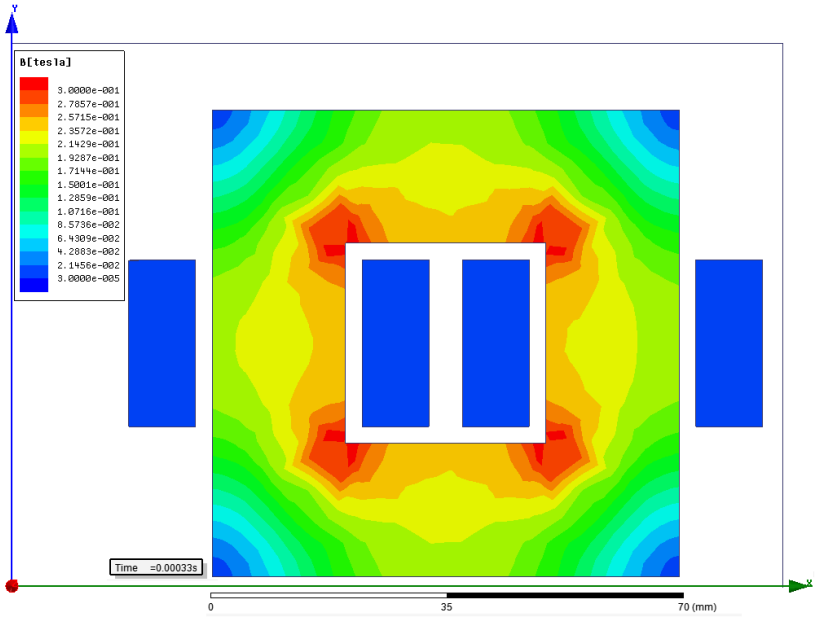

Figure 6-14: Ferrite 3C85 Core based 6 kHz transformer design (*20 cm X 2 cm X 2 cm*)

6.6. Inference and Conclusion

The previous sub-sections discussed the medium frequency (MF) and high frequency (HF) transformer designs and analysis in detail and simulated the different designs using Ansys Maxwell software. It could be seen that though the MF transformer core loss per kg increases significantly while using Si steel core, the total losses of the transformer can be made to be almost equal to the line frequency design due to the reduction in the size. Use of amorphous core can significantly reduce the losses even at MF design. But for operating frequencies between 2 kHz and 5 kHz, the amorphous core can cause significant audible noise and beyond 5 kHz, the core loss of the amorphous core itself will become very high, making the core temperature rise also to intolerable limits. Beyond 5 kHz, ferrite cores seem to be very attractive due to their low loss characteristics and almost constant permeability over the entire range of operation. But then the converter losses become higher due to higher switching frequencies.

Table 6-1 summarizes the results and observations from the design and simulations of the different transformers. It can be seen that using a 600 Hz MF design with M19 Si steel core can bring the size and the cost of a transformer by one-third compared to a 60 Hz design with the same material, at the same net transformer losses. If a Metglass core is used, the size and efficiency of a MF (600 Hz) design can be brought down to nearly one-third of a 60 Hz transformer design with silicon steel core, at a similar cost (even including converter costs).

Table 6-1 assumes from Table 1-1 that the normalized cost of winding is almost 40 % the cost of the core for a practical 60 Hz transformer design [15]. The cost of the

60 Hz core using M19 (silicon steel) is considered to be 1 p.u. and the other costs are shown with respect to that. It is assumed that the cost per kg of Metglass 2605 core is almost 3 times that of M19 core and cost per unit volume of ferrite core is almost twice that of Metglass 2605 core. Table 6-1 also shows the comparison of 6 kHz operating frequency based design with the 600 Hz and 60 Hz designs. It can be seen that a HF transformer constructed with ferrite 3C85 core features to be the best in terms of cost, efficiency as well as power density, even while operating at 6 kHz. But it should be noted that for a high power converter system over several hundreds of kilowatts, operating with hard switching at 6 kHz significantly increases the switching losses, nullifying the effects of the efficiency, cost and size gains from the usage of ferrite core.

Table 6-1: Summary of transformer design parameters and values discussed earlier in this section

Transformer Design	M19 Core 60 Hz	M19 Core 600 Hz	Metglass 600 Hz	Metglass - 2605 6 kHz	Ferrite - 3C85 6 kHz
Operating Frequency (Hz)	60	600	600	6000	6000
Max. Flux Density (T)	1.25	0.55	1.1	0.55	0.3
Core Dimensions (cm)	62 X 4 X 7.5	54 X 5 X 2.5	60 X 4.5 X 2.5	20 X 2 X 2	20 X 2 X 2
Number of turns	250	140	180	80	80
Core Volume (L)	1.9	0.67	0.62	0.08	0.08
Core Weight (kg)	14.8	5.3	5.0	0.6	**0.4**
Core Loss/Mass (W/kg)	1.7	7.5	1.8	24	12
Net Core Loss (W)	25	40	9	14	5
Winding Loss (W)	20	6	8	3	3
Total Transformer Loss (W)	45	46	**17**	17	8
Efficiency at 1.6 kVA (%)	97.3	97.2	99.0	99.0	**99.5**
Cost of Core (p.u.)	1.0	0.35	1.0	0.15	0.3
Cost of Winding (p.u.)	0.4	0.13	0.2	0.1	0.1
Total Cost (p.u.)	1.4	0.48	1.2	0.25	**0.4**

From Figure 6-15, it can be seen that if a 600 Hz Si steel core based MF transformer (designed similar as the one in Figure 6-9) is used in the proposed topology in Figure 2-4, the overall converter efficiency comes close to 95 %, the main loss contributor being the MF transformer itself. The next largest loss contributions are due to the primary side AC-AC converter switching losses as well as the boost PFC losses. For calculations, *FZ400R33KL2C* IGBTs and *DD400S33KL2C* diodes specified in [92] and [62], respectively were chosen along with some other reasonable assumptions for a 1000 H.P. system, that can be used in applications such as data centers, ASDs, etc.

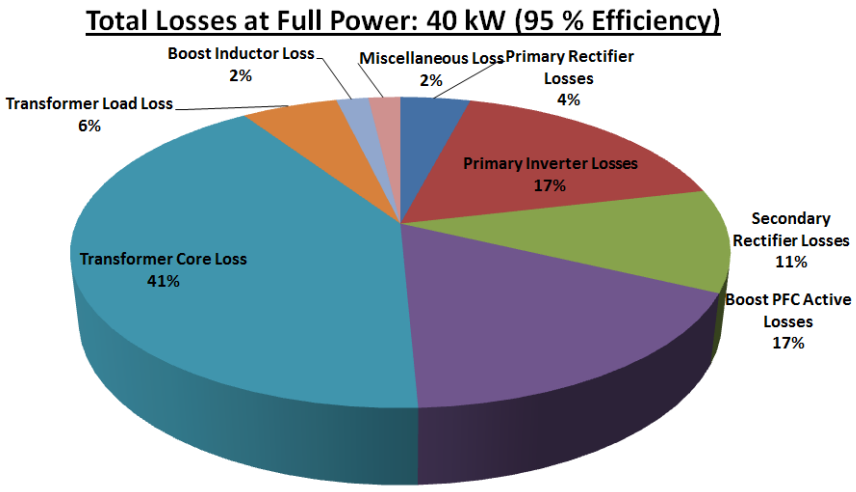

Figure 6-15: System level loss distribution while operating the proposed topology in Figure 2-4 with 600 Hz M19 Si steel core based transformer

Now, when the same proposed topology as in Figure 2-4 is operated along with Metglass 2605 core based 600 Hz transformer, and using the same remaining converter system, the total efficiency improves significantly to almost 96.5 % as seen in Figure 6-16, at an almost 55 % reduction in total size compared to a line frequency transformer based system in Figure 3-1 or Figure 4-1. This shows that an amorphous core based MF

transformer is a very good alternative to a Si steel core based line frequency transformer. Only the cost of the system is a little higher compared to the Si steel core, but this can be offset to an extent by the lower cooling requirement in the transformer.

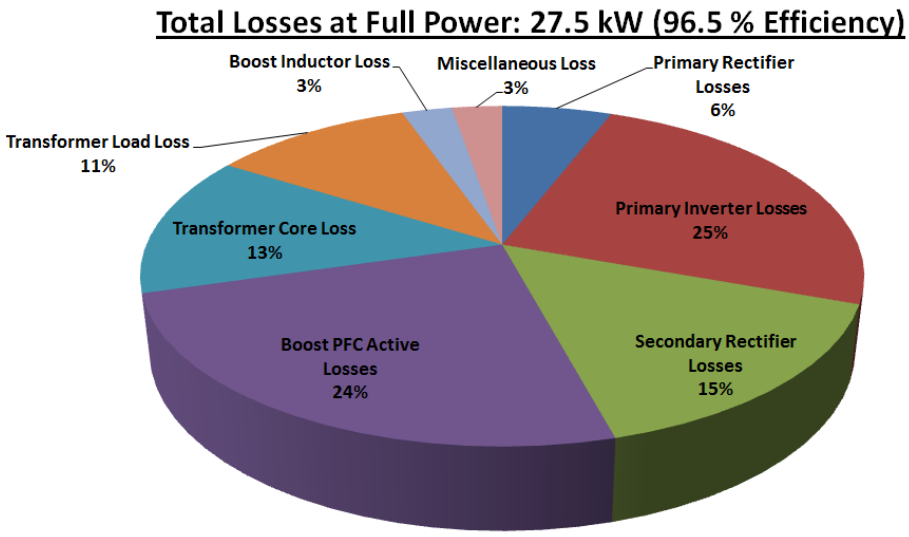

Figure 6-16: System level loss distribution while operating the proposed topology in Figure 2-4 with 600 Hz Metglass 2605 core based transformer

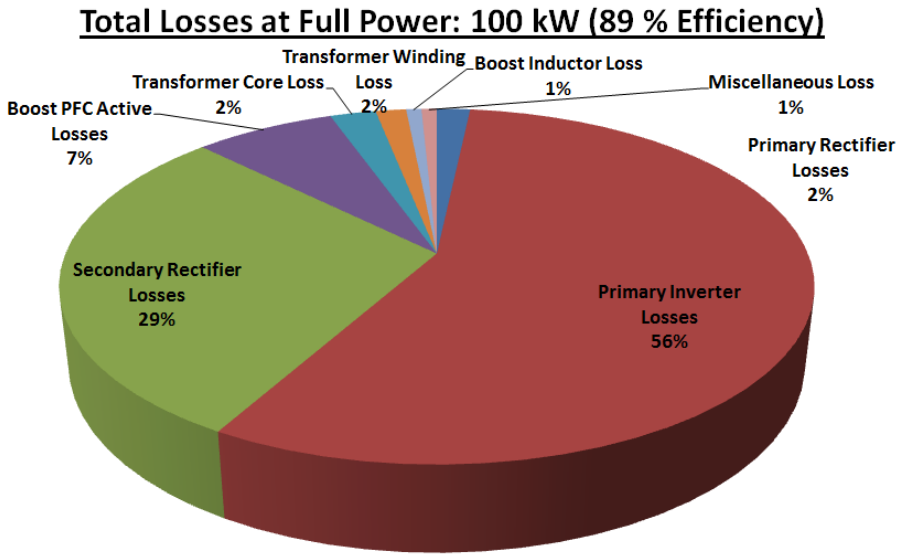

Figure 6-17: System level loss distribution while operating the proposed topology in Figure 2-4 with 6 kHz Metglass 2605 core based transformer with no soft-switching

In order to have a fair comparison on the total losses in the system for even higher transformer core frequencies, a similar analysis was performed for a 6 kHz transformer designed using both amorphous material (Metglass 2605) and ferrite material (3C85). First, the analysis assumes that no soft-switching is involved in this application. Since the loss contribution at 6 kHz by both Metglass as well as ferrite core is low (compared to the remaining system) owing to the small core size and loss characteristics, only the loss distribution of amorphous core transformer based topology (in Figure 2-4) is shown in Figure 6-17. In the same system, if soft-switching is performed to lower the switching losses on the AC-AC converter and the secondary side diode rectifier, an overall efficiency of 96.5 % as in the previous case (see Figure 6-16) can be attained only if soft-switching is able to reduce net switching losses to *one-fifth*, which is difficult to achieve in a high power system, especially with pulsating DC bus.

Overall for high power isolated converters, a Si steel core - MF transformer based system fares well in terms of cost and size compared to a 60 Hz design, where as an amorphous core - MF transformer based system fares well in terms of efficiency and size compared to a conventional 60 Hz design (with Si steel core), while a ferrite core can be useful if appropriate soft-switching techniques are identified. Finally the relative size occupied by various components in the above mentioned transformer as well as converter designs related to the proposed topology in Figure 2-4 are briefed in Figure 6-18 (considering the overall system size of conventional 60 Hz transformer based approach is 1 p.u.). While the 60 Hz and 1200 Hz core frequency based designs have been assumed to operate with hard-switching, the ferrite core (3C85) based system is

assumed to operate with soft-switching as discussed previously. The numbers obtained have been derived from Figure 1-4 and [87, 93]. Also, it is possible to achieve 5 to 6 times higher power density using a 1200 Hz MF transformer compared to a 60 Hz transformer, which is almost at the upper limit of frequency in the MF range since operating frequencies between 1.5 kHz and 5 kHz can significantly increase the audible noise while using amorphous or Si steel cores.

It can be seen from Figure 6-18 that as we increase the operating frequency of the transformer, the transformer size does reduce considerably. But since the remaining components of the system also form around 30 to 40 % of most conventional high power systems that employs the line frequency transformer, this portion cannot be reduced much owing to design constraints. Thus, any design involving transformer frequencies beyond 1.2 to 1.5 kHz may not result in significant reduction in the power-to-volume density of the overall system. So in conclusion, to achieve a reasonably higher system power density (atleast twice) compared to a line frequency transformer based conventional approach at a comparable efficiency, a Si steel or an amorphous core based MF transformer itself can be a handful, which also involves lower operating/constructional complexity compared to a HF transformer based system at high power. This makes it easier to employ standard semiconductor devices itself since the switching frequency is not very high even at such high power scales. But for applications less than 200 kW, HF transformers can be put to better use to improve the power density.

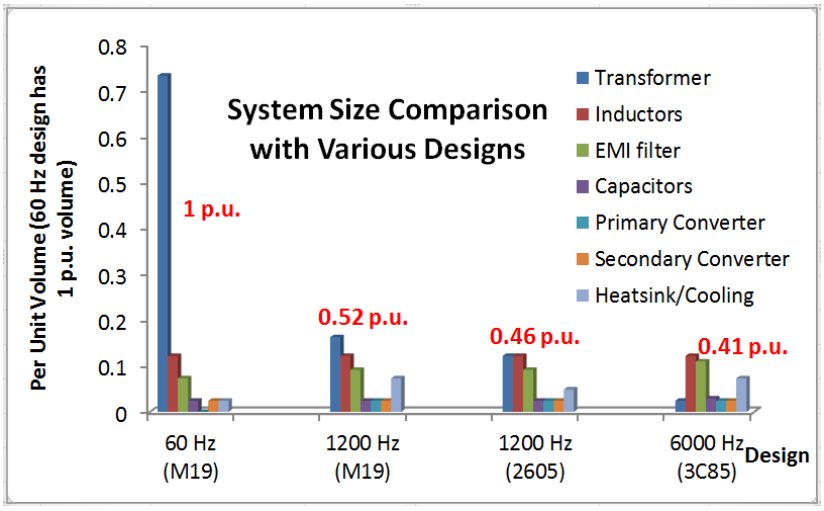

Figure 6-18: Component size distribution for different transformer designs for the same proposed topology in Figure 2-4 (overall system size of 60 Hz transformer based design is 1 p.u.)

From Table 1-1 and Table 6-1, the size seems to be following a trend. If 'n' is the ratio of the MF (say 600 Hz) to the line frequency (say 60 Hz), in order to achieve the same net efficiency (or losses), the improvement in power density possible is nearly '$\sqrt{n}$'. From Table 1-1, $n\sim=16$ for the 1000 Hz design and the power density could be increased to nearly *4* times. Here from Table 6-1, $n=10$ for the 600 Hz design and the power density could be improved to nearly *3* times. Though this trend may not continue for frequencies beyond 1.5 kHz when the Si steel core becomes very lossy, this relation provides a reasonable starting point for a MF transformer design to optimize further.

7. SUMMARY

7.1. Conclusion

This dissertation first introduced various utility interface applications and the concepts of power density in converters. Then the section discussed the mathematical modeling of power converters at various modulation schemes along with some of the basic ways of implementing the models using AC-AC converters.

The subsequent section proposed an isolated 3-phase AC-DC converter using MF or HF transformers, which can be used for various applications such as in telecom power supplies, battery charging, etc. The design and control strategy were explained in detail and the concepts were validated through simulations and experiments. Section 3 proposed a simplified multi-pulse diode rectifier concept using MF or HF transformers that replace bulky line frequency transformers from a typical system. The theory and design of the conventional systems were presented followed by the explanation of the proposed approach. Detailed analysis, simulation and experiments were performed for a 12-pulse rectifier configuration, and ways to extend this concept to higher configurations were also discussed.

Section 4 extended some of the concepts proposed in section 2 and applied them to develop topologies for wind turbine generator (WTG) – medium voltage DC (MVDC) interconnection suitable for offshore farms and long-distance transmission line. The section started with the introduction to offshore wind farms and some of the WTG – MVDC converters already proposed in the literature. After explaining the theory and

operation of the proposed topology, simulation results were shown which demonstrated the control mechanism and robustness of the system. The subsequent section introduced the importance of battery energy storage systems (BESS) in modern day grid and discussed some of the power electronic topologies that have been proposed in the literature to interface large BESS systems with the utility grid. Then a MF transformer based approach was proposed for interfacing a large scale BESS system to the utility grid. As an extension, a 3-port scheme for interfacing a WTG system along with a BESS system was also introduced in this section. Detailed simulation and experimental results were shown. Salient features of a large wind farm, such as low voltage ride through (LVRT), fault-handling capacity, etc. were also discussed in detail.

Section 6 concentrated on the design and modeling the MF/HF transformers using ANSYS Maxwell software. Transformers designed at different core frequencies using various materials such as silicon steel, amorphous, ferrite, etc. were evaluated in depth under the criteria of size and losses. Comparison in terms of size and losses in the MF or HF transformers with respect to the line frequency transformer was also shown. The best designs with regards to different parameters of size, cost and efficiency were noted; and a relative component size study was performed for the overall converter.

To conclude, this dissertation proposed several approaches using which it is possible to replace bulky line frequency transformers with medium or high frequency ‘solid-state transformers’ and avoid large DC electrolytic capacitors to improve the power density as well as reduce the cost of typical medium and high power applications such as ASDs, WTGs, etc. It was identified that for such systems, MF transformers

constructed using electrical steel or amorphous cores could significantly reduce the overall system size to almost 40 %, with potential to further improvement in size and efficiency. For such high power applications, though it is possible to opt for an even higher frequency transformer core such as ferrite or nano-crystalline, this may lead to higher switching losses in the power converters and will significantly reduce the 'fill factor' of the windings due to the corona losses beyond certain frequencies, resulting in a lower efficiency at only a meagre improvement in power density. Medium frequency transformers can be very suitable for such situations leading to higher power density, either at a lower cost or higher efficiency.

7.2. Future Work

Various other possibilities arise from this dissertation. A few are listed below:

- Soft-switching techniques that can be employed at even higher switching frequencies in the proposed topologies; also resonant energy conversion can be studied.
- Though the experiments in this dissertation regarding multi-pulse rectifier were on 12-pulse topology, 18-pulse and higher configurations can be constructed and tested on an even larger scale.
- Since only the 600 Hz Si steel transformer was constructed and tested, all the other transformers designed and simulated in the earlier section can also be constructed and tested on laboratory prototypes.
- Nano-crystalline core based transformers can be investigated for higher operating frequencies and in situations where high temperature operation is desired.

REFERENCES

[1] T. Mai;, R. Wiser;, D. Sandor;, G. Brinkman;, G. Heath;, P. Denholm;, D. J. Hostick;, N. Darghouth;, A. Schlosser;, and K. Strzepek;. (Nov. 30, 2014). *"Renewable Electricity Futures Study" (Volume 1 ed.)*. Available: http://www.nrel.gov/docs/fy12osti/52409-1.pdf

[2] H. S. Krishnamoorthy, S. Essakiappan, P. N. Enjeti, R. S. Balog, and S. Ahmed, "A new multilevel converter for megawatt scale solar photovoltaic utility integration," in *Twenty-Seventh Annual IEEE Applied Power Electronics Conference and Exposition (APEC)*, 2012, pp. 1431-1438.

[3] M. Charles. (Nov. 30, 2014). *"California's Energy Storage Mandate: Electricity Advisory Committee Meeting"*. Available: http://energy.gov/sites/prod/files/2014/06/f17/EACJune2014-3Charles.pdf

[4] W. Kramer;, S. Chakraborty;, B. Kroposki;, and H. Thomas;. (Nov. 30, 2014). *"Advanced Power Electronic Interfaces for Distributed Energy Systems"*. Available: http://www.nrel.gov/docs/fy08osti/42672.pdf

[5] ABB. (Nov 30 2014). *"A world in transformation"*. Available: http://www05.abb.com/global/scot/scot271.nsf/veritydisplay/c3791bac5b25bd10c1257ab80037553b/$file/ABB%20SR%20Transformers-121031.pdf

[6] F. Blaabjerg, A. Consoli, J. A. Ferreira, and J. D. Van Wyk, "The future of electronic power processing and conversion," *Industry Applications, IEEE Transactions on,* vol. 41, pp. 3-8, 2005.

[7] R. Burkart and J. W. Kolar, "Component cost models for multi-objective optimizations of switched-mode power converters," in *Energy Conversion Congress and Exposition (ECCE), 2013 IEEE*, 2013, pp. 2139-2146.

[8] A. Rufer, N. Schibli, C. Chabert, and C. Zimmermann, "Configurable front-end converters for multicurrent locomotives operated on 16 2/3 Hz AC and 3 kV DC systems," *Power Electronics, IEEE Transactions on,* vol. 18, pp. 1186-1193, 2003.

[9] Railway-Technical. (Nov. 30, 2014). *"Electric Locomotives"*. Available: http://www.railway-technical.com/elec-loco-bloc.shtml

[10] R. Raju. (Nov. 30, 2014). *"Silicon Carbide: High Voltage, High Frequency Conversion"* [NIST High Megawatt Variable Speed Drive Technology Workshop]. Available: http://www.nist.gov/pml/high_megawatt/upload/Approved-Raju-DoE_NIST_HMW_VSD_GE_raju.pdf

[11] R. M. Burkart and J. W. Kolar, "Comparative evaluation of SiC and Si PV inverter systems based on power density and efficiency as indicators of initial cost and operating revenue," in *Control and Modeling for Power Electronics (COMPEL), 2013 IEEE 14th Workshop on*, 2013, pp. 1-6.

[12] J. W. Kolar; and G. I. Ortiz;. (Nov. 30 2014). *"Solid State Transformer Concepts in Traction and Smart Grid Applications"*. Available: https://www.pes.ee.ethz.ch/uploads/tx_ethpublications/__ECCE_Europe_SST_Tutorial_FINAL_as_corrected___extended_after_ECCE_12_130912.pdf

[13] L. Chun-kit, S. Dutta, B. Seunghun, and S. Bhattacharya, "Design considerations of high voltage and high frequency three phase transformer for Solid State Transformer application," in *Energy Conversion Congress and Exposition (ECCE), 2010 IEEE*, 2010, pp. 1551-1558.

[14] G. Ortiz, J. Biela, and J. W. Kolar, "Optimized design of medium frequency transformers with high isolation requirements," in *IECON 2010 - 36th Annual Conference on IEEE Industrial Electronics Society*, 2010, pp. 631-638.

[15] Alibaba. (Nov. 30 2014). *"Grain-Oriented Silicon Sheets"*. Available: http://www.alibaba.com/showroom/grain-oriented-silicon-steel-sheet.html

[16] T. Soeiro, T. Friedli, and J. W. Kolar, "Three-phase high power factor mains interface concepts for Electric Vehicle battery charging systems," in *Twenty-Seventh Annual IEEE Applied Power Electronics Conference and Exposition (APEC)*, 2012, pp. 2603-2610.

[17] H. Akagi and K. Isozaki, "A Hybrid Active Filter for a Three-Phase 12-Pulse Diode Rectifier Used as the Front End of a Medium-Voltage Motor Drive," *Power Electronics, IEEE Transactions on,* vol. 27, pp. 69-77, 2012.

[18] B. N. Singh, P. Jain, and G. Joos, "Three-phase AC/DC regulated power supplies: a comparative evaluation of different topologies," in *Applied Power Electronics Conference and Exposition, 2000. APEC 2000. Fifteenth Annual IEEE*, 2000, pp. 513-518 vol.1.

[19] G. Spiazzi and F. C. Lee, "Implementation of single-phase boost power-factor-correction circuits in three-phase applications," *Industrial Electronics, IEEE Transactions on,* vol. 44, pp. 365-371, 1997.

[20] P. Drabek, Z. Peroutka, M. Pittermann, Ce, x, and M. dl, "New Configuration of Traction Converter With Medium-Frequency Transformer Using Matrix Converters," *Industrial Electronics, IEEE Transactions on,* vol. 58, pp. 5041-5048, 2011.

[21] P. Barbosa, F. Canales, and F. C. Lee, "A front-end distributed power system for high-power applications," in *Industry Applications Conference, 2000. Conference Record of the 2000 IEEE*, 2000, pp. 2546-2551 vol.4.

[22] J. W. Kolar; *et. al.*, "Three-Phase PFC Rectifier and AC-AC Converter Systems," in *Applie Power Electronics Conference (APEC)*, TX, 2011.

[23] J. W. Kolar; G. Ortiz, "Solid-State-Transformers: Key Components of Future Traction and Smart Grid Systems," in *International Power Electronics Conference - ECCE Asia (IPEC)*, Hiroshima, Japan, 2014.

[24] T. Friedli, M. Hartmann, and J. W. Kolar, "The Essence of Three-Phase PFC Rectifier Systems-Part II," *Power Electronics, IEEE Transactions on,* vol. 29, pp. 543-560, 2014.

[25] J. W. Kolar and T. Friedli, "The Essence of Three-Phase PFC Rectifier Systems-Part I," *Power Electronics, IEEE Transactions on,* vol. 28, pp. 176-198, 2013.

[26] B. Hafez, H. S. Krishnamoorthy, P. Enjeti, S. Ahmed, and I. J. Pitel, "Medium voltage power distribution architecture with medium frequency isolation transformer for data centers," in *Applied Power Electronics Conference and Exposition (APEC), 2014 Twenty-Ninth Annual IEEE*, 2014, pp. 3485-3489.

[27] H. S. Krishnamoorthy, D. Rana, P. Garg, P. N. Enjeti, and I. J. Pitel, "Wind Turbine Generator - Battery Energy Storage Utility Interface Converter Topology With Medium-Frequency Transformer Link," *Power Electronics, IEEE Transactions on,* vol. 29, pp. 4146-4155, 2014.

[28] H. S. Krishnamoorthy, P. Garg, and P. N. Enjeti, "A matrix converter-based topology for high power electric vehicle battery charging and V2G application," in *38th Annual Conference on IEEE Industrial Electronics Society*, 2012, pp. 2866-2871.

[29] C. Citro, A. Luna, J. Rocabert, R. S. Munoz-Aguilar, I. Candela, and P. Rodriguez, "Overview of power processing structures for embedding Energy Storage in PV power converters," in *IECON 2011 - 37th Annual Conference on IEEE Industrial Electronics Society*, 2011, pp. 2492-2498.

[30] M. Hartmann, J. Miniboeck, H. Ertl, and J. W. Kolar, "A Three-Phase Delta Switch Rectifier for Use in Modern Aircraft," *Industrial Electronics, IEEE Transactions on,* vol. 59, pp. 3635-3647, 2012.

[31] C. Yong-Won, K. Jung-Min, and K. Bong-Hwan, "Single Power-Conversion AC--DC Converter With High Power Factor and High Efficiency," *Power Electronics, IEEE Transactions on,* vol. 29, pp. 4797-4806, 2014.

[32] M. Narimani and G. Moschopoulos, "A New Interleaved Three-Phase Single-Stage PFC AC-DC Converter," *Industrial Electronics, IEEE Transactions on,* vol. 61, pp. 648-654, 2014.

[33] K. Ho-Sung, B. Ju-Won, R. Myung-Hyu, K. Jong-Hyun, and J. Jee-Hoon, "The High-Efficiency Isolated AC-DC Converter Using the Three-Phase Interleaved LLC Resonant Converter Employing the Y-Connected Rectifier," *Power Electronics, IEEE Transactions on,* vol. 29, pp. 4017-4028, 2014.

[34] B. Tamyurek and D. A. Torrey, "A Three-Phase Unity Power Factor Single-Stage AC-DC Converter Based on an Interleaved Flyback Topology," *Power Electronics, IEEE Transactions on,* vol. 26, pp. 308-318, 2011.

[35] B. Tamyurek, "A High-Performance SPWM Controller for Three-Phase UPS Systems Operating Under Highly Nonlinear Loads," *Power Electronics, IEEE Transactions on,* vol. 28, pp. 3689-3701, 2013.

[36] S. Norrga, S. Meier, and S. Ostlund, "A Three-Phase Soft-Switched Isolated AC/DC Converter Without Auxiliary Circuit," *Industry Applications, IEEE Transactions on,* vol. 44, pp. 836-844, 2008.

[37] J. Everts, F. Krismer, J. Van den Keybus, J. Driesen, and J. W. Kolar, "Optimal ZVS Modulation of Single-Phase Single-Stage Bidirectional DAB AC-DC Converters," *Power Electronics, IEEE Transactions on,* vol. 29, pp. 3954-3970, 2014.

[38] H. Byung-Moon, C. Nam-Sup, and L. Jun-Young, "New Bidirectional Intelligent Semiconductor Transformer for Smart Grid Application," *Power Electronics, IEEE Transactions on,* vol. 29, pp. 4058-4066, 2014.

[39] H. S. Krishnamoorthy, P. Garg, P. J. Kunwor, and P. N. Enjeti, "3-Phase AC-DC converter topologies with higher frequency transformer isolation for utility grid interface," in *Applied Power Electronics Conference and Exposition (APEC), 2014 Twenty-Ninth Annual IEEE*, 2014, pp. 1240-1247.

[40] G. Bin, J. Dominic, C. BaiFeng, and L. Jih-Sheng, "A high-efficiency single-phase bidirectional AC-DC converter with miniminized common mode voltages for battery energy storage systems," in *Energy Conversion Congress and Exposition (ECCE), 2013 IEEE*, 2013, pp. 5145-5149.

[41] M. R. Islam, G. Youguang, and Z. Jianguo, "A High-Frequency Link Multilevel Cascaded Medium-Voltage Converter for Direct Grid Integration of Renewable Energy Systems," *Power Electronics, IEEE Transactions on,* vol. 29, pp. 4167-4182, 2014.

[42] M. Swamy and T. Kume, "Present state and a futuristic vision of motor drive technology," in *Optimization of Electrical and Electronic Equipment, 2008. OPTIM 2008. 11th International Conference on*, 2008, pp. XLV-LVI.

[43] S. Inoue and H. Akagi, "A Bi-directional isolated DC/DC converter as a core circuit of the next-generation medium-voltage power conversion system," in *37th IEEE Power Electronics Specialists Conference*, 2006, pp. 1-7.

[44] D. A. Rendusara, E. Cengelci, P. N. Enjeti, V. R. Stefanovic, and J. W. Gray, "Analysis of Common Mode Voltage - "Neutral Shift" in Medium Voltage PWM Adjustable Speed Drive (MV-ASD) Systems," *IEEE Transactions on Power Electronics,* vol. 15, pp. 1124-1133, 2000.

[45] S. Jianjiang, G. Wei, Y. Hao, Z. Tiefu, and A. Q. Huang, "Research on Voltage and Power Balance Control for Cascaded Modular Solid-state Transformer," *IEEE Transactions on Power Electronics,* vol. 26, pp. 1154-1166, 2011.

[46] Z. Tiefu, Y. Liyu, W. Jun, and A. Q. Huang, "270 kVA Solid State Transformer Based on 10 kV SiC Power Devices," in *Electric Ship Technologies Symposium, 2007. ESTS '07. IEEE*, 2007, pp. 145-149.

[47] M. K. Das, C. Capell, D. E. Grider, R. Raju, M. Schutten, J. Nasadoski, S. Leslie, J. Ostop, and A. Hefner, "10 kV, 120 A SiC half H-bridge power MOSFET modules suitable for high frequency, medium voltage applications," in *Energy Conversion Congress and Exposition (ECCE), 2011 IEEE*, 2011, pp. 2689-2692.

[48] ABB. (Nov. 30, 2014). *"Powering the world economy: Is there a better way to use electricity?"*. Available: http://www04.abb.com/global/seitp/seitp202.nsf/0/ec96823a06519347c12578b500362974/$file/ABB_ElectricMotors_infographic.pdf

[49] ABB. (2011, Nov. 30, 2014). *"Chemical, Oil and Gas: Medium voltage drives for greater profitability and performance"*. Available: http://www05.abb.com/global/scot/scot216.nsf/veritydisplay/7afdc73aa9256670c12578b5004a2ae5/$file/cog%20brochure%20revc_lowres.pdf

[50] E. Hydraulic Institute, DOE. (2004, 11/26). *Variable speed pumping*. Available: http://www1.eere.energy.gov/manufacturing/tech_assistance/pdfs/variable_speed_pumping.pdf

[51] G. Gong, U. Drofenik, and J. W. Kolar, "12-pulse rectifier for more electric aircraft applications," in *Industrial Technology, 2003 IEEE International Conference on*, 2003, pp. 1096-1101 Vol.2.

[52] Siemens. (Nov. 30, 2014). *"Robicon VFDs: Perfect Harmony"*. Available: http://eastcoastmotor.com/wordpress/wp-content/uploads/2013/04/robicon-perfect-harmony-short-overview.pdf

[53] H. S. Krishnamoorthy, P. N. Enjeti, I. J. Pitel, and J. T. Hawke, "New medium-voltage Adjustable Speed Drive (ASD) topologies with medium-frequency transformer isolation," in *Power Electronics and Motion Control Conference (IPEMC), 2012 7th International*, 2012, pp. 814-819.

[54] ABB. (Nov. 30, 2014). *"Medium Voltage AC Drives: ACS 5000 Series"*. Available: http://www05.abb.com/global/scot/scot216.nsf/veritydisplay/8971bcb62448dd5dc1257b160053775b/$file/ACS%205000%20EN%20Rev%20H_lowres.pdf

[55] M. H. Rashid, *"POWER ELECTRONICS HANDBOOK"*: Academic Press, 2001.

[56] D. Wensky, "FACTS and HVDC for grid connection of large offshore wind farms."

[57] A.-K. Skytt, P. Holmberg, and L.-E. Juhlin, "HVDC Light for connection of wind farms," in *Second International Workshop on Transmission Networks for Offshore Wind Farms Royal Institute of Technology Stockholm, Sweden*, 2001.

[58] L. Harnefors, Y. Jiang-Häfner, M. Hyttinen, and T. Jonsson, "Ride-through methods for wind farms connected to the grid via a VSC-HVDC transmission," 2007.

[59] P. Jones, B. Westman, C. Plant, and M. Foster, "From generation to grid," *Renewable Energy Focus,* vol. 8, pp. 38-42, 2007.

[60] E. V. Larsen and R. W. Delmerico, "Hvdc connection of wind turbine," ed: Google Patents, 2011.

[61] T. M. CLARE JONATHAN CHARLES, ; TRAINER DAVID, ; WHITEHOUSE ROBERT, ""HYBRID 2-LEVEL AND MULTILEVEL HVDC CONVERTER"."

[62] Infineon. (Nov. 30, 2014). *"DD400S33KL2C: Technical Datasheet"*. Available: http://www.infineon.com/dgdl/Infineon-DD400S33KL2C-DS-v02_00-en_cn.pdf?fileId=db3a30433e20bc87013e20c67d6c0001

[63] Z. Jindong, M. M. Jovanovic, and F. C. Lee, "Comparison between CCM single-stage and two-stage boost PFC converters," in *Applied Power Electronics Conference and Exposition, 1999. APEC '99. Fourteenth Annual*, 1999, pp. 335-341 vol.1.

[64] ABB. (Nov 30 2014). *"ABB Boderline"*. Available: http://www05.abb.com/global/scot/scot271.nsf/veritydisplay/febcd9def08a98dbc12575e4004a0f2f/$file/35-41%202m967_eng72dpi.pdf

[65] H. Polinder, D. Bang, R. P. J. O. M. van Rooij, A. S. McDonald, and M. A. Mueller, "10 MW Wind Turbine Direct-Drive Generator Design with Pitch or Active Speed Stall Control," in *Electric Machines & Drives Conference, 2007. IEMDC '07. IEEE International*, 2007, pp. 1390-1395.

[66] J. S. Thongam; and M. Ouhrouche;. (Nov. 30 2014). *"MPPT Control Methods in Wind Energy Conversion Systems"*. Available: http://www.intechopen.com/books/fundamental-and-advanced-topics-in-wind-power/mppt-control-methods-in-wind-energy-conversion-systems

[67] L. Maharjan, S. Inoue, H. Akagi, and J. Asakura, "A transformerless battery energy storage system based on a multilevel cascade PWM converter," in *2008 IEEE Power Electronics Specialists Conference*, 2008, pp. 4798-4804.

[68] P. F. Ribeiro, B. K. Johnson, M. L. Crow, A. Arsoy, and Y. Liu, "Energy storage systems for advanced power applications," *Proceedings of the IEEE,* vol. 89, pp. 1744-1756, 2001.

[69] S. Sharma and B. Singh, "Performance of Voltage and Frequency Controller in Isolated Wind Power Generation for a Three-Phase Four-Wire System," *Power Electronics, IEEE Transactions on,* vol. 26, pp. 3443-3452, 2011.

[70] X. Zhuang, L. Rui, Z. Hui, X. Dianguo, and C. H. Zhang, "Control of Parallel Multiple Converters for Direct-Drive Permanent-Magnet Wind Power Generation Systems," *Power Electronics, IEEE Transactions on,* vol. 27, pp. 1259-1270, 2012.

[71] ABB. (Nov. 30 2014). *"DES Distributed Energy Storage modules Up to 2MW"*. Available: http://www05.abb.com/global/scot/scot235.nsf/veritydisplay/209ba3fbd42472a6c1257b130057436f/$file/des_brochure.pdf

[72] N. W. Miller, R. S. Zrebiec, G. Hunt, and R. W. Deimerico, "Design and commissioning of a 5 MVA, 2.5 MWh battery energy storage system," in *Transmission and Distribution Conference, 1996. Proceedings., 1996 IEEE*, 1996, pp. 339-345.

[73] S. Thomas, M. Stieneker, and R. W. De Doncker, "Development of a modular high-power converter system for battery energy storage systems," in *Power Electronics and Applications (EPE 2011), Proceedings of the 2011-14th European Conference on*, 2011, pp. 1-10.

[74] L. H. Walker, "10 MW GTO converter for battery peaking service," in *Industry Applications Society Annual Meeting, 1988., Conference Record of the 1988 IEEE*, 1988, pp. 850-858 vol.1.

[75] J. P. Barranger, *Hysteresis and eddy-current losses of a transformer lamination viewed as an application of the Poynting theorem*: National Aeronautics and Space Administration, 1965.

[76] D. E. Consultancy. (Nov. 30 2014). *"Best Practice Manual for Electric Transformers"*. Available: http://www.energymanagertraining.com/bee_draft_codes/best_practices_manual-TRANSFORMERS.pdf

[77] Q. Hengsi and J. W. Kimball, "Solid-State Transformer Architecture Using AC–AC Dual-Active-Bridge Converter," *Industrial Electronics, IEEE Transactions on,* vol. 60, pp. 3720-3730, 2013.

[78] T. Zhao, G. Wang, S. Bhattacharya, and A. Q. Huang, "Voltage and Power Balance Control for a Cascaded H-Bridge Converter-Based Solid-State Transformer," *Power Electronics, IEEE Transactions on,* vol. 28, pp. 1523-1532, 2013.

[79] S. Deshang, X. Guo, and L. Xiaozhong, "Control Strategy for Input-Series-Output-Series High-Frequency AC-Link Inverters," *Power Electronics, IEEE Transactions on,* vol. 28, pp. 5283-5292, 2013.

[80] H. S. Krishnamoorthy, P. Garg, and P. N. Enjeti, "A new medium-voltage energy storage converter topology with medium-frequency transformer isolation," in *Energy Conversion Congress and Exposition (ECCE), 2012 IEEE*, 2012, pp. 3471-3478.

[81] P. R. Tenca, A. A.; Lipo, T. A. (2007, 11/26). *LVRT Capability for Wind Turbines based on Current Source Inverter Topologies*. Available: http://lipo.ece.wisc.edu/2007pubs/2007_34.pdf

[82] K. Ki-Hong, J. Yoon-Cheul, L. Dong-Choon, and K. Heung-Geun, "LVRT Scheme of PMSG Wind Power Systems Based on Feedback Linearization," *Power Electronics, IEEE Transactions on,* vol. 27, pp. 2376-2384, 2012.

[83] T. Senjyu, N. Nakasone, A. Yona, A. Y. Saber, T. Funabashi, and H. Sekine, "Operation strategies for stability of gearless wind power generation systems," in *Power and Energy Society General Meeting - Conversion and Delivery of Electrical Energy in the 21st Century, 2008 IEEE*, 2008, pp. 1-7.

[84] A. V. d. Bossche; and V. C. Valchev;. (Nov 30 2014). *"Inductors and Transformersfor Power Electronics"*. Available: http://192.211.49.220/-%20Electronics/Books/Inductors%20And%20Transformers%20For%20Power%20Electronics.pdf

[85] W. books. (Nov 30 2014). *"Transformer Design"*. Available: http://en.wikibooks.org/wiki/Electronics/Transformer_Design

[86] C. W. T. McLyman, *Transformer and Inductor Design Handbook, Third Edition*: Taylor & Francis, 2004.

[87] J. Biela and J. W. Kolar, "Cooling Concepts for High Power Density Magnetic Devices," in *Power Conversion Conference - Nagoya, 2007. PCC '07*, 2007, pp. 1-8.

[88] Metglas. (Nov 30 2014). *"Metglas® 2605SA1 & 2605HB1M Magnetic Alloy"*. Available: http://www.metglas.com/products/magnetic_materials/2605sa1.asp

[89] Philips. (Nov 30 2014). *"Magnetic Products-Data Sheet"*. Available: http://www.thierry-lequeu.fr/data/3C85.pdf

[90] C. W. T. McLyman. (Nov 30 2014). *"Window Utilization Factor"*. Available: http://www.kgmagnetics.org/APNOTES-06/An-102.pdf

[91] E. Colarado. (Nov. 30 2014). *"Inductor Design"*. Available: http://ecee.colorado.edu/~ecen5797/course_material/Ch14slides.pdf

[92] Infineon. (Nov. 30, 2014). *"FZ400R33KL2C: Technical Datasheet"*. Available: http://www.infineon.com/dgdl/Infineon-FZ400R33KL2C_B5-DS-v02_00-en_cn.pdf?fileId=db3a30433e16edf9013e184ae5870336

[93] J. Biela, U. Badstuebner, and J. W. Kolar, "Impact of Power Density Maximization on Efficiency of DC–DC Converter Systems," *Power Electronics, IEEE Transactions on,* vol. 24, pp. 288-300, 2009.